UNIVERSITY OF CALIFORNIA

Santa Barbara

Tuning Electrostatic Interactions in Confined Soft Matter

A dissertation submitted in partial satisfaction of the

requirements for the degree Doctor of Philosophy

in

Materials

by

Matthew Allen Gebbie

Committee in charge:

Professor Jacob N. Israelachvili, Chair

Professor J. Herbert Waite

Professor Cyrus R. Safinya

Professor Omar A. Saleh

March 2016

The dissertation of Matthew Allen Gebbie is approved.

_____

J. Herbert Waite

_____

Cyrus R. Safinya

_____

Omar A. Saleh

_____

Jacob N. Israelachvili, Committee Chair

December 2015

Tuning Electrostatic Interactions in Confined Soft Matter

by

Matthew Allen Gebbie

Acknowledgements

I tremendously enjoyed my extended ‘vacation’ in Santa Barbara. Looking back on the last five years, one thing is clear: I was incredibly privileged to spend my graduate studies surrounded by fun, supportive, and brilliant friends, colleagues, and mentors.

First and foremost, I thank my amazing wife Allison for her tireless support and encouragement during this long and demanding process. My time in Santa Barbara would have been an entirely inferior experience without Allie taking a leap faith, walking away from employment as a Chemical Engineer to move across the country. For the record, Allie’s advice and feedback helped me get multiple scientific papers accepted, be selected to attend a once-in-a-lifetime international conference, and succeed in winning two proposals.

I am also extremely grateful for my family, and I thank my parents, David and Deborah, as well as my grandparents, John, Dorothy, Warren, and Mary Jo for their constant faith and support. My education would not have been possible without such an extraordinary family.

I would not have succeeded in earning a Ph.D. without Wes Henderson’s and Michael Dickey’s support and encouragement during my undergraduate years. Wes and Michael are fantastic mentors who both had a profound positive impact on my life.

On the scientific front, I truly appreciate the professors, students, and staff at UCSB who created the stimulating environment that I needed to develop into an independent researcher. I am indebted to Jacob Israelachvili, who taught me how to select important questions, critically analyze complex problems, and seek rigorous explanations for surprising observations, all while encouraging me to lead my research in directions that I found most engaging. I likewise value the perspectives and enthusiasm provided by Herb Waite, Omar Saleh, and Cyrus Safinya. From discussions on protein biochemistry, to seminars on single

molecule mechanics, I'm confident that they helped me develop the broader context that is necessary to stay excited about tackling new scientific challenges.

A significant portion of my graduate experience was defined by collaborations, discussions, and social outings with members of Jacob's lab. Additionally, Rich Appelbaum, Shirley Han, Galen Stocking Luciano Kay, and the other members of the UCSB CNS played a large role in shaping my academic perspective and helped me learn how to communicate across disciplines. I am grateful to have worked with such a diverse and interesting collection of scientists and social scientists. I am especially fortunate to have collaborated with Markus Valtiner at the beginning of my Ph.D.; Markus helped me turn my initial ideas into reality, and I will fondly remember our numerous late night experiments – complete with scientific, philosophical, and sociopolitical discussions. I also greatly enjoyed working with Xavier Banquy, Alex Schrader, Steve Donaldson, Howie Dobbs, Wei Wei, and Tom Cristiani, who all had tangible impacts on the development of my dissertation research. I am likewise very appreciative of Nancy Emerson, who helped me stay organized, enabling me to focus more of my time on science.

Last but not least, I thank Evan F., Erin K., Peter M., Bo S., Greg S., Leah K., Luke G., Anne G., Nick C., Alex S., the other Alex S., Mike G., Chris F., Nate K., Davey J., Grace A., Kaylan W., Luke R., and Alan L. for greatly enhancing the many hours of surfing, hiking, climbing, camping, and biking that allowed me to decompress from the stress and uncertainty that can be associated with pursuing a Ph.D.

Finally, I would like to dedicate this dissertation to Allison, who always remains patient, even when I forget the most important slides in my presentations. I am excited to continue our journey together, and I look forward to whatever the future holds.

Curriculum Vitae of Matthew Allen Gebbie

Education

Ph.D. in Materials Science, December 2015
University of California, Santa Barbara, CA
Advisor: Professor Jacob N. Israelachvili
Thesis Title: Tuning electrostatic interactions in confined soft matter

B.S. in Chemical Engineering, minor in Business Administration, 2010
North Carolina State University; Raleigh, NC
Graduated Cum Laude

Research Experience

- **Ph.D. candidate,** Prof. Jacob N. Isrealachvili**,** UCSB, Materials Department, October 2010 – December 2015.
    - Developed force measuring techniques with *in situ* electrochemical control.
    - Discovered mechanism of long range electrostatic screening in ionic liquids.
    - Developed molecular design principles for mussel-mimetic underwater adhesives.
    - Self-assembly interactions in biological systems (P&G collaboration).

- **Researcher**, Aromatic dissolution in ionic liquids, Prof. Wesley Henderson, North Carolina State University, Department of Chemical and Biomolecular Engineering, May 2009 – August 2010.
    - Synthesized novel ionic liquids.
    - Combined NMR, kinetic studies to quantify aromatic solubility in ionic liquids.
    - Proposed molecular design principles for aromatic-aliphatic separations in petroleum processing.

Publications

1. Valtiner, M., Donaldson, S. H., Gebbie, M. A., Israelachvili, J. N. Hydrophobic forces, electrostatic steering, and acid-base bridging between atomically smooth self-assembled monolayers and end-functionalized PEGolated lipid bilayers. *J Am. Chem. Soc.* **134** (3), 1746-1753 (2012).

2. Donaldson, S. H., Valtiner, M., Gebbie, M. A., Harada, J., Isrealachvili, J. N. Interactions and visualization of bio-mimetic membrane detachment at smooth and nano-rough gold electrode surfaces. *Soft Matter* **9** (21), 5231-5238 (2013).

3. Gebbie M. A., Valtiner, M., Banquy, X., Fox, E. T., Henderson, W. A., Isrealachvili, J. N. Ionic liquids behave as dilute electrolyte solutions. *Proc. Natl Acad. Sci. USA* **110** (24), 9674-9679 (2013).

4. Gebbie M. A., Valtiner, M., Banquy, X., Henderson, W., Isrealachvili, J. Reply to Perkin et al.: Experimental observations demonstrate that ionic liquids form both bound (Stern) and diffuse electric double layers. *Proc. Natl Acad. Sci. USA* **110** (44), E4122 (2013).

5. Donaldson, S. H., Das, S., Gebbie, M. A., Rapp, M. V., Jones, L. C., Roiter, Y., Koenig, P. H., Gizaw, Y., Israelachvili J. N. Asymmetric electrostatic and hydrophobic-hydrophilic interaction forces between mica surfaces and silicone polymer thin films. *ACS Nano* **7** (11), 10094-10104 (2013).

6. Israelachvili, J. N., Kristiansen K., Gebbie M. A., Lee D. W., Donaldson S. H., Das S., Rapp M. V., Banquy X., Valtiner M., Yu J. The intersection of interfacial forces and electrochemical reactions. *J. Phys. Chem. B* **117** (51), 16369-16387 (2013).

7. Donaldson, S. H., Utzig T., Gebbie M. A., Raman S., Shrestha B. R., Israelachvili J. N., Valtiner M. Electrochemical control of specific adhesion between amine-functionalized polymers and noble metal electrode interfaces. *Matrl. Corr.* **65** (4), 362-369 (2014).

8. Rapp, M. V., Donaldson S. H., Gebbie M. A., Das S., Kaufman Y., Gizaw Y., Koenig P. H., Roiter Y., Israelachvili J. N. Hydrophobic, electrostatic, and dynamic polymer forces at polysurfactant-modified silicone surfaces. *Small* **11** (17), 2058-2068 (2014).

9. Wei Wei, Yu J., Gebbie M. A., Tan Y., Martinez Rodriguez N. R., Israelachvili J. N., Waite J. H. The bridging adhesion of mussel-inspired peptides: role of charge, chain length, and surface type. *Langmuir* **31** (3), 1105-1112 (2015).

10. Donaldson, S. H., Røyne A., Kristiansen K., Rapp M. V., Das S., Gebbie M. A., Lee D. W., Stock P., Valtiner M., Israelachvili J. N. Developing a general interaction potential for hydrophobic and hydrophilic interactions. *Langmuir* **31** (7), 2051-2250 (2015).

11. Gebbie M. A., Dobbs H. A., Valtiner M., Israelachvili J. N. Long range electrostatic screening in ionic liquids. *Proc. Natl Acad. Sci. USA* **112** (24), 7432-7437 (2015)**.**

12. Rapp M. V., Donaldson S. H., Gebbie M. A., Gizaw Y., Koenig P., Roiter Y., Israelachvili J. N. The effects of surfactants and polyelectrolytes on the interaction between a

negatively charged surface and a hydrophobic polymer surface. *Langmuir* **31** (29), 8013-8021 (2015).

13. Banquy, X., Lee DW, Kristainsen K, Gebbie MA, Israelachvili JN. Interaction forces between supported lipid bilayers in presence of PEGylated polymers. *Biomacromolecules* **17** (1), 88-97 (2016).

14. Gebbie, M. A., Wei Wei, Schrader, A. M., Cristiani, T., Griffin, A., Waite, J. H., Isrealachvili, J. N. Tuning underwater adhesion with cation-pi interactions.

Presentations

- "Tuning underwater adhesion with cation-π interactions." Invited Oral, *Materials Research Outreach Program 2016,* Santa Barbara, CA, 2 February 2016.
- "Ionic liquids and water: the surprising connection." Poster, *Gordon Research Conference: Chemistry and Physics of Liquids,* Holderness, NH, 5-6 August 2015.
- "Ionic liquids and water: the surprising connection." Oral presentation, *Gordon Research Seminar: Chemistry and Physics of Liquids,* Holderness, NH, 1 August 2015.
- "Ionic liquids and water: the surprising connection." Oral presentation, *American Chemical Society, 2015 National Meeting,* Denver, CO, 26 March 2015.
- "Engineering underwater adhesives: leveraging cation-pi interactions to govern peptide cohesion." Oral presentation, *American Chemical Society, 2015 National Meeting,* Denver, CO, 24 March 2015.
- "Ionic liquids and dilute electrolytes: the surprising connection." Poster presentation, *Surface Forces Apparatus Conference 2014,* Cancun, Mexico, 26 August 2014.
- "Ionic liquids and dilute electrolytes: the surprising connection." Oral presentation, *Liquids 2014:9th Liquid Matter Conf., Univ. Lisboa,* Lisbon, Portugal 23 July 2014.
- "Bio-inspired adhesion: local chemical environments impact adhesive stability." Oral presentation, *American Physical Society, March 2014,* Denver, CO, 4 March 2014.
- "Ionic liquids behave as dilute electrolytes." Oral presentation, *American Institute of Chemical Engineering, 2013 Annual Meeting,* San Francisco, CA, 5 November 2013.
- "Dopa-mediated adhesion: local chemical environments and redox stability." Poster presentation, *UCSB/CWNU/KAIST Workshop on Biologically-Inspired Soft Matter, University of California,* Santa Barbara, CA, 24 September 2013.
- "Ionic liquids behave as dilute electrolyte solutions." Poster presentation, *Gordon Research Conference: Chem. and Phys. of Liquids,* Holderness, NH, 5-6 August 2013.
- "Ionic liquids behave as dilute electrolyte solutions." Oral presentation, *Materials Research Society, Spring 2013 Meeting,* San Francisco, CA, 3 April 2013.

- "Impact of ionic liquid molecular structure on intersurface forces in nanoconfined films." Oral presentation, *American Institute of Chemical Engineers, 2011 Annual Meeting*, Minneapolis, MN, 20 October 2011.
- "Dissolution of aromatics in ionic liquids: exploring the influence of ion structure on solubility." Oral presentation, *American Chemical Society, Spring 2010 National Conference*, San Francisco, CA, 23 March 2010.

Selected Awards and Distinctions

- 2016–2018 Geballe Laboratory for Advanced Materials Postdoctoral Fellowship, Stanford University.
- Science and Engineering Fellow, National Science Foundation Center for Nanotechnology in Society, UC Santa Barbara, 2011–2015.
- Selected by the National Science Foundation to attend the 2015 Lindau Nobel Laureate Interdisciplinary Meeting in Lindau, Germany, July 2015.
- GradSlam Finalist, UC Santa Barbara, April 2015.
- STEMposium Invited Speaker, UC Santa Barbara, May 2015.
- "Outstanding Poster" Award, Surface Forces Apparatus Conference 2014, Cancun, Mexico, August 2014.
- Doctoral Student Travel Grant, Academic Senate, UC Santa Barbara, travel to Universidade de Lisboa, Lisbon, Portugal, July 2014.
- Chemical Sciences Student Seminar Invited Speaker, UC Santa Barbara, October 2013.
- Materials Research Laboratory-Dow Materials Institute Travel Fellowship, UC Santa Barbara, 2013.
- Honorable Mention, National Science Foundation Graduate Research Fellowship, 2011.

Abstract

Tuning Electrostatic Interactions in Confined Soft Matter

by

Matthew Allen Gebbie

Electrostatic interactions determine the key properties of several materials that promise to enable revolutionary nanotechnologies. For example, the power delivered by ionic liquid-based supercapacitors, and the curing time of bio-inspired surgical adhesives, both hinge on the collective behavior of large ensembles of ions in confined interfaces. However, a comprehensive framework for understanding and influencing electrostatic interactions in highly concentrated electrolytes remains elusive. We address this knowledge gap by using nanoscale force-distance measurements to investigate and tune electrostatic interactions in interfaces containing high ionic densities, with an aim of providing quantitative molecular foundations to guide nanomaterials design.

In this dissertation, we first review our extension of the Surface Forces Apparatus technique (SFA) to enable force-distance measurements with *in situ* electrochemical control (the EC SFA). Next, we discuss how EC SFA experiments were combined with temperature-controlled SFA measurements to demonstrate that the electrostatic screening properties of ionic liquids can be rationalized using mean-field theories by focusing on local excess charge densities, as opposed to explicitly accounting for the distribution of every ion. Finally, we

illustrate the pivotal role of electrostatic interactions in governing the adhesive performance of mussel-mimetic peptides and conclude with an analysis of how natural proteins provide molecular themes that may guide the design of biomedical adhesives.

Table of Contents

List of Figures

List of Tables

1 Introduction and Motivation

The development of techniques for manipulating matter at the nanometer-scale has opened the door to revolutionary scientific and technological possibilities. On the fundamental front, the invention of methods to controllably synthesize optically-active nanoparticles promises to enable the real-time, *in vitro* imaging of living cells at the single molecule level [1, 2], yielding meaningful insights into complex biological processes, like stem cell differentiation and cancer metastasis. On the technological front, the development of nanotechnologies promise to provide entirely new solutions to many of society's most pressing problems, ranging from carbon nanomaterials that enable dramatic increases in our ability to generate and store energy [3], to self-assembling molecules that enable advanced biomaterials that actively interface with bone, skin, and internal organs [4].

During the previous two decades, the rapid progression of nanoscale science and engineering has been largely driven by the National Nanotechnology Initiative (NNI), which was introduced by the United States government in the year 2000. The US NNI has expended about $22 billion to date, with $1.5 billion in additional funds for 2016 [5] and firmly sets the nanoscale engineering of materials as a United States national scientific priority. Further, the NNI explicitly highlights nanotechnology as a driver of the next major industrial revolution, with predicted societal benefits that could significantly exceed those offered by the microelectronics revolution by the year 2025.

While it is unclear whether nanoscale science and engineering is on pace to surpass the electronics industry in terms of societal impact – indeed many nanotechnologies are actually

driving advances in the electronics industry – nanoscale science and engineering already influences many aspects of modern life. High performance nanocomposite materials are used to create strong, lightweight bicycles and automobiles [6], and nanotechnology-enabled consumer products, such as stain-resistant clothing [7] and invisible sunscreens [8], can be found in almost every American household. Over the longer term, advances to existing applications are predicted to be only the tip of the iceberg. However, many of these lofty visions appear to have outpaced the scientific community's ability to predict and tune interactions between the extremely large numbers of molecules that make up the interfaces in most nanotechnologies, which are also much too complex for a trial-and-error approach to be a sustainable long-term solution. Hence, further fundamental studies in the area of nano- to meso-scale interactions – the realm of colloid and interface science – will be indispensable for the success of nanoscale science and engineering.

Colloid and interface science is a cross-disciplinary field that leverages ideas and approaches from several traditional areas, including chemistry, physics, and biology, to study the behavior of matter over length scales spanning from nanometers to many micrometers [2]. In this size regime, colloidal systems are strongly influenced by thermal fluctuations. Further, atomic, molecular, and surface interactions are either competitive with or vastly exceed the influence of gravitational forces. Thus, intermolecular interactions and surface forces play a dominant role in determining the properties of colloidal materials, particularly for colloidal systems that are composed of at least one fluid phase.

The primary aim of this dissertation is to develop phenomenological frameworks for rationalizing, and ultimately tuning, the behavior of large ensembles of ions in confined interfaces. This would greatly aid the development of materials and architectures for energy

storage devices and could also be leveraged to gain deeper insight into the assembly processes of charged biological molecules, like mussel adhesive proteins and DNA-protein complexes. Nevertheless, the high interaction strength and very long range influence of electrostatic interactions makes the behavior of highly concentrated populations of ions extremely difficult explicitly model using molecular simulations [9]. Furthermore, there is a dearth of mean-field theories that are applicable to systems containing high ionic densities [10]. Hence, we address this knowledge gap through the use of experimental studies of confined soft matter systems composed of high concentrations of ions and/or charged functional groups to develop quantitative frameworks that can be applied to rationalize and tune the properties of high ion density nanomaterials.

1.1 Electrostatic screening in ionic liquids

Room temperature ionic liquids are single component liquids that are composed solely of ions. To date, thousands of ionic liquids have been identified with diverse physical properties that can be tuned via careful design of cation-anion pairs [11]. Notably, many common cations that are prevalent in ionic liquids are derived from imidazolium rings, primary amines, and other molecular structures that are prominently featured in amino acid functional groups. Thus, there is ultimately a molecular connection between the short range ion structuring interactions that we measure across ionic liquids and the electrostatic cohesive interactions that we measure across bio-inspired adhesive peptides.

The properties of ionic liquids are strongly influenced by the same strong electrostatic interactions that underlie the properties of solid salts, like sodium chloride. However ionic liquids are composed of large ions with asymmetric charge distributions (Fig. 1.1), which frustrates the formation of solid crystals. Notably, the high thermal and electrochemical

stabilities, negligible volatilities, and variable intrinsic ionic conductivities of many ionic liquids make them excellent candidate materials for several emerging nanotechnologies, including: electric double-layer capacitors, batteries, and self-assembly media [12–14].

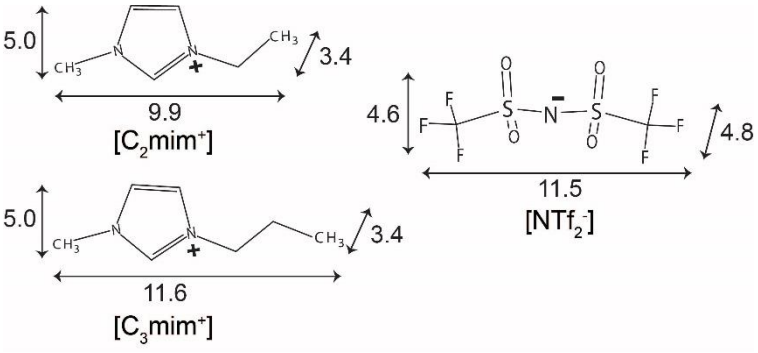

Figure 1.1 Chemical structures and approximate dimensions of the RTIL ions studied in Chapter 4. Molecular dimensions were calculated from the van der Waals radii of the constituent atoms.

The successful integration of ionic liquids into such applications will require a fundamental understanding of the physical characteristics of the interfaces that are formed between ionic liquids and charged surfaces. However, the properties of ionic liquid electric double-layers remains an active area of research and discussion. When we initiated this research in 2010, the generally accepted picture of electrostatic screening in confined ionic liquids was that ionic liquid double-layers consist of ordered layers of cations and anions extending away from surfaces out to 3–5 ionic diameters [15].

Chapter 3 describes our experiments using the Surface Forces Apparatus technique with *in situ* electrochemical control (the EC SFA), where we discovered that the electric double-layers formed by ionic liquids can actually extend out to distances exceeding 35 ionic diameters per surface. Further, the surface forces that are characteristic of these electric double-layers are monotonic for surface separations that exceed several ionic diameters, an observation that contradicts the exclusive formation of well-ordered layers. We used this

observation to propose that the electrostatic screening properties of ionic liquids can be rationalized by considering ionic liquid ions to exist in two distinct states: thermally-dissociated “free” ions, and effectively charge neutral “coordinated” ions. Our key advance is to demonstrate that the electrostatic screening properties of ionic liquids can be modeled using standard mean-field theories of electrostatic screening, like the Poisson-Boltzmann equation discussed in Section 2.2, as long as the equations are reframed in terms of excess charge densities, instead of total charge densities.

Chapter 4 outlines our efforts to test a key prediction of the framework we develop in Chapter 3, namely that increasing temperatures will increase the effective ionic strength of ionic liquids by driving the thermal dissociation of effectively “free” ions. In this work, we performed surface forces measurements across two prototypical ionic liquids at various temperatures, and found that the electric double-layers formed by ionic liquids decrease in range as the temperature increases. Further, this decrease was consistent with an ionic liquid specific charge carrier activation energy that can be rationalized by considering ion pair interaction energies to be decreased by the bulk dielectric permittivity of ionic liquids.

A further aim of Chapter 4 is to generalize the picture proposed in Chapter 3 by reframing the discussion of electrostatic screening in terms of thermally-activated charged quasiparticles, either free ions or correlated charge domains, reminiscent of the free electron/hole approximation used in semiconductor physics. This refinement opens the door to applying these ideas to high concentration multicomponent electrolyte solutions, like battery electrolytes, ionic liquid mixtures, and aqueous electrolyte solutions, which may provide a fruitful avenue for future research.

1.2 Adhesive performance of bio-inspired peptides

Marine mussels, sandcastle worms, barnacles and numerous other marine organisms leverage highly adhesive proteins to strongly anchor to solid surfaces in the highly dynamic intertidal region of marine environments. Many of these adhesive proteins are rich in the amino acid functional group 3,4-dihydroxyphenyl-L-alanine (Dopa) [16, 17] (Fig. 1.2). Dopa exhibits broad chemical functionality that is beneficial for underwater adhesion, such as undergoing autoxidation-induced covalent crosslinking, and Dopa is also hypothesized to form strong bidentate hydrogen bonding interactions with surfaces. Nevertheless, certain marine organisms, like barnacles, achieve strong underwater adhesion using proteins that are sparing in Dopa [18], and many studies demonstrate that Dopa alone is no guarantee that a molecule will function as a strong underwater adhesive [17].

In Chapter 5, we explore the role that the charged amino acids flanking Dopa in mussel proteins play in promoting adhesive interactions in mussel-inspired peptides. In particular, we demonstrate that electrostatic charge-charge interactions play a crucial role in enabling underwater bio-adhesion, even in high salt environments reminiscent of seawater and biological fluids. In these experiments, we designed three short mussel foot protein-inspired peptides that each contain an equivalent mol % of Dopa, while surrounding the Dopa residues with amino acids that dramatically differ: one of the peptides is acidic and exhibits a negative charge at seawater pH, one peptide is neutral at seawater pH, and one of the peptides is strongly basic and exhibits a positive charge at seawater pH. Surprisingly, we found that the positive peptide exhibits distinct behavior by mediating much stronger adhesive and cohesive interactions between mica surfaces than the negative or neutral peptides, and this observation

cannot be explained solely by considering surface-peptide charge-charge interactions and bidentate hydrogen bonding.

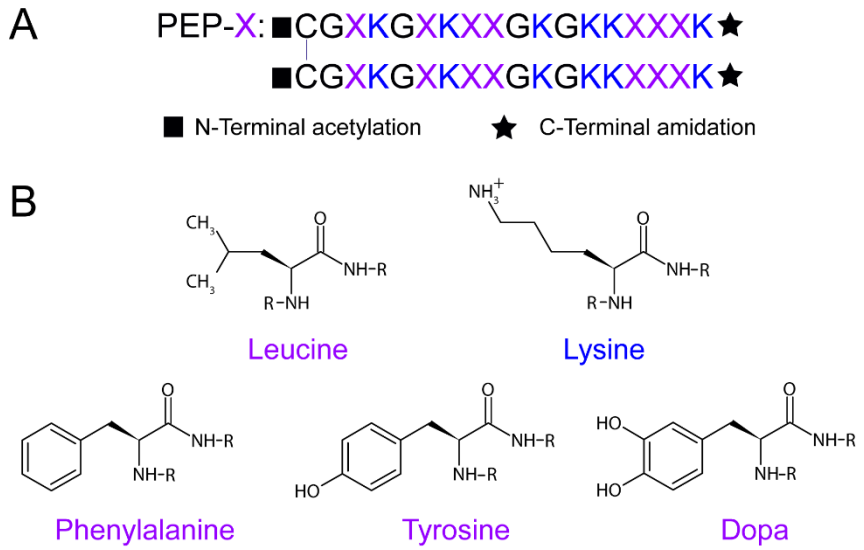

Figure 1.2. Sequences and molecular structures of the peptides studied in Chapter 6. Each of the four peptides included one of the amino acids illustrated in panel **(B)** incorporated in the sequence locations marked by a purple "X" in panel **(A)**. The Lys residues are conserved in each peptide sequence and are marked in blue to emphasize the positive charge of Lys at a pH of 2.5.

Chapter 6 focuses on developing deeper molecular-scale insight into the adhesive behavior of these positively charged peptides that are rich in Dopa or other aromatic amino acids, shown in Figure 1.2. Overall, we resolve several questions raised in Chapter 5 by demonstrating that cation-π interactions, in addition to specific Dopa hydrogen bonding or charge-charge interactions, appear to be a major contributor to the strong cohesive interactions between lysine- and aromatic-rich peptides. Ultimately, we demonstrate that these engineered short peptides self-assemble into nanoscale films that mediate wet adhesion that is competitive with full mussel foot proteins. Thus, we conclude that the presence of high densities of both aromatic and cationic residues are important for wet bio-adhesion.

Notably, we find that peptides with the amino acid phenylalanine, which is sparing in mussel proteins, exhibits the strongest adhesive performance. We interpret this observation to indicate that interfacial confinement fundamentally alters the energetics of cation-π interactions via many-body electrostatic interactions. If confirmed, then this proposal should prove relevant for diverse materials design activities, ranging from the development of surgical adhesives, to the design of tissue engineering scaffolds. 1.3 Organization of dissertation

Chapter 2 begins with a philosophical overview of using surface force measurements to guide the design of nanomaterials, followed by an in-depth discussion of electrostatic interactions and broad overviews of van der Waals interactions and of short range, specific intermolecular interactions. Chapter 2 concludes by providing detailed descriptions of the Surface Forces apparatus technique and the electrochemical modifications that enabled the research described in the remainder of this dissertation.

Chapters 3 and 4 describe our research on the molecular-scale mechanism of electrostatic screening in ionic liquids and other highly concentrated electrolyte solutions, and Chapter 4 concludes with an overview of future avenues of research on ionic liquids and high ionic strength electrolytes that may prove promising. Chapters 5 and 6 discusses our efforts to develop molecular design principles for bio-inspired underwater adhesives, with a focus on our research demonstrating that short range electrostatic interactions play a key role in enabling the adhesive performance of bio-inspired proteins and peptides, even in highly concentrated electrolyte solutions. Chapter 6 then concludes with a broad overview of the open questions remaining in the area of marine bio-adhesion.

1.4 References

1. Schirhagl R., Chang K., Loretz M., Degen C. L. Nitrogen-vacancy centers in diamond: nanoscale sensors for physics and biology. *Annu. Rev. Phys. Chem.* **65,** 83–105 (2014).
2. Michalet X. et al. Quantum dots for live cells, in vivo imaging, and diagnostics. *Science* **538,** 538–545 (2012).
3. Simon P., Gogotsi Y. Materials for electrochemical capacitors. *Nat. Mater.* **7,** 845–854 (2008).
4. Lee K. Y., Mooney D. J. Hydrogels for tissue engineering. *Chem. Rev.* **101**(7)**,** 1869–1879 (2001).
5. http://www.nano.gov
6. Breuer O., Sundararaj U. Big returns from small fibers: a review of polymer/carbon nanotube composites. *Polym. Compos.* **25,** 630–645 (2004).
7. Ma M., Hill R. M. Superhydrophobic surfaces. *Curr. Opin. Colloid Interface Sci.* **11,** 193–202 (2006).
8. Buzea C., Pacheco I. I., Robbie K. Nanomaterials and nanoparticles: sources and toxicity. *Biointerphases* **2,** MR17–MR71 (2007).
9. Bazant M. Z., Kilic M. S., Storey B. D., Ajdari A. Towards an understanding of induced-charge electrokinetics at large applied voltages in concentrated solutions. *Adv. Colloid Interface Sci.* **152,** 48–88 (2009).
10. Giera B., Henson N., Kober E. M., Squires T. M., Shell M. S. Model-free test of local-density mean-field behavior in electric double layers. *Phys. Rev. E* **88,** 011301 (2013).
11. Welton T. Room-temperature ionic liquids. Solvents for synthesis and catalysis. *Chem. Rev*. **99,** 2071–2083 (1999).

12. Antonietti M., Kuang D., Smarsly B., Zhou Y. Ionic liquids for the convenient synthesis of functional nanoparticles and other inorganic nanostructures. *Angew. Chemie - Int. Ed.* **43,** 4988–4992 (2004).
13. Galinski M., Lewandowski, Stepniak I. Ionic liquids as electrolytes. *Electrochim. Acta* **51,** 5567–5580 (2006).
14. Armand M., Endres F., MacFarlane D. R., Ohno H., Scrosati B. Ionic liquid materials for the electrochemical challenges of the future. *Nat. Mater.* **8,** 621–629 (2009).
15. Kornyshev A. A. Double-layer in ionic liquids: paradigm change? *J. Phys. Chem. B* **111,** 5545–5557 (2007).
16. Stewart R. J., Weaver J. C., Morse D. E., Waite J. H. The tube cement of Phragmatopoma californica: a solid foam. *J. Exp. Biol.* **207,** 4727–4734 (2004).
17. Lee B. P., Messersmith P. B., Israelachvili J. N., Waite J. H. Mussel-inspired adhesives and coatings. *Annu. Rev. Mater. Res.* **41,** 99–132 (2011).
18. Kamino K., Nakano M., Kanai S. Significance of the conformation of building blocks in curing of barnacle underwater adhesive. *FEBS J.* **279,** 1750–1760 (2012).

2 Force measurements to guide materials design

As engineered structures are decreased to the nanoscale, the ratio of exposed surface area to bulk material dramatically increases. As a result, the properties of many nanomaterials are predominantly, if not entirely, determined by exposed surfaces and colloidal interactions between adjacent surfaces. For example, carbon atoms at the surface of diamond nanoparticles cannot from tetrahedral coordination bonds with 4 other carbon atoms, as in bulk diamond. Surface carbon atoms instead expose unfilled molecular orbitals that either react with other atoms like oxygen or hydrogen, or form additional π-bonding covalent interactions with adjacent surface carbons. Each of these outcomes exhibits a distinct influence on nanoparticle surface chemistry, surface charge, and electronic structure [1].

Further, gravity typically has a negligible impact on many nanomaterials and nanoscale structures. Thus, the intuition and rules that guide the design of macroscopic engineering activities, such as the construction of bridges and skyscrapers, must be replaced by design rules that emphasize intermolecular and surface interactions. In modern times, researchers can select from among numerous nanoscale characterization methods to develop the intuition necessary to design nanomaterials, including x-ray and neutron scattering, optical and magnetic spectroscopy, and electronic and molecular simulation; the reader is referred to Reference 2 for a detailed discussion of nanoscale characterization methodologies.

The major approach followed throughout this dissertation is to use force-distance measurements as a tool to develop physical intuition and molecular design principles for engineering nanomaterials at the molecular level. In particular, we study bio-inspired adhesive peptides [3] and ionic liquids [4, 5], as model systems, with an aim of developing broader

predictive frameworks that enable tuning electrostatic interactions in confined soft matter. Over the longer term, we envision that this work could enable the creation of ionic liquids that will find use in advanced supercapacitors for transportation applications and bio-inspired surgical adhesives for replacing damaging screws in joint repair procedures.

2.1 Overview of intermolecular interactions and surface forces

Nature features four distinct, fundamental forces: gravity, the strong nuclear force, the weak nuclear force, and electromagnetic forces. All intermolecular interactions are electromagnetic in nature. Despite this common origin, intermolecular interactions cannot readily be analyzed using a single, universal interaction potential, because a complex interplay of static and dynamic electromagnetic effects influence the range and magnitude of intermolecular interaction forces [2]. Thus, intermolecular interactions are most easily modeled and understood by using a superposition of distinct interaction potentials that independently account for these differing effects, as discussed in Sections 2.2–2.4.

The comprehensive analysis of all intermolecular interactions with a single framework is possible, in principle. However, this approach would necessitate the explicit solution of Schrodinger's equation [6] for tremendously complicated systems of particles, a currently insurmountable task that likely remain such for the foreseeable future. The approach followed in this dissertation is to categorize intermolecular interactions into distinct classes that arise from different aspects of the total intermolecular interaction – for example, treating electrostatic and van der Waals interactions independently – while taking care to avoid double-counting any contributions to the total interaction. Figure 2.1 illustrates the various intermolecular interactions that are discussed throughout this dissertation, and provides a qualitative representation of strengths and ranges of common colloidal forces.

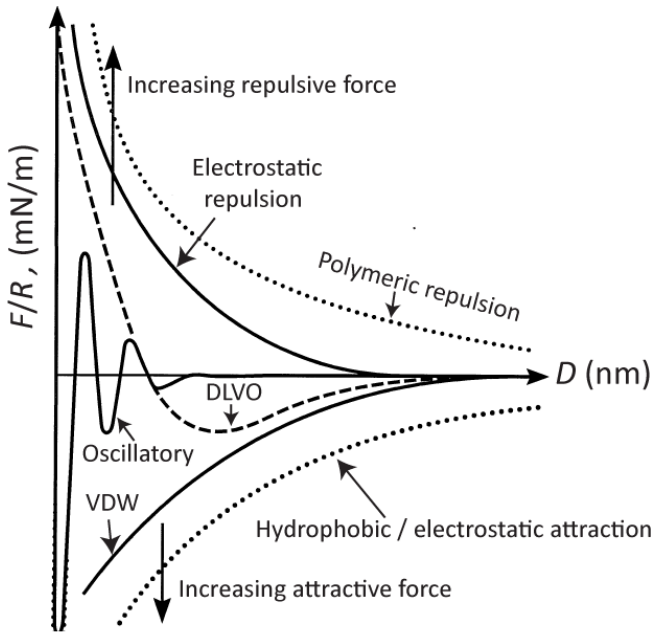

Figure 2.1 Schematic representation of the common colloidal interaction forces, where the y-axis is the interaction force between two crossed cylinders normalized by the radius of curvature, and the x-axis is the surface separation distance in nanometers. Repulsive forces are positive and attractive forces are negative. Figure adapted from Leckband and Israelachvili [7].

In Sections 2.2 and 2.3, we introduce electrostatic and van der Waals interactions by first describing the interaction free energy between two isolated particles, $w(r)$ (J), where r (m) is the separation distance between the centers of the particles. The force can then be calculated from the interaction energy via [2]:

$$f = -\frac{\partial}{\partial r}(w(r)) \tag{2.1}$$

If the characteristic potential for the interaction energy between pairs of particles is known, then interaction forces between surfaces and other large many-particle objects can be approximated by summing up the interaction energies between all pairs of particles [2]:

$$E = \sum w_{ij}(r_{ij}) \tag{2.2}$$

Where w_{ij} (J) is the interaction energy between two particles that are separated by distance r_{ij} (m). In practice, this summation is too complex to routinely evaluate, so various approximations for predicting surface interaction energies have been developed, and the interaction force between two objects or surfaces can be evaluated via [2]:

$$F = -\frac{\partial}{\partial D}(E(D)) \tag{2.3}$$

Where D (m) is the separation distance between the surfaces, and E (J) is the interaction potential energy between the surfaces. In this dissertation, we distinguish between intermolecular and surface forces, where we specifically refer to the force between to particles and/or surfaces, and intermolecular and surface interactions, where we more generally refer to the consequences of forces on molecular systems.

One of the major breakthroughs for the study of colloidal interactions occurred in the middle of the twentieth century, when the continuum interaction potential known as DLVO (Derjaguin-Landau-Verwey-Overbeek) theory [8, 9] gained wide acceptance. DLVO theory models colloidal interactions as a superposition of van der Waals and electric double-layer interactions, and Equation 2.4 shows the general form of the DLVO potential for interaction forces, $F(D)$, between two macroscopic surfaces in a crossed cylinder geometry (normalized by the geometric mean cylinder radius, R):

$$\frac{F(D)}{2\pi R} = E_{\mathrm{EDL}}(D) + E_{\mathrm{vdW}}(D) \tag{2.4}$$

Where R (m) is the average radius of the two cylinders, E_{EDL} is the diffuse electric double-layer interaction energy and E_{vdW} is the van der Waals interaction energy between the two surfaces across an intervening medium. The power of Equation 2.4 lies in the fact that the interaction forces between two macroscopic cylindrical surfaces, which is an experimental observable, is directly related to the interaction energy between two infinite flat planes. This relationship is obtained via the Derjaquin approximation [2], which becomes exact in the limit of macroscopic surface curvatures, where $R >> D$:

$$E_{plane}(D) = \frac{F_{cylinder}}{2\pi R} \tag{2.5}$$

Where W_{flat} (J) is the interaction free energy between two flat surfaces, $F_{cylinder}$ (N) is the interaction force between two orthogonal, crossed cylinders, R (m) is the radius (or average radius) of the cylinders, and D (m) is the separation distance between the two surfaces.

DLVO theory provides a quantitative, testable framework for studying the relationships between surface and solution properties and interactions between particles and surfaces. DLVO theory has also been expanded to account for interactions involving: polymers (both grafted to surfaces and dispersed in solutions), hydrogen bonding interactions between water and hydrophilic or hydrophobic groups, adsorbed layers of ions or molecules, and other increasingly complex interaction forces, as briefly overviewed in Section 2.4.

2.2 Electrostatic forces

The overarching theme of this dissertation is the development of approaches for rationalizing electrostatic interactions in solid-liquid interfaces containing high concentrations of ions or charged functional groups. In particular, we show that the typical mean field theories

that are used to describe electrostatic interactions in ideal, dilute electrolyte solutions can be applied to highly concentrated, correlated fluids, like ionic liquids, when the theoretical frameworks are reformulated in terms of local charge imbalances. Modeling electrostatic interactions in high concentration electrolytes via local charge imbalances is a departure from previous approaches, where mean field theories aim to capture the behavior every ion and/or functional group [10–12]. Further, we demonstrate that local charge imbalances play an important role in driving the energetics of intermolecular cohesion in bio-inspired adhesive peptides.

This section outlines the fundamental principles and equations underlying the Poisson-Boltzmann equation, since the Poisson-Boltzmann equation is our common starting point for treating electrostatic interactions in confined soft matter systems.

At the most elementary level, the electrostatic interaction force between isolated charged particles is described by Coulomb's law:

$$F_{el} = \frac{q_1 q_2}{4\pi\varepsilon_0 r^2} \tag{2.6}$$

Where q (C) is the particle electric charge, ε_0 (F/m) is the permittivity of free space, and r (m) is the separation between the charged particles. Like gravitational interactions, electrostatic interactions exhibit spherical symmetry, leading to an interaction force that falls off as $1/r^2$, extending the influence of electrostatic interactions to much longer ranges than other intermolecular interactions, such as van der Waals forces. Electrostatic interactions are also much stronger than other non-bonding intermolecular forces, with vacuum interaction energies that routinely approach the energies of covalent bonds. For example, a sodium chloride ion pair in vacuum exhibits an interaction free energy on the order of 200 k_BT – or about 200 times stronger than the randomizing effect of thermal energy at 295 K.

Taken together, the long range of influence and high interaction free energy makes electrostatic interactions a dominant intermolecular influence. However, these same two characteristics make systems that are composed of extremely high concentrations of charged particles extremely difficult to treat computationally.

In contrast to covalent interactions, electrostatic interaction free energies are strongly influenced by immersing charged species in condensed media, since charged particles polarize surrounding atoms and molecules, resulting in the formation of reaction fields that reduce the free energy that charged particles can contribute to the formation of Coulomb bonds. The net result is to reduce the electrostatic interaction energy between two ions or functional groups by a factor of $1/\varepsilon$ when they are immersed in a medium, relative to the electrostatic free energy of the same interaction in vacuum, where ε is the static relative dielectric permittivity of the medium.

The static dielectric permittivity is an important material property that depends on the polarizability of the atoms that make up the medium, as well as the presence of any molecular dipoles, with ε increasing as the atomic polarizability and molecular dipole density increases. For comparison, the dielectric permittivity for linear alkanes and nonpolar, hydrophobic regions of proteins is about $\varepsilon \approx 2$ at room temperature, while the room temperature permittivity for bulk water is $\varepsilon = 78$ [2]. Thus, the 200 k_BT interaction energy of a sodium chloride ion pair in vacuum falls to an energy of 3–5 k_BT in water, which explains the moderate solubility of many salts in water. Interestingly, the dielectric permittivity of pure salts, including ionic liquids, are modest, typically ranging from $\varepsilon = 7–15$ [13]. While these values of ε may seem counterintuitive for a medium that is composed purely of ions, the dielectric permittivity

values for salts are primarily determined by atomic polarizabilities, since strong Coulombic interactions between ions drive local electroneutrality.

Since electrostatic interactions are pairwise additive – electrostatic interactions obey the superposition principle – the interaction forces between charged particles can be calculated by summing Coulomb's law for each pair of particles. However, this approach quickly becomes unwieldy for many particle, soft matter systems that prominently feature fluctuations and disorder. The concept of an electric field is essential for describing the combined electrostatic influence exerted by large collections of particles, such as liquids or surfaces. The electric field is the force that would be exerted on any test particle that is placed in a specific region of space, resulting from the electrostatic influence of all surrounding particles:

$$\mathbf{F}_{\text{el}} = q\mathbf{E} \tag{2.7}$$

Where q (C) is the test particle charge, and $\boldsymbol{E}$ (V/m) is the vector electric field. By extension, the total electrostatic force on an extended charged surface can be calculated if the electric field distribution is known, by replacing q in Equation 2.7 with the charge density of a surface. As a result, calculating electrostatic interaction forces between charged surfaces amounts to determining surface charge densities and electric field distributions.

As a general rule, electromagnetic interactions in soft matter systems are classical in nature, so Maxwell's equations – Equations 2.8–2.11 – provide the fundamental relationships between electric fields and the distributions of charged particles:

$$\nabla \cdot \mathbf{E} = \frac{\rho}{\varepsilon_0} \tag{2.8}$$

$$\nabla \times \mathbf{E} = -\frac{\partial \mathbf{B}}{\partial t} \tag{2.9}$$

$$\nabla \cdot \mathbf{B} = 0 \tag{2.10}$$

$$c^2 \nabla \times \mathbf{B} = \frac{\partial \mathbf{E}}{\partial t} + \frac{j}{\varepsilon_0} \tag{2.11}$$

Where **E** (V/m) is the vector electric field, ρ (C/m^3) is the electric charge density, **B** (T) is the vector magnetic field, **j** (A) is the electric current and c (m/s) is the speed of light.

In the absence of externally varying electric and magnetic fields, Maxwell's equations reduce into a single equation, Poisson's equation:

$$\nabla^2 \psi(x, y, z) = -\frac{\rho}{\varepsilon_0} \tag{2.12}$$

$$\mathbf{E} = -\nabla \psi(x, y, z) \tag{2.13}$$

Here ψ (V) is the scalar electric potential. Unless otherwise noted, it is assumed that ionic distributions within electric double-layers are in thermal equilibrium with a bulk reservoir, meaning that the concentration of each ionic species follows the Boltzmann distribution:

$$n = n_0 \exp\left(\frac{-ze\psi(x, y, z)}{k_B T}\right) \tag{2.14}$$

Where n (particles/m^3) is the potential-dependent ionic concentration of each ionic species, n_0 (particles/m^3) is the bulk ionic concentration of that species, z is the ion valence, e (C) is the elementary charge, k_B is Boltzmann's constant, and T (K) is the temperature. The term $ze\psi$ (J) is the electric potential energy of an ion of valence z in a field of strength ψ.

Inserting Equation 2.14 into Equation 2.12 yields the Poisson-Boltzmann equation, which for a 1:1 electrolyte composed of a monovalent salt, such as NaCl in water, is:

$$\nabla^2\psi(x,y,z) = \frac{n_0 e}{\varepsilon_0}[\exp(\frac{-e\psi(x,y,z)}{k_B T}) - \exp(\frac{e\psi(x,y,z)}{k_B T})] \qquad (2.15)$$

The Poisson-Boltzmann equation has broad applicability within the field of colloid science [2], and is used to address problems ranging from predicting the stability of colloidal suspensions, to calculating the expected energy density of electric double-layer capacitors.

When charged surfaces are immersed in electrolyte solutions containing dissociated ions, the surfaces attract counter-ions and repel co-ions. In the absence of thermal fluctuations, these perturbed ionic concentrations would be confined to a single layer that is adjacent to the surface, named the Helmholtz layer. In reality, thermal fluctuations provide an osmotic driving force that acts to remix the electrolyte solution, leading to a smearing out of the ionic atmosphere, called a diffuse double-layer. Equation 2.15 enables one to quantify the balance of electrostatic and osmotic forces and describes the ranges and magnitudes of the electric field decay away from charged surfaces in electrolyte solutions. Strictly, this nonlinear, partial differential equation can be numerically solved. In practice, the Poisson-Boltzmann equation is often linearized and simplified with assumptions to yield physically insightful analytical solutions [2]. The latter approach is taken throughout this dissertation, with the goal of obtaining general physical insight to aid in the design of advanced materials.

In this work, the foundational equation that is used to model force-distance profiles between charged surfaces is the 1-D linearized Poisson-Boltzmann equation, also known as the Debye-Hückel approximation, for a charged plane that is immersed in a 1:1 electrolyte:

$$\frac{\partial^2 \psi}{\partial z^2} = \kappa^2 \psi \tag{2.16}$$

With the solution under constant potential boundary conditions:

$$\Psi = \Psi_0 e^{-\kappa z} \tag{2.17}$$

$$\kappa^{-1} \equiv \sqrt{\frac{\varepsilon \varepsilon_0 k_B T}{2nq^2}} \tag{2.18}$$

Here κ^{-1} (m) is the Debye screening length, z (m) is the distance from the charged surface, ψ_0 (V) is the surface electrostatic potential, n (particles/m^3) is the concentration of dissolved ions, q (C) is the ion valence, and ε is the static dielectric permittivity of the intervening medium. This solution assumes that the surface potential decays to ψ = 0 V far from the surface, and the characteristic length scale of this potential decay is the Debye length. The Debye length depends inversely on the total concentration and valence of dissolved ions for strongly dissociated, dilute electrolyte solutions. For weakly dissociated electrolyte solutions that exhibit significant ion pairing and/or electrostatic correlations, the Debye length is no longer directly proportional to the ionic strength. Examples of weakly dissociated electrolytes include: weak acids, weak bases, ocean water, ionic liquids, battery electrolytes, and extremely high concentration electrolyte solutions.

SFA experiments implement two surfaces, typically in the orthogonal, crossed cylinder geometry. To obtain the appropriate interaction potential for SFA experiments, the linear

Poisson-Boltzmann equation is solved for two flat plates approaching one another across an intervening electrolyte solution, where the electrostatic potential or charge density of each of the two surfaces is fixed. The Derjaguin approximation, Equation 2.5, is then used to relate the interaction energy between the hypothetical flat plates to the actual measured interaction forces between SFA surfaces. When the surfaces are initially far apart, at separation distances, D (m), that greatly exceed the Debye length, κ (m), each surface forms an independent electric double-layer that can be modeled using Equations 2.16–2.18. As the two surfaces are brought together, the diffuse electric double-layers begin to overlap, leading to interactions between the two surfaces, E_{EDL} (J), that are attractive or repulsive, depending on the potential and/or charge densities of the surfaces.

The most general SFA electric double-layer interaction potential that can be derived from the linearized Poisson-Boltzmann equation is for two symmetric planes interacting with constant potential boundary conditions [14]:

$$\frac{F_{\mathrm{cylinder}}}{2\pi R} = E_{\mathrm{EDL}} = \frac{4e^2 n}{k_{\mathrm{B}} T \kappa} \frac{\psi^2 (1 - \exp(-\kappa D))}{\exp(\kappa D) - \exp(-\kappa D)} \tag{2.19}$$

Where the Debye length, κ^{-1} (m), is defined above in Equation 2.18. This equation is extremely accurate for surface potentials of ψ < 25 mV. However, this equation can also be applied to situations where surface potentials are as high as 200 mV [2, 13], as long as the surface forces are only modeled in the asymptotic limit of $D >> \kappa^{-1}$, where:

$$E_{\mathrm{EDL}} \approx \frac{4e^2 n}{k_{\mathrm{B}} T \kappa} \psi^2 \exp(-\kappa D) \tag{2.20}$$

This approach can be extended to derive electric double-layer interaction potentials for more complex scenarios, such as for surfaces with dissimilar surface charges or for surfaces that follow constant charge density boundary conditions. When necessary, these approaches are presented and discussed at the relevant section of the dissertation.

The interaction force between overlapping electric double-layers is a balance of the entropic penalty associated with confining ions next to charged surfaces, with the favorable or unfavorable electrostatic free energy associated with ion-surface and surface-surface interactions. For the case of symmetric surfaces, Equations 2.19 and 2.20, the repulsive interaction is entirely osmotic in nature, as the entropic penalty associated with constricting the spatial extent of each surface charge compensating double-layer is always lower than the free energy penalty that would result from surface-surface electrostatic repulsions.

For dissimilar surfaces, the interaction potential is often dominated by the (repulsive) osmotic contribution for surfaces with charges of the same sign, while the interaction potential is typically dominated by the (attractive) electrostatic term for oppositely charged surfaces. When oppositely charged surfaces are brought together, the osmotic term can also be attractive, when counter-ions are released into the reservoir, but this osmotic attraction is typically much smaller than the associated electrostatic attraction.

The above equations provide a powerful framework for understanding and tuning electrostatic interactions in confined soft matter. For example, the Debye screening length provides a direct measure of the degree of electrostatic correlations within electrolyte solutions. However, these mean field equations inherently break down as surfaces are approached to separation distances that are significantly smaller than a Debye length. At molecular distances, specific intermolecular interactions begin to dominate surface forces,

such as the cation-π interactions, and steric (oscillatory) ion-binding interactions discussed below. Further, electrostatic interactions are only one contributor to the total colloidal interactions between surfaces. A thorough understanding of van der Waals forces and short range molecular forces is required to effectively tune the properties of nanomaterials.

2.3 van der Waals forces

van der Waals forces originate from the correlation of molecular dipolar and/or electronic fluctuations, and encompass all intermolecular interactions that do not directly result from covalent bonding or the presence of electrostatic monopoles [2]. Much like the gravitational interaction, van der Waals interactions occur between all types of matter and impact the properties of all nanomaterials to varying degrees. Thus, van der Waals interactions are the key interaction that determines the properties of neutral molecules and surfaces. However, in the presence of charged groups, van der Waals interactions are much weaker than electrostatic interactions and operate over shorter ranges, so van der Waals forces are frequently secondary to electrostatic forces between charged surfaces.

Between isolated pairs of particles, van der Waals interactions exhibit a characteristic $1/r^6$ distance dependence and can be broken down into three distinct contributions: dipole-dipole orientation interactions, dipole-induced dipole interactions, and dispersion (induced dipole-induced dipole) interactions. For two polar molecules, the van der Waals interaction free energy is given by [2]:

$$w_{\mathrm{VDW}}(r) = -\frac{[C_{\mathrm{orient}} + C_{\mathrm{ind}} + C_{\mathrm{disp}}]}{r^6} \tag{2.21}$$

$$= -[\frac{u_1^2 u_2^2}{3k_B T} + (u_1^2\alpha_{02} + u_2^2\alpha_{01}) + \frac{3\alpha_{01}\alpha_{02} h\nu_1\nu_2}{2(\nu_1+\nu_2)}] / (4\pi\varepsilon_0)^2 r^6 \tag{2.22}$$

Where C_{orient} (J) is the orientation interaction coefficient, C_{ind} (J) is the dipole-induced dipole interaction coefficient, C_{disp} (J) is the dispersion interaction coefficient, u (D) is the molecular dipole moment, α (m^3) is the (volume) molecular polarizability, ν (s^{-1}) is the molecular ionization frequency, and h (J s) is Planck's constant.

The dispersion contribution to van der Waals interaction occurs between all atoms and molecules and dominates the van der Waals interactions between neutral particles, except for small molecules with unusually high dipole moments, like water and hydrazine [2]. Physically, the dispersion interaction is quantum mechanical in origin; all molecules and atoms experience electronic fluctuations that result in instantaneous polarizations of the electron densities relative to atomic nuclei, and the correlation of these electronic fluctuations between particles leads to attractive dispersion interactions. Dispersion interactions are typically on the order of 1 k_BT for isolated molecule pairs, but can exceed 10 k_BT for the interaction free energy of a molecule with surrounding molecules in condensed phases, as evidenced by the 212 °C boiling point of dodecane at standard pressure.

van der Waals interactions between isolated particles in vacuum are always attractive. However, van der Waals interactions can lead to effective "repulsions" between particles in condensed phases, when the dielectric properties of the medium is intermediate to that of the particles. This is analogous to the apparent "repulsion" that gravitational interactions induce between two masses of differing densities that are immersed in a medium of intermediate density, for example lead and Styrofoam balls that are immersed in water as a contact pair and separate upon bring released.

Unlike electrostatic interactions, van der Waals interactions exhibit complex, non-additive, many body effects that significantly impact interaction free energies. As a result, the

most accurate van der Waals interaction potentials, E_{vdW}, that are used to model the interaction forces between extended surfaces across intervening media, such as the Lifshitz theory [15], are derived from measured bulk properties, such as refractive index and relative permittivity. In this dissertation, the van der Waals interaction energy between two flat planes interacting across a continuum medium is given by Equations 2.23–2.25 [2]:

$$E_{\mathrm{vdW}} = -\frac{A_{\mathrm{H}}}{12\pi D^2} \tag{2.23}$$

$$A_{\mathrm{H}} = A_{\nu=0} + A_{\nu>0} \tag{2.24}$$

$$\approx \frac{3}{4} k_B T \left(\frac{\varepsilon_1 - \varepsilon_3}{\varepsilon_1 + \varepsilon_3}\right)\left(\frac{\varepsilon_2 - \varepsilon_3}{\varepsilon_2 + \varepsilon_3}\right) + \frac{3h\nu_{\mathrm{e}}}{8\sqrt{2}} \frac{(n_1^2 - n_3^2)(n_2^2 - n_3^2)}{(n_1^2 + n_3^2)^{1/2}(n_2^2 + n_3^2)^{1/2}[(n_1^2 + n_3^2)^{1/2} + (n_2^2 + n_3^2)^{1/2}]} \tag{2.25}$$

Where A_{H} (J) is the Hamaker constant, $A_{\nu=0}$ (J) is the zero frequency (dipolar) contribution to the Hamaker constant, $A_{\nu>0}$ (J) is the electronic contribution to the Hamaker constant, ε_1 is the dielectric permittivity of the first surface, ε_2 is the dielectric permittivity of the second surface, ε_3 is the dielectric permittivity of the intervening medium, n_1 is the refractive index of the first surface, n_2 is the refractive index of the second surface, n_3 is the refractive index of the intervening medium, and ν_e (s^{-1}) is the main electronic absorption frequency of the system. These equations are derived from the Lifshitz approach for modeling van der Waals interactions, and the Hamaker constant depends on a combination of the continuum properties of each of the three materials involved in the van der Waals interactions, as opposed to being a specific property of each independent surface and/or medium. The Derjaguin approximation (Equation 2.5) is then used to relate the interaction energy between flat planes to the surface forces between orthogonal cylinders.

Notably, van der Waals interactions between extended surfaces exhibit a $1/D^2$ dependence, which is longer range than the $1/r^6$ dependence of particle-particle van der Waals forces, due

to the additive effect of many interacting particles. Equation 2.25 provides a quantitative foundation for understanding the interaction forces that drive the aggregation of unstable colloidal suspensions, such as the long range attractive interaction forces that drive aggregation in suspension of neutral metal nanoparticles [2]. However, van der Waals interactions are typically shorter range than electrostatic interactions between charged surfaces in dilute electrolyte solutions, and strong electrostatic correlations may overwhelm van der Waals interactions in moderate to high concentration electrolytes.

The Hamaker constant in Equation 2.23 can even be used as a qualitative estimate of the relative surface energies of solid surfaces, by considering a system that consists of two solid surfaces of the material with air as the intervening medium. However, this approach is challenging, as an interaction cut-off distance must be assumed, since Equation 2.23 has a $1/D^2$ distance dependence, which asymptotes to an interaction free energy of $-\infty$ in the limit of $D \rightarrow 0$ nm. Typically, cut off distances of 2 Å yield interaction energies that are in reasonable agreement with measured solid surface energies [2]. van der Waals interactions between extended surfaces can also be repulsive, termed a disjoining pressure. As can be seen from Equation 2.25, this situation occurs when the dielectric properties of the medium is intermediate to that of the two surfaces.

2.4 Short range, specific intermolecular interactions

When the separation distance between two macroscopic surfaces approaches molecular dimensions, the assumptions underlying mean-field theories of electrostatic and van der Waals interactions break down. Over molecular length scales, specific intermolecular interactions, like hydrogen bonding interactions, specific Coulombic bonding interactions and cation-π interactions determine the properties of most nanomaterials.

Currently there is no general framework analogous to the Poisson-Boltzmann equation or the Lifshitz theory that can be applied to model surface interactions for such closely spaced surfaces. Instead, combinations of empirical interaction potentials and phenomenological arguments have proven to be the most effective methods to understand and predict the behavior of short range interactions, such as the layering of ionic liquid ions and the self-assembly properties of proteins. This section addresses the major classes of short range, specific intermolecular interactions that are of relevance for this dissertation.

2.4.1 Ion correlation interactions

When charged surfaces approach to separation distances that are much shorter than a Debye length, ions become confined to increasingly small regions of space. In fact, the local ionic concentration of even ideal, dilute electrolyte solutions, can be more than three orders of magnitude larger within confined interfaces than in bulk solutions, as two charged surfaces are approached to distances of $D << \kappa^{-1}$. Thus, even dilute electrolyte solutions, such as 1 mM sodium chloride in water, can quickly become non-ideal, with local charge densities in excess of 1 M for moderate surface potentials of around 100 mV [2]. Electrostatic correlations are compounded as surface potentials or bulk ionic strengths are increased, and short range ionic correlations are prominent in the surface forces experiments across ionic liquids and peptides that are described in Chapters 3–6.

In interfaces containing very high local ionic concentrations, ions are confined close enough to charged surfaces and other ions that electrostatic interaction energies drastically exceed the randomizing influence of thermal energy. The characteristic distance where the Coulomb potential energy between two elementary charges is equal to the randomizing influence of thermal energy is known as the Bjerrum length:

$$l_B = \frac{e^2}{4\pi\varepsilon_0\varepsilon k_B T} \tag{2.26}$$

Where e (C) is the electron charge, ε_0 (F/m) is the permittivity of free space, ε is the medium permittivity, k_B (J/K) is the Boltzmann constant, and T (K) is the temperature.

Although strictly a mean field theory that depends on the bulk dielectric permittivity of the intervening medium, ε, the Bjerrum length routinely proves to be surprisingly accurate for predicting the length scales over which electrostatic correlations persist, as discussed in greater detail in Chapter 4. Thus, when ions and/or surfaces begin to approach to distances that are shorter than approximately l_B, the ions begin to adopt charge-ordered configurations, and surface charge densities and ionic distributions begin to deviate from the predictions of smeared-out, mean-field models [16].

The most common consequence of electrostatic correlations is the emergence of an additional strong, short range, interaction force that exhibits non-monotonic, "oscillatory" behavior, where strongly repulsive interaction regimes alternate with strongly attractive interaction regimes, as shown in Figure 2.2. For electrolyte solutions that feature prominent electrostatic correlations, these short range oscillatory forces originate from the compression of distinct ion layers, with the sudden attractive instabilities in force-distance profiles corresponding to the abrupt removal of mixed cation-anion layers. Each subsequent layer requires higher forces to remove from the interface than the previous layer, as ion layers that are closer to charged surfaces are more highly ordered and enhanced in surface counter-ions [2]. Typically, between 1–2 ion layers per surface are unable to be fully removed from confined interfaces using experimental techniques like the SFA and AFM, and these ion layers are known as condensed, bound counter-ions. Short range oscillatory force-distance profiles

are a common feature of the surface forces measured across confined ionic liquids and highly concentrated electrolyte solutions, and are discussed in Chapters 3–6.

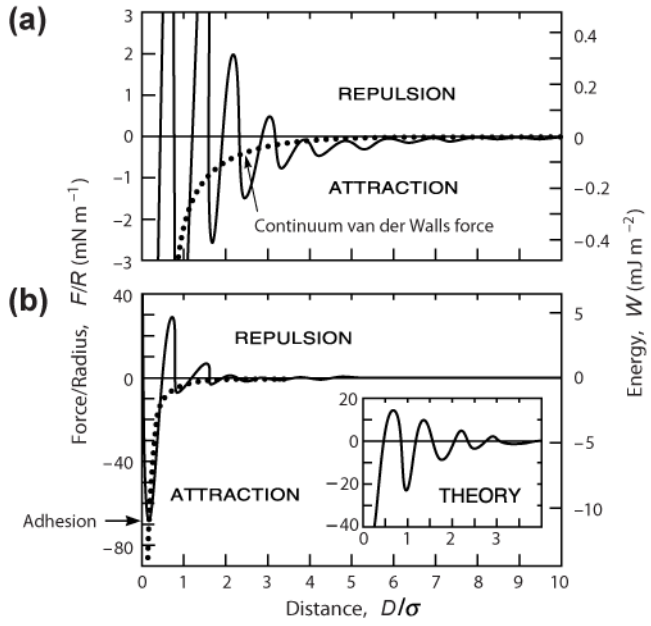

Figure 2.2. Representative "oscillatory" force-distance profile measured across octamethylcyclotetrasiloxane (OMCTS) between two cylindrical mica surfaces. The solid lines represent experimental data, and the dashed line are predicted DLVO forces. Oscillations result from ordering of the quasi-spherical OMCTS molecules when confined to molecular films, and the characteristic spacing of the oscillations is in agreement with the molecular size of OMCTS. Similar effects are also seen when ions are confined between two charged surfaces. Figure reprinted from *Intermolecular and Surface Forces, 3rd Ed.* by Jacob Israelachvili [2].

Short range electrostatic interactions between highly charged surfaces of opposite sign are often more attractive than the predictions of mean-field theory, possibly resulting from strong attractions between opposing bound ion layers [2]. Experimentally, this effect has been observed most prominently in electrochemically active interfaces [8, 17], as discussed in Section 2.5.1. On the theoretical front, some computational studies predict that short range ion correlation forces could also cause non-mean field attractive interactions between surfaces with like charges [16], but direct force-distance measurements supporting such proposals are

lacking [2], perhaps due to the dominance of the long range electrostatic and osmotic repulsions.

2.4.2 Cation-π interactions

As discussed in Chapter 6, cation-π interactions play a key role in the short range cohesive binding of bio-inspired adhesive peptides. Cation-π interactions are electrostatic in origin and occur between cations and electron-rich π-orbitals [18–20]. These interactions share conceptual connections with van der Waals interactions, as the cation-π interaction originates from the polarization of a net neutral π-bonding systems, such as aromatic rings. However, cation-π interactions require the presence of an electrostatic monopole.

Cation-π interactions are significantly stronger in the gas phase than in condensed phases, and cation-π interactions still exceed the strength of hydrogen bonds, and possibly even charge-charge interactions, in aqueous solutions [18, 21]. Notably, especially strong binding occurs when cations interact with the delocalized π-orbitals perpendicular to the plane of aromatic rings [20]. Like other polarization interactions, cation-π interaction strengths are highly sensitive to the size and charge density of cations, with small cations and localized charge densities increasing binding strengths. Additionally, cation-π interactions are strongly impacted by chemical substituents that influence the electron densities of π-bonding molecular orbitals, with electron withdrawing groups decreasing interaction strengths, and electron donating groups increasing interaction strengths [20].

As for other short range specific interactions, the strengths of cation-π induced surface interactions are difficult to predict *a priori*. In fact, much of the current understanding of cation-π binding strengths in condensed phases is either extrapolated from gas phase experiments and calculations [18–21], or inferred from the proximity of aromatic and cationic

amino acids in protein crystal structures [22–24]. Thus, it remains unclear whether these insights are directly applicable to rationalizing cation-π energetics at interfaces. In Chapter 6 we address the relative interaction strengths of interfacial cation-π interactions, and demonstrate that hydroxyl- substituents can be used to tune cation-π interactions in bio-inspired adhesives, a molecular design strategy that was previously unknown.

2.4.3 Steric and polymeric forces

Neutral molecules, like dodecane and other linear alkanes, interact with surfaces via van der Waals interactions that can be strong enough to induce the formation of quasi-ordered, layered molecular structures [2, 25, 26], where the first molecular layer of liquid that is in contact with a solid surface binds strongly enough to dramatically reduce the rotational and translational entropy of liquid molecules. These bound molecules then weakly template the orientation of adjacent layers, although this effect is weaker than the first bound layer. Typically, surface-induced layering persists between 3–5 molecular diameters away from the surface, at which point the liquid molecules exhibit bulk-like behavior [25–27].

Surface-induced molecular templating is analogous to the ion correlation interactions discussed in Section 2.4.1, resulting in similar "oscillatory" force-distance profiles as surfaces are brought to molecular separations, as illustrated in Figure 2.2. Oscillatory forces have also been observed across a variety of polar molecules, including water [27], where this forces is known as a hydration repulsion and is driven by hydrogen bonding. The ranges and magnitudes of these interactions are highly sensitive to the strength of molecule-surface interactions, and can be surprisingly similar to the range and magnitude of ion correlation forces. In principle, such structural forces will have a large impact on colloidal stability and surface forces. However, oscillatory structural forces require the presence of extended,

molecularly smooth solid surfaces, which are not typical characteristics of real colloidal systems, as molecular scale roughness and/or surface thermal fluctuations, like capillary waves, smear out surface ordering interactions [2]. For real colloidal systems, oscillatory structural forces are typically "smeared out" into a weaker, monotonic structural repulsion.

Additionally, polymeric materials, such as proteins, can bind to, or be grafted to, surfaces. As surfaces are compressed to molecular contact, these bound protein and/or polymer chains will be confined into highly restricted molecular configurations, giving rise to short range entropic repulsions between surfaces. Several mean field interaction potentials have been proposed to model the steric repulsion forces that result from the constriction of polymeric materials with differing grafting or binding densities [2].

For example, end-grafted polymers can either exist as "mushrooms" where the polymeric chains are grafted at low densities and neighboring chains do not overlap to reduce the overall configurational entropy. Alternatively, end grafted polymers can exist in the "brush" regime, where extremely high grafting densities cause each chain to strongly overlap with neighboring chains, forcing polymers to extend out into solution. These two situations result in differing interaction potentials, and the polymer chain length, polymer adsorption configuration, polymer grafting density, and a variety of other factors influence the qualitative and quantitative nature of polymeric forces [2].

In Chapters 5 and 6 we present a short discussion of steric interaction forces across densely packed films of solution deposited peptides. For a detailed discussion of polymer "mushrooms," polymer "brushes," and other steric interaction potentials, the reader is referred to Reference 2.

2.4.4 Hydrophilic and hydrophobic interactions

Hydrophobic and hydrophilic interactions originate from the propensity of water to form strong hydrogen bonds with surfaces and other molecules, especially other water molecules. Hydrogen bonds are highly directional and exhibit typical interaction strengths of 5–10 k_BT per hydrogen bond, inducing molecules to preferentially adopt specific orientations. For example, water molecules in ice adopt a tetrahedral crystal structure, where each water molecule participates in two hydrogen bond donating and two hydrogen bond accepting interactions with four distinct surrounding water molecules [28]. In liquid water, hydrogen bonding interactions also induce water molecules to favor specific orientations with surrounding water molecules, with typical water molecules sharing about 3.5 hydrogen bonding neighbors at any moment in time. Hence, water is often viewed as a dynamic, hydrogen bonded network of molecules [2]. Water molecules can also autoionize, freeing a proton that can "hop" through the hydrogen bonding network of water. This proton "hopping" effect is expected to impact hydrophobic and hydrophilic interactions, however few current theories of interaction forces between surfaces account for proton hopping.

Hydrophilic surfaces exhibit strong hydrogen bond donating or accepting interactions with water molecules, causing the first layer of water molecules in contact with hydrophilic surfaces to experience restricted translational and orientational motion [2]. The next layer of water molecules in contact with the surface-bound water is biased towards adopting orientations that facilitate the formation of hydrogen bonds with surface-bound water, but this second layer of molecules exhibits dynamics that are very similar to bulk water. In fact, water already exhibits completely bulk-like behavior and correlations at distances of 2–3 water molecules from the surface [29].

Hydrophilic interaction forces result from repulsive interactions between the surface-bound water layers and/or surface bound ions and molecules of one surface with those on adjacent, opposing surfaces [29]. In essence, hydrophilic interactions are an extension of the steric interactions discussed in Section 2.4.3 but are driven primarily by hydrogen bonding instead of van der Waals interactions. Since hydrogen bonds are strong, specific interactions, hydrophilic repulsions are typically stronger than typical DLVO van der Waals attractions [2], and are thus responsible for the stability of colloidal silica and many other colloidal suspensions. Hydrophilic interactions also play a large role in guiding the self-assembly of proteins, lipids, and other biomolecules, and contribute to the short range steric repulsive forces discussed in Chapters 5 and 6.

The hydrophobic interaction is an attractive interaction that occurs between nonpolar particles and surfaces that are unable to form hydrogen bonding interactions with water molecules [30]. When water molecules come into contact with surfaces or particles that do not offer hydrogen bonding sites, water molecules can either sacrifice hydrogen bonds or restrict molecular motion to ensure that hydrogen bonding sites are pointed away from the nonpolar species at all times [2, 30]. In general, both mechanisms occur, with restricted motion being the larger effect when water comes into contact with small nonpolar solutes, like methane, for example through the formation of clathrates [2], and broken hydrogen bonds becoming the larger effect as the solute size is increased to macroscopic surfaces.

Hydrophobic interactions induce an additional attractive force between nonpolar solutes and/or surfaces that is noticeably stronger than, and extends to longer ranges than, typical van der Waals forces, known as the hydrophobic effect [31]. As a result, the hydrophobic interaction in conjunction with hydrophilic interactions have a large influence on protein

folding and biological self-assembly. Nevertheless, the hydrophobic effect is typically weaker than specific electrostatic interactions, such as Coulomb bridges and cation-π interactions, as discussed in Chapter 6.

Hydrophobic and hydrophilic interactions share a common origin and interaction strength, and both interactions occur concurrently in many biological systems. Thus, determining the balance of hydrophobic and hydrophilic interactions is an important task. Recently, we proposed that the hydrophobic effect and hydrophilic interactions between extended surfaces can be modeled within a single interaction potential framework [32]:

$$E_{Hy}(D) = -2\gamma_i \cdot Hy \cdot \exp(-\frac{D}{D_{\mathrm{H}}}) \qquad (2.27)$$

Where γ_{i} (J/m^2) is the interfacial tension (or average interfacial tension) of the interacting surfaces, *Hy* is the non-dimensional Hydra parameter, and D_{H} (m) is the interaction decay length, which ranges between D_{H} = 0.3–2 nm, depending on the specific system of surfaces. In this framework, *Hy* is indicative of the degree to which hydrophobic or hydrophilic interactions dominate the resultant surface forces, with *Hy* = 1 for the pure hydrophobic effect (i.e., maximally hydrophobic interactions). For *Hy* between 0 and 1, the interaction potential describes system that exhibit partially hydrophobic interactions, and the potential becomes repulsive for *Hy* < 0, which is indicative of hydrophilic interactions.

The utility of the Hydra potential is that this framework could enable one to begin to predict whether hydrophobic or hydrophilic interactions should dominate in a situation of interest. Achieving this goal will require the development of theoretical methods to predict the value of *Hy* and D_H, but many of the fundamental principles underlying the hydrophobic effect and hydrophilic interactions remain an active area of research and discussion.

2.5 Measuring surface forces: The Surface Forces Apparatus

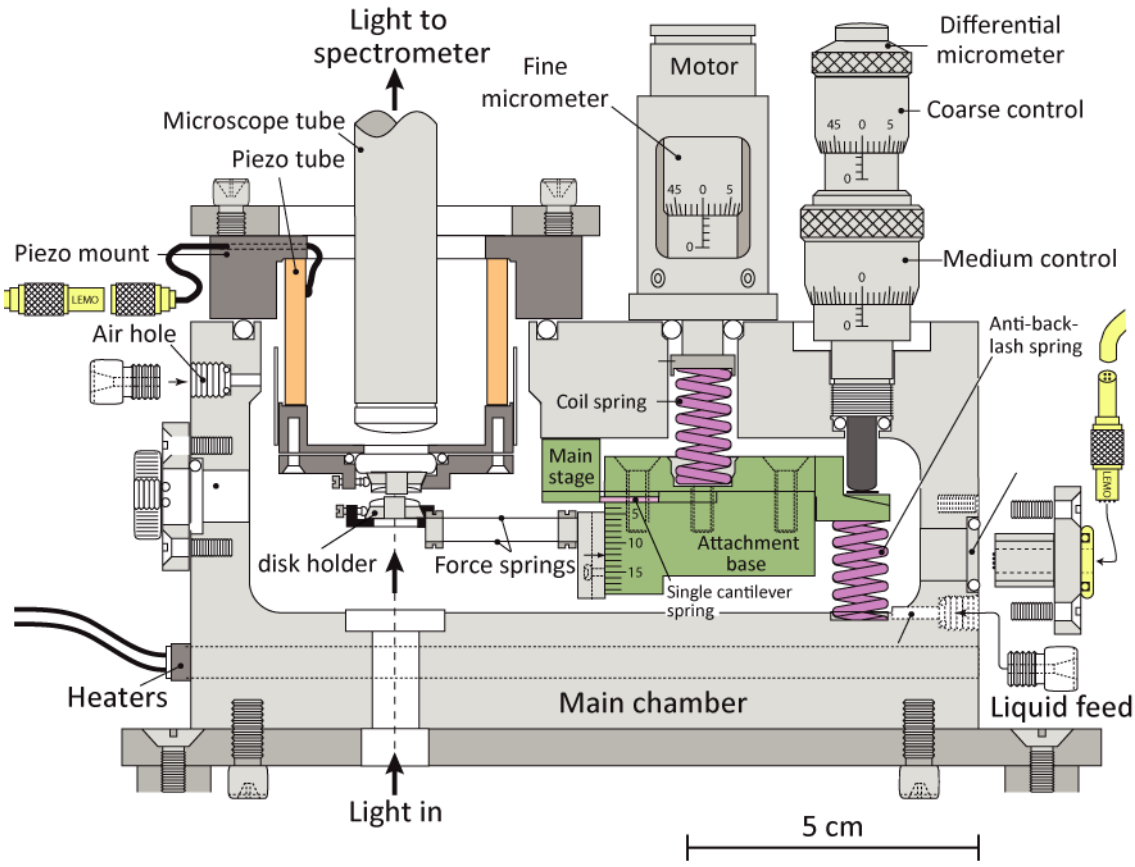

Figure 2.3. Schematic of the SFA 2000 used for all SFA measurements presented in this dissertation. This schematic shows section cut through the center of the apparatus. Figure adapted from Reference 33.

The Surface Forces Apparatus (SFA) technique [33], shown in Figure 2.3, is the primary experimental tool we employed to characterize the electrostatic screening properties of ionic liquids and adhesive performance of bio-inspired peptides. In the broadest sense, the SFA enables one to measure the characteristic force-distance laws, $F(D)$ (N) (Figs, 2.1, 2.2, and 2.4), between two macroscopic surfaces across an intervening medium, with force and

distance resolutions that are relevant for molecular scale phenomena. Beginning with the work of Israelachvili and Tabor [34] in the early 1970s that confirmed the Lifshitz theory of van der Waals forces, the SFA technique has been used to study diverse phenomena, ranging from ligand-receptor binding in biological systems [35] to the room temperature sintering of gold surfaces [36]. In this dissertation, we use the SFA technique to address various fundamental questions that are relevant to materials design, including: How are peptide cohesive interactions impacted by changes to molecular structures? and What is the molecular mechanism of electrostatic screening across confined ionic liquids?

The measurement of normal surface forces is the focus of this dissertation, and Figure 2.4, shows an example of a measured force-distance profile for two surfaces interacting via van der Waals interactions. In practice, SFA force-distance profiles will be composed of a superposition distinct contributions from each of the various interaction forces discussed above (Fig. 2.1), and these distinct force contributions are independently analyzed and discussed in each Chapter. Throughout this dissertation, we adopt the typical convention for the sign of forces illustrated in Figure 2.4, where attractive forces are negative and repulsive forces are positive. The SFA technique can also be used to measure lateral friction forces, and the reader is referred to Reference 33 to learn more about these capabilities.

Conceptually, the SFA technique is closely related to the atomic force microscopy (AFM) technique, with each providing complementary advantages. In particular, SFA measurements feature three distinct advantages when compared to AFM force measurements: the SFA enables direct measurement of absolute surface separation distances and surface deformations using interferometry (AFM provides relative distance information and yields only indirect insight into surface deformations), the SFA employs two extended surfaces, meaning that

continuum models of interaction forces can be used to describe experimental systems, and SFA surfaces can be controlled with arbitrarily slow actuation speeds, enabling the measurement of truly equilibrium force-distance profiles (AFM measurements inherently involve actuating surfaces at tens-to-hundreds of nm per second).

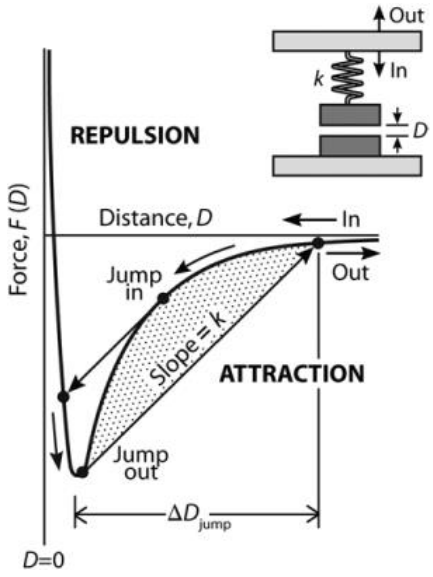

Figure 2.4. Illustration of a representative force-distance law for two extended surfaces that demonstrates attractive instabilities on approach and separation. Figure adapted from Reference 34.

A key strength of the SFA technique is that white light interferometry is used to directly monitor the separation between, and deformations of, extended surfaces to angstrom-scale resolution [37]; the important principles underlying interferometry are discussed in Section 2.5.2. Simultaneously, the deflection of a cantilever spring is used to obtain a force resolution on the order of 1–10 nN. Millimeter-to-micrometer scale control of surface separation distance is obtained using a differential micrometer, and the fine control of surface actuation needed during force-distance measurements is achieved using either a piezoelectric crystal, which enables angstrom-scale distance control, or a motorized micrometer, which enables nanometer-scale distance control.

Normal force-distance profiles are obtained by approaching and separating two surfaces, while simultaneously recording the shift in interference fringes. Normal forces can be obtained through either static or dynamic experiments, and we employed both methods to characterize equilibrium and non-equilibrium forces.

Static force-distance measurements are used to measure equilibrium surface forces. This protocol involves actuating the top surface a specific amount by applying a voltage to the piezoelectric crystal and then leaving the surfaces to equilibrate, typically for times ranging from 10–60 s. For static measurements, the shift in the interference fringe pattern is measured at the end of the specified equilibration time, and the magnitude of the normal surface force acting between the surfaces at each separation is inferred through Hooke's law:

$$F(D) = k_s(D_{expect} - D_{actual}) \tag{2.28}$$

Where k_s (N/m) is the spring constant, D_{expect} (m), is the distance that the voltage ramp is expected to move the top surface, and D_{actual}, is the actual distance that the surface moved.

Dynamic force-distance measurements are obtained by actuating one of the surfaces at a constant rate using either the piezoelectric crystal or motorized micrometer, while continuously measuring the shift in interference fringes. Colloidal forces accelerate and/or decelerate the surfaces and these distance-dependent forces can be inferred by modeling the surface forces measurement using the equation of motion given by [38]:

$$\frac{6\pi R_H R_G \eta \dot{D}}{D} + k_s x + F(D) = 0 \tag{2.29}$$

Where R_H (m) is the harmonic mean radius, R_G (m) is the geometric mean radius, η (Pa·s) is the liquid viscosity, $\dot{D}$ (m/s) is the surface velocity, k_s (N/m) is the spring constant, x (m) is

the instantaneous spring deflection, and $F(D)$ (N) is the actual surface force. In this equation, the first term is the hydrodynamic drag, the second term is the spring deflection, and the third term is the colloidal force acting between the surfaces (the inertial term is neglected in Equation 2.29). This approach can also be used to determine equilibrium surface forces, when the surfaces are actuated slowly enough to enable neglecting the hydrodynamic drag term, i.e., quasi-static force distance measurements.

Since springs are always used to measure force-distance profiles, instabilities occur whenever the slope of the measured $F(D)$ profile exceeds the spring constant, as illustrated in Figure 2.4. In these regions, two surfaces abruptly "jump" towards or away from one another, giving rise to a characteristic adhesive minimum, as we measured across adhesive peptides in Chapters 5 and 6 and characteristic oscillatory force "gaps," as we measured across ionic liquids in Chapters 3 and 4. For adhesive minima, the surface jump distance can be used to obtain highly accurate magnitudes of the adhesive forces. Determining the depth of adhesive instabilities in oscillatory regions of force-distance profiles is more challenging, as discussed in greater detail in Chapters 3 and 4.

2.5.1 The Electrochemical Surface Forces Apparatus (EC SFA)

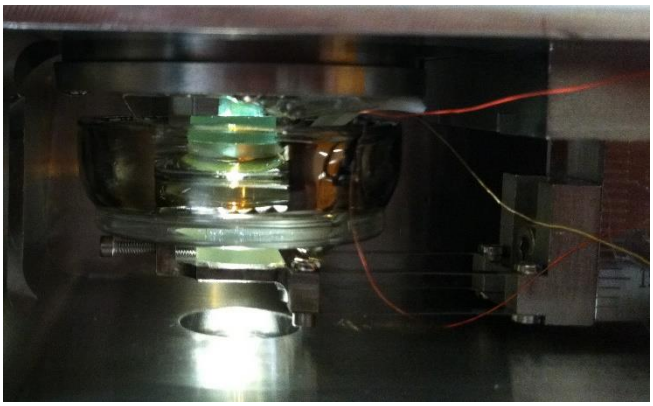

Figure 2.5. Photograph of fully assembled EC SFA setup in the 3 mL silicon dioxide reservoir cup described in the main text. The top surface is a molecularly-smooth gold working electrode surface, the bottom surface is a single-crystalline back silvered mica surface, and the intervening medium is a prototypical ionic liquid.

The work described in Chapter 3 was enabled by extending the SFA 2000 to enable surface forces measurements on small, sub-5 mL volumes of liquids, while simultaneously controlling the electrochemical potential of a molecularly-smooth gold surface that functioned as the top surface in SFA experiments [4]: the EC SFA (Fig. 2.5). This advance was pivotal for the progression of this dissertation, as the work outlined in Chapter 3 directly led to the development of the general approach for understanding electrostatic screening in ionic liquids that is proposed in Chapter 4. The development of the EC SFA further enabled a number of other related research directions, including electrochemical switching of the adhesive properties of redox-active peptides [39], a project that ultimately ended up precipitating the research presented in Chapters 5 and 6.

The concept of seeking *in situ* electrochemical control during SFA measurements can be traced back to the pioneering work of Frechette and Vanderlick in 2001 [8]. Prior to this work, Hillier and Bard reported colloid probe atomic force microscopy (AFM) measurements with *in situ* electrochemical control of a gold electrode surface [40]. Both groups tested the validity

of the classical Poisson-Boltzmann framework for modeling electric double-layer interactions in strongly dissociated, dilute electrolyte solutions and concluded that the long range interaction forces measured at separation distances exceeding one Debye length exhibit excellent agreement with the predictions of mean-field theory. However, both groups reported strong deviations from mean-field theory as surfaces approach molecular contact and attributed these deviations to electrostatic correlations and ion binding interactions.

While successfully proving the feasibility of performing SFA measurements with *in situ* electrochemical control, this initial rendition of the EC SFA [8] necessitated a number of complex fabrication steps that precluded the wider adoption of this promising technique. In 2011, we developed a streamlined approach for setting up EC SFA measurements [41] by combining facile nanofabrication techniques to prepare mica-templated of gold working electrode surfaces with a greatly simplified design for implementing the counter and reference electrodes necessary to perform 3 electrode electrochemical measurements (Fig. 2.6). Additional details of gold surface preparation and a detailed discussion of our EC SFA development efforts can be found in Reference 39. Notably, this EC SFA design still required filling the entire 250 mL SFA chamber with electrolyte solution, which prevented the extension of this methodology to high value materials, like ionic liquids and proteins.

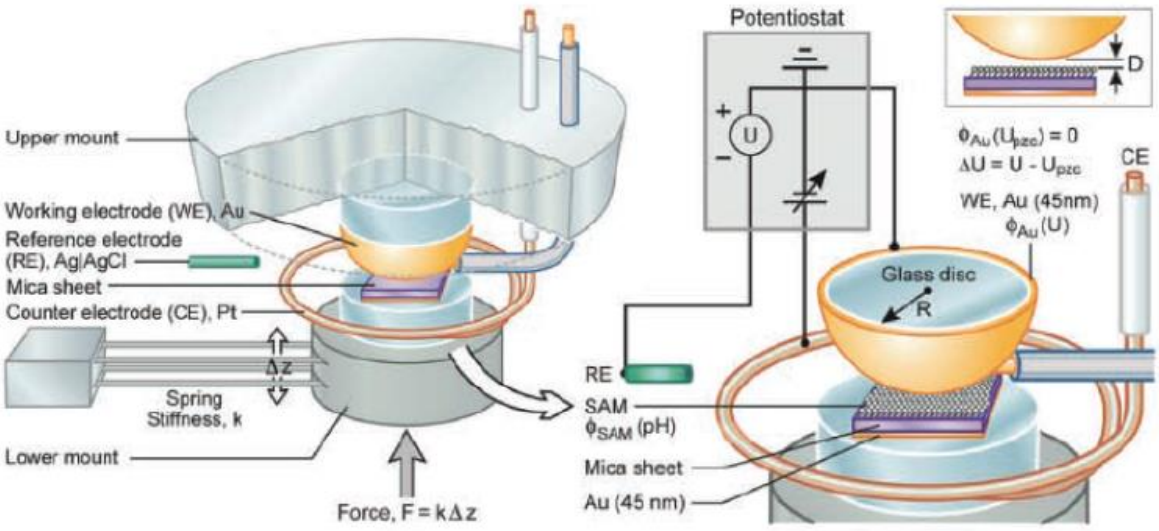

Figure 2.6. Schematic of the electrochemical modification to the Surface Forces Apparatus technique developed in the Israelachvili lab, the EC SFA. Figure adapted from Reference 41.

Over the following year, we further extended the EC SFA technique to enable measurements on liquid volumes as small as 2–3 mL, as depicted in Figure 2.5, and this breakthrough enabled the work described in Chapter 3. This extension was allowed by the incorporation of a counter electrode into a small silicon dioxide glass cup that functions as a liquid reservoir. This was achieved by coating the base of the silica cup with a 15 nm layer of titanium dioxide, followed by a 500 nm layer of platinum via electron beam deposition. The electrical contact with the counter electrode was made by soldering a gold wire to the base of the cup, and the solder contact point was isolated with ultraviolet curing glue.

The top surface in this setup consists of a molecularly-smooth gold surface that functions as a working electrode, while the bottom surface consists of a single-crystalline sheet of back-silvered muscovite mica that was prepared using the standard procedure for preparing mica SFA surfaces. Briefly, a single-crystalline mica sheet (back-silvered) was glued onto a cylindrical SFA disc using UV glue and UV glued into the base of the silicon dioxide cup.

2.5.2 Principles of multiple beam interferometry

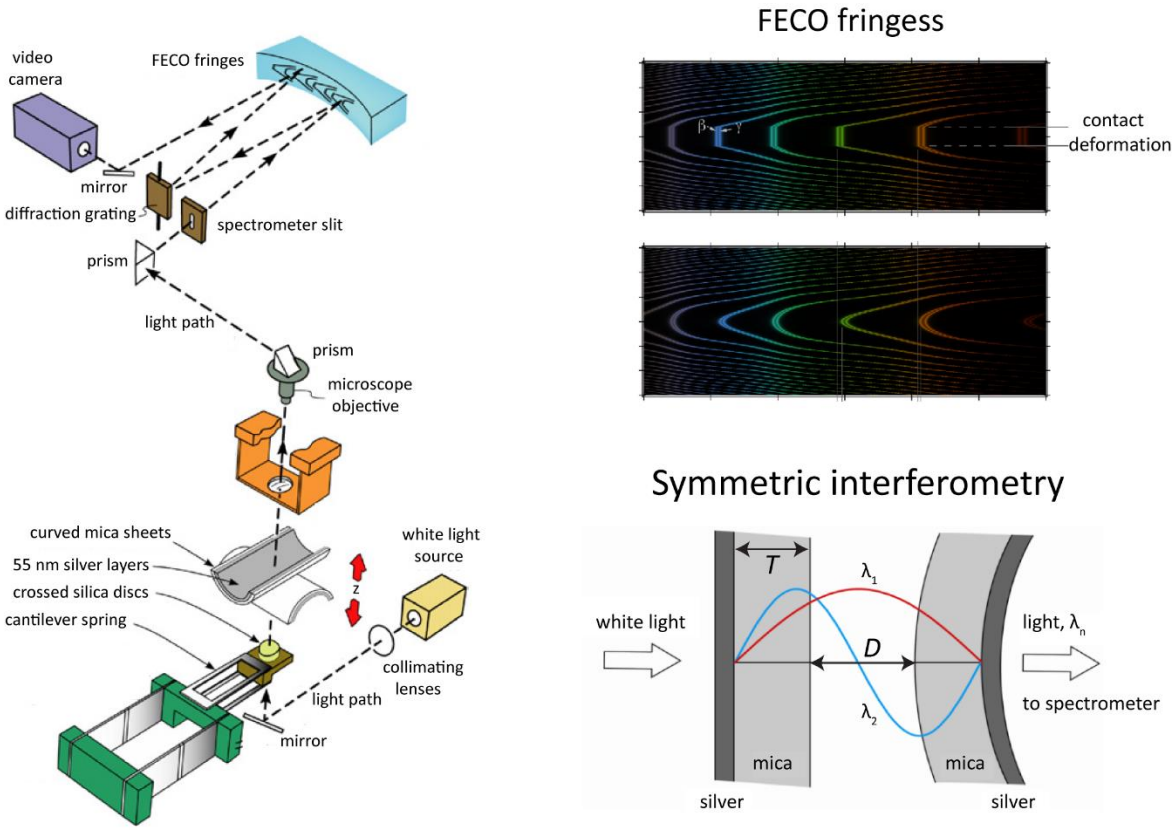

Figure 2.7. Schematic of the optical path employed in the standard SFA 2000 setup. White light is passed normal through the interface and reflects between the back-silvered mica surfaces generating interference patterns (Newton's rings) before being passed into a spectrometer, where the fringes are separated by wavelength. The wavelength of constructively interfering fringes shifts as the distance between the mirrors (surfaces) changes, and a video camera is used to record these shifts as surfaces are approached and separated during SFA experiments. Since mica is birefringent, the interference fringes exhibit an additional splitting of each fringe into thinner β and γ fringes when mica is used as the interferometer dielectric, as depicted above. However, this minimally impacts the interferometry, as either fringe wavelength (or the average of both wavelengths) can be tracked to determine separation distances. Figure adapted from Reference 33.

A major advantage of the SFA technique is that visible light interferometry is used to continuously monitor the surface separation distances to angstrom resolution and surface deformations to micrometer resolution [37]. A schematic of the standard optical setup

employed in SFA measurements is shown in Figure 2.7, along with representative interference fringes. White light sources are effective for interferometry as long as the reflective mirrors in the interferometer do not approach closer than the wavelength of the incident light, where interference is a resonant phenomenon and frequency shifts are readily resolved to fractions of the total photon wavelength. Thus, the SFA technique requires only standard white light sources and employs low energy radiation that only minimally heats the sample and surfaces, in contrast to x-rays, which routinely damage sensitive samples.

Symmetric SFA experiments, such as those described in Chapters 4–6, utilize two identical surfaces that are composed of a transparent material, typically mica. The back side of these transparent surfaces is coated with a reflective layer using standard thermal sputtering techniques, typically 55 nm of silver, which reflects approximately 98% of the incident light. The majority of the residual light is transmitted into the interface, undergoing multiple reflections before exiting the second mirror surface and entering a spectrometer.

In the spectrometer, the radiation is broken up into distinct wavelengths, called fringes of equal chromatic order (FECO), as illustrated in Figure 2.7, and the frequency of these FECO fringes is recorded with a video camera. Each successive standing wave fringe is given an increasing order, n, and the standing wave solutions for symmetric interferometers have alternating waves with nodes and anti-nodes at the center of the interface. As illustrated above, fringes of odd order (n = 1, 3, 5, …) contain anti-nodes while fringes of even order (n = 2, 4, 6, …) contain nodes. As the SFA surfaces are moved, the separation between the two mirrored surfaces changes, shifting the locations of the FECO fringes. The spectral lines from a mercury light source are concurrently guided into the spectrometer and used as a known frequency calibration to convert camera pixels to actual wavenumbers.

When two symmetric, equal thickness surfaces are in molecular contact with no intervening medium, the thickness of the surfaces, T (m), can be determined by knowing the wavelength of the nth order fringe through the relationship [37]:

$$T = \frac{n\lambda_n^0}{4\mu_{\text{mica}}} \tag{2.30}$$

Where λ_n^0 is the wavelength of the nth order fringe, and μ_{mica} is the refractive index of the mica at the wavelength of interest. To use this relationship, the order of the nth fringe is determined by [37]:

$$n = \frac{\lambda_{n-1}^0}{\lambda_{n-1}^0 - \lambda_n^0} \tag{2.31}$$

Where $\lambda_{n\text{-}1}^0$ is the wavelength of the fringe at the next highest wavelength. The locations of the FECO fringes shift as the surfaces are separated from contact, and the shift of any specific reference fringe, n, can be followed to determine the distance between the two surfaces, D (m), using the relationship [37]:

$$\tan\left(\frac{2\pi\mu D}{\lambda_n^D}\right) = \frac{2\bar{\mu}\sin[\pi(1-\lambda_n^0/\lambda_n^D)/(1-\lambda_n^0/\lambda_{n-1}^0)]}{(1+\bar{\mu}^2)\cos[\pi(1-\lambda_n^0/\lambda_n^D)/(1-\lambda_n^0/\lambda_{n-1}^0)] \pm (\bar{\mu}^2-1)} \tag{2.32}$$

Where the + sign is taken for odd fringes and the – sign is taken for even fringes and where μ is the refractive index of the intervening medium, $\bar{\mu} = \mu_{\text{mica}}/\mu$ is the effective refractive index, λ_n^D is the new wavelength of the nth (reference) fringe, λ_n^0 is the initial wavelength of the nth fringe, and $\lambda_{n\text{-}1}^0$ is the initial location of the next highest wavelength fringe.

As the separation distance becomes small, Equation 2.32 can be approximated by [37]:

$$D = nF_n(\lambda_n^D - \lambda_n^0) / 2\mu_{\text{mica}}, \quad \text{for odd n} \tag{2.33}$$

$$D = nF_n(\lambda_n^D - \lambda_n^0)\mu_{\text{mica}} / 2\mu^2, \quad \text{for even } n \tag{2.34}$$

Where F_n is a correction factor for that accounts for reflection-induced phase changes and is approximately $F_n \approx 1.024 + 1/n$ for white light reflected by the silver surfaces used in SFA measurements [37]. Notably, these equations can also be used to determine the refractive index of the intervening medium, as the odd fringe shift is independent of the medium refractive index, while the even fringe shift exhibits a refractive index dependence.

EC SFA experiments employ an asymmetric interferometer, since one of the two mica surfaces is replaced with a 42.5 nm thick gold electrode surface that functions as a SFA surface and interferometry mirror. Equation 2.32 can still be used to determine the separation distance between the surfaces, but every FECO fringe is even, preventing refractive index measurements. Two reflective gold surfaces that do not contain at least a single dielectric coating cannot be used for SFA measurements, as the separation distance between the reflective mirrors will become smaller than the wavelength of white light, resulting in complex near-field interference, as opposed to classical interferometry.

2.6 Additional experimental techniques

Throughout Chapters 3–6, additional experimental techniques were used to complement SFA measurements. In particular, AFM imaging was used in Chapter 3 to characterize the morphology and molecular smoothness of mica templated gold surfaces, NMR spectroscopy, UV-vis spectroscopy, and Raman spectroscopy was used in Chapters 3 and 4 to verify the purity of ionic liquids, dynamic light scattering measurements were used in Chapters 5 and 6 to determine the solution aggregation state of peptides, and a variety of biochemical, synthetic

and analytical chemistry techniques were used to synthesize and purify the custom ionic liquids and peptides studied in Chapters 3–6. For brevity and cohesiveness, these methods are introduced in the Materials and Methods sections of each Chapter.

2.7 References

1. Clay W. A., Dahl J.E.P., Carlson R.M.K., Melosh N. A., Shen, Z.-X. Physical properties of materials derived from diamondoid molecules. *Rep. Prog. Phys.* **78,** 016501 (2015).
2. Israelachvili, J. N. Intermolecular and Surface Forces. (Elsevier, 2011).
3. Wei W. et al. Bridging adhesion of mussel-inspired peptides: role of charge, chain length, and surface type. *Langmuir* **31,** 1105–1112 (2015).
4. Gebbie M. A. et al. Ionic liquids behave as dilute electrolyte solutions. *Proc. Natl. Acad. Sci. U. S. A.* **110,** 9674–9679 (2013).
5. Gebbie M. A., Dobbs H. A., Valtiner M., Israelachvili J. N. Long range electrostatic screening in ionic liquids. *Proc. Natl. Acad. Sci. U. S. A.* **112** (24), 7432-7437 (2015).
6. Schrödinger E. An undulatory theory of the mechanics of atoms and molecules. *Phys. Rev.* **28,** 1049–1070 (1926).
7. Leckband D., Israelachvili J. N. Intermolecular forces in biology. *Quart. Rev. Biophys.* **34** (2), 105–267 (2001).
8. Frechette J., Vanderlick Double layer forces over large potential ranges as measured in an electrochemical surface forces apparatus. *Langmuir* **17,** 7620–7627 (2001).
9. Verwey E. J. W., Overbeek J. T. G. Theory of the stability of lyophobic colloids. (1948).
10. Kornyshev A. A. Double-layer in ionic liquids: paradigm change? *J. Phys. Chem. B* **111,** 5545–5557 (2007).
11. Bazant M. Z., Kilic M. S., Storey B. D., Ajdari A. Towards an understanding of induced-

charge electrokinetics at large applied voltages in concentrated solutions. *Adv. Colloid Interface Sci.* **152,** 48–88 (2009).

12. Bazant M., Storey B., Kornyshev A. Double layer in ionic liquids: overscreening versus Crowding. *Phys. Rev. Lett.* **106,** 046102 (2011).
13. Weingärtner H. Understanding ionic liquids at the molecular level: facts, problems, and controversies. *Angew. Chem. Int. Ed.* **47,** 654–70 (2008).
14. Parsegian V. A., Gingell D. On the electrostatic interaction across a salt solution between two bodies bearing unequal charges. *Biophys. J.* **12,** 1192–204 (1972).
15. Lifshitz E. M. The theory of molecular attractive forces between solids. *J. Exp. Theor. Phys. U. S. S. R.* **29,** 94–110 (1954).
16. Levin Y. Electrostatic correlations: from plasma to biology. *Rep. Prog. Phys.* **65,** 1577–1632 (2002).
17. Wang J., Bard A. J. Direct atomic force microscopic determination of surface charge at the gold/electrolyte interface-the inadequacy of classical GCS theory in describing the double-layer charge distribution. *J. Phys. Chem. B* **105,** 5217–5222 (2001).
18. Sunner J., Nishizawa K., Kebarle P. Ion-solvent molecule interactions in the gas phase. The potassium ion and benzene. *J. Phys. Chem.* **85,** 1814–1820 (1981).
19. Burley, Petsko. Amino-aromatic interactions proteins. *FEBS Lett.* **203,** 139–143 (1986).
20. Ma J. C., Dougherty D. A. The cation − π interaction. *Chem. Rev.* **97,** 1303–1324 (1997).
21. Deakyne, Meot-Ner. Unconventional ionic hydrogen bonds. 2. NH^{+}...π. complexes of onium ions with olefins and benzene deriv. *J. Am. Chem. Soc.* **107,** 474–479 (1985).
22. Gallivan J. P., Dougherty D. A. Cation-pi interactions in structural biology. *Proc. Natl. Acad. Sci. U. S. A.* **96,** 9459–9464 (1999).

23. Crowley P. B., Golovin A. Cation-pi interactions in protein-protein interfaces. *Proteins* **59,** 231–239 (2005).
24. Khademi S. et al. Mechanism of ammonia transport by Amt/MEP/Rh: structure of AmtB at 1.35 A. *Science* **305,** 1587–1594 (2004).
25. Horn R. G., Israelachvili J. N. Direct measurement of structural forces between two surfaces in a nonpolar liquid. *J. Chem. Phys.* **75,** 1400 (1981).
26. Christenson H. K. Experimental measurements of solvation forces in nonpolar liquids. *J. Chem. Phys.* **78,** 6906–6913 (1983).
27. Israelachvili J. N., Pashley R. M. Molecular layering of water at surfaces and origin of repulsive hydration forces. *Nature* **306,** 249–250 (1983).
28. Pauling L. The Structure and entropy of ice and of other crystals with some randomness of atomic arrangement. *J. Am. Chem. Soc.* **57,** 2680–2684 (1935).
29. Israelachvili J., Wennerström H. Role of hydration and water structure in biological and colloidal interactions. *Nature* **379,** 219–225 (1996).
30. Chandler D. Interfaces and the driving force of hydrophobic assembly. *Nature* **437,** 640–647 (2005).
31. Israelachvili J., Pashley R. The hydrophobic interaction is long range, decaying exponentially with distance. *Nature* **300,** 341–342 (1982).
32. Donaldson S. H. et al. Developing a general interaction potential for hydrophobic and hydrophilic interactions. *Langmuir* **31** (7), 2051-2064 (2015).
33. Israelachvili J. et al. Recent advances in the surface forces apparatus (SFA) technique. *Rep. Prog. Phys.* **73,** 036601 (2010).
34. Israelachvili J., Tabor D. The measurement of van der Waals dispersion forces in the range

1.5 to 130 nm. *Proc. R. Soc. Lond. A. Math. Phys. Sci.* **331,** 19–38 (1972).

35. Leckband D. E., Israelachvili J. N., Schmitt F. J., Knoll W. Long-range attraction and molecular rearrangements in receptor-ligand interactions. *Science* **255,** 1419–21 (1992).
36. Alcantar N. A., Park C., Pan J. M., Israelachvili J. N. Adhesion and coalescence of ductile metal surfaces and nanoparticles. *Acta Mater.* **51,** 31–47 (2003).
37. Israelachvili J. N. Thin film studies using multiple-beam interferometry. *J. Colloid Interface Sci.* **44,** 259–272 (1973).
38. Vinogradova O. I. Drainage of a thin liquid film confined between hydrophobic surfaces. *Langmuir* **11,** 2213–2220 (1995).
39. Israelachvili J. N. et al. The intersection of interfacial forces and electrochemical reactions. *J. Phys. Chem. B* **117,** 16369–16387 (2013).
40. Hillier A. C., Kim S., Bard A. J. Measurement of double-layer forces at the electrode / electrolyte interface using the atomic force microscope : potential and anion dependent interactions. *J. Phys. Chem.* **100,** 18808–18817 (1996).
41. Valtiner M., Kristiansen K., Greene G. W., Israelachvili J. N. Effect of surface roughness and electrostatic surface potentials on forces between dissimilar surfaces in aqueous solution. *Adv. Mater.* **23,** 2294–9 (2011).

3 Ionic liquids behave as dilute electrolyte solutions

Gebbie M. A., Valtiner M., Banquy, X, Fox E. T., Henderson W. A., Isrealachvili J. N. *Proc. Natl Acad. Sci. USA* **110** (24), 9674–9679 (2013).

3.1 Abstract

We combine direct surface force measurements with thermodynamic arguments to demonstrate that pure ionic liquids are expected to behave as dilute weak electrolyte solutions, with typical effective dissociated ion concentrations of less than 0.1% at room temperature. We performed equilibrium force-distance measurements across the common ionic liquid [C_4mim][NTf_2] using a surface forces apparatus with *in situ* electrochemical control and quantitatively modeled these measurements using the van der Waals and electrostatic double-layer forces of the Derjaguin-Landau-Verwey-Overbeek (DLVO) theory with an additive repulsive steric (entropic) ion-surface binding force. Our results indicate that ionic liquids screen charged surfaces through the formation of both bound (Stern) and diffuse electric double-layers, where the diffuse double-layer is comprised of effectively dissociated ionic liquid ions. Additionally, we employed the energetics of thermally dissociating ions in a dielectric medium to quantitatively predict the equilibrium for the effective dissociation reaction of [C_4mim][NTf_2] ions, in excellent agreement with the measured Debye length. Our results clearly demonstrate that, outside of the bound double-layer, most of the ions in [C_4mim][NTf_2] are not effectively dissociated and thus do not contribute to electrostatic screening. We also provide a general, molecular-scale framework for designing ionic liquids with significantly increased dissociated charge densities via judiciously balancing ion pair interactions with bulk dielectric properties. Our results clear up several inconsistencies that

have hampered scientific progress in this important area and guide the rational design of novel, high free ion density ionic liquids and ionic liquid blends.

3.2 Introduction

Ionic liquids are fluids composed solely of ions [1, 2]. Much of the recent scientific interest surrounding ionic liquids derives from the fact that ionic liquids have been demonstrated for numerous applications, such as safe, high-efficiency electrochemical storage devices [3, 4], self-assembly media [5], and lubrication [6]. A key paradigm within ionic liquids research is that the physical properties of ionic liquids can be controlled to an unprecedented degree through the judicious design of cation-anion pairs [1–9]. Thus, ionic liquids are known as "designer" solvents/materials [1]. However, fully realizing this advantage requires the development of a comprehensive framework that can be used to rationalize the relationship between an ionic liquid's molecular structure and its bulk and interfacial behavior and properties, which are governed by a complex interplay of Coulomb, van der Waals, dipole, hydrogen bonding, and steric interactions [10, 11].

Recent work has greatly progressed a fundamental understanding of ionic liquids at charged interfaces, but there are currently inconsistencies between experiment and theory [7-9, 12–23]; this is particularly true for the ranges of surface-induced ordering and electrostatic screening. For example, a comparison of the values obtained from ionic conductivity and ion diffusion coefficient measurements with ionic liquid electrolytes lead to the postulation that ionic liquids behave as highly-dissociated electrolytes with an immense concentration of free ions in solution, where typical ionic liquids are expected to exhibit effective free ion concentrations on the order of 50–80% of the maximum ion density [24, 25]. With such high effective free ion concentrations, the Debye lengths for typical ionic liquids, κ^{-1}, should be on

the order of 0.1 Å [4, 9], which is at least 1–2 orders of magnitude smaller than the molecular dimensions of even the smallest ionic liquids. This discrepancy is typically provided as evidence that ionic liquids should completely electrostatically screen charged surfaces within several bound (Stern) ion layers (1–2 nm), beyond which charged surfaces no longer impact ion density or ordering [9, 21–23]. This screening behavior has been observed in theoretical studies involving simplified model ionic liquids [9, 21–23].

In contrast, X-ray reflectivity, atomic force microscopy (AFM), and surface forces apparatus (SFA) measurements have shown that strong ion-surface interactions can induce ion ordering that extends up to 10 nm into solution (per surface) [12–20]. Notably, the sign and magnitude of the charge density intrinsic to solid surfaces are crucial determinants for the ranges of the surface-induced ordering and for the templating of the specific structure formed by the bound ion layers [19, 20]. For example, a combined X-ray reflectivity-molecular dynamics study on ionic liquid-solid interfaces demonstrates that replacing a neutral graphene surface with a negatively-charged muscovite mica surface leads to a substantial increase in the range of surface-induced ion ordering and changes the structure of the bound ion layers from a mixed cation-anion layering motif to an alternating cation-anion layering structure [20].

Further, a study of the differential capacitance of ionic liquids at electrode surfaces indicates that ionic liquids electrostatically screen charged surfaces through the formation of electric double-layers consisting of distinct inner (bound/compact) and outer (diffuse) double-layers [26]. This screening mechanism is consistent with proposed models, analogous to the Gouy-Chapman-Stern model for dilute electrolyte solutions [27, 28]. Nevertheless, the

prevailing picture is that ionic liquids should behave as highly-concentrated, but largely dissociated, electrolyte solutions.

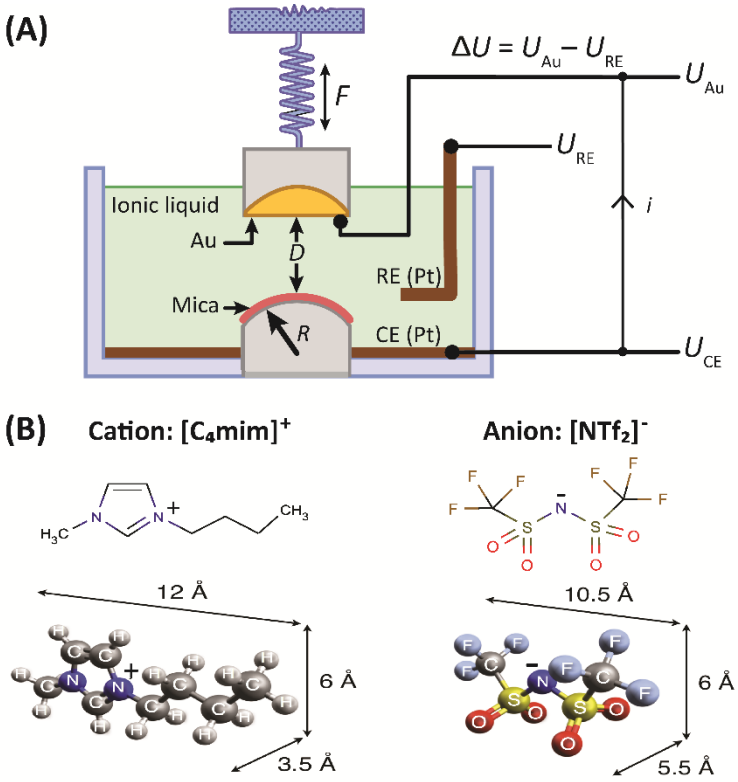

Figure 3.1. (A) Schematic of the electrochemical surface forces apparatus (EC SFA). The electrochemical potential of the top gold electrode surface was controlled through a custom built electrochemical SFA attachment based on a three electrode setup [32, 43]. When immersed in $[C_4mim][NTf_2]$, muscovite mica is known to acquire a negative surface charge through the dissociation of surface-bound K^+ ions; the resultant K^+ concentration within the bulk ionic liquid is negligible [17, 20]. The mica surface potential, Ψ_M, was assumed to be independent of applied potentials, ΔU. The distance between the two surfaces, D, was defined with respect to the contact of the gold and mica surfaces in absence of $[C_4mim][NTf_2]$, where $D = 0$. Equilibrium (static) force measurements were performed at constant applied potentials, ΔU, and the open circuit potential (OCP), where the potential was sensed to be -140 mV. Degradation peaks in post-experimental cyclic voltammetry measurements were used to account for small shifts in potential referencing across experiments. All results described here were measured at applied potentials, ΔU, that did not induce Faradaic reactions at the gold electrode surface. (B) Molecular structure and dimensions of the 1-butyl-3-methylimidazolium bis(trifluoromethanesulfonyl)imide

([C_4mim][NTF_2]) cation and anion. Conformations and dimensions were calculated through the conjugate gradient energy minimization of the chemical structures using the Universal Force Field [44].

Here, we report quantitative equilibrium force-distance measurements of two dissimilarly-charged surfaces: single-crystalline muscovite mica and molecularly-smooth, polycrystalline gold (0.2 nm RMS roughness), interacting across an ionic liquid – [C_4mim][NTf_2] (Fig. 3.1B) - using the EC (electrochemical) SFA technique described in Fig. 3.1A. These results were quantitatively modeled using the van der Waals and electrostatic double-layer forces of the Derjaguin-Landau-Verwey-Overbeek (DLVO) theory with an additive monotonic repulsive steric (entropic) ion-surface binding force. Additionally, we propose a general, molecular-scale framework that can be used to predict the temperature-dependent effective free ion density for ionic liquids, provided that the ion dissociation energy (interaction potential) in vacuum, E_d, and the low-frequency relative permittivity, ε, of an ionic liquid can be independently determined.

Our results further show that the relative charges and potentials of confining surfaces, as well as the chemical nature of each of the two ion species in single-component ionic liquids, can impact the qualitative nature of surface-surface interactions across nano-confined ionic liquids by resulting in the presence (or absence) of long range electrostatic interactions. These results provide insights into current inconsistencies regarding the ranges of electrostatic screening and surface-induced ordering in ionic liquids, and thus have important implications for the utilization of ionic liquids in numerous applications, including as electrolytes in electrochemical storage devices, self-assembly media, and lubricants.

3.3 Results and analysis

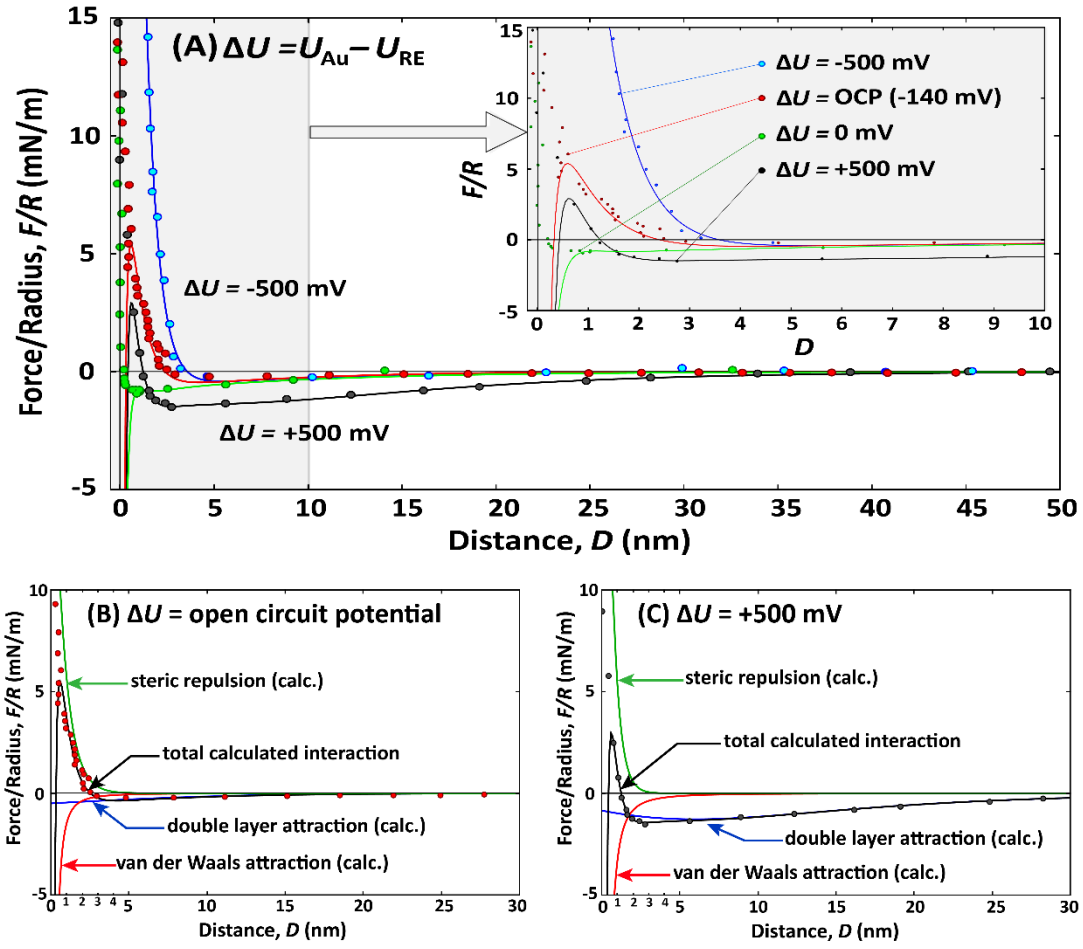

Figure 3.2. Points correspond to experimental data and solid lines correspond to forces calculated using Equation 1. (A) Representative equilibrium force-distance, *F(D)*, profiles measured between mica and gold on approach. Measurements were taken while monitoring the open circuit potential (OCP) (red) and at 3 different applied potentials, ΔU, across the ionic liquid [C_4mim][NTF_2]. The inset shows the same data for distances of D < 10 nm. (B),(C) Distance dependence of the individual and total total calculated interaction potentials for (B) ΔU = OCP and (C) ΔU = +500 mV.

3.3.1 Equilibrium force-distance measurements

Representative force-distance profiles, $F(D)$, for the open circuit potential (OCP, the potential was sensed) and applied potentials of ΔU = -500, 0 and +500 mV are shown in Fig. 3.2. For the measurements that were performed at constant ΔU, the system was allowed to equilibrate for at least 5 min at each potential before beginning the equilibrium $F(D)$ measurements. Immediately, after applying each potential, the magnitudes of the current densities measured at the gold electrode were found to decay to a negligible baseline current density within several seconds (on the order of ~ 10–50 nA/cm^2), consistent with the charging of an electric double-layer – no Faradaic currents were observed.

Static (equilibrium) $F(D)$ measurements were taken by using a piezoelectric crystal to move the gold surface in constant voltage steps of ~ 1.5–3.0 V, which corresponds to constant distance, D, steps of between 3–5 nm. The surfaces were allowed to equilibrate at each point for 45 s before moving to the next D. The voltage-distance calibration for the piezoelectric crystal was determined at surface separation distances, D, where no interaction forces were measured. This procedure allowed us to determine the equilibrium interaction forces across the surfaces at each measured D, and the experimental error of the measured data points are $F = \pm 0.01$ mN/m and $D = \pm 0.2$ nm.

3.3.2 Total interaction potential

The measured force-distance profiles exhibit a long range interaction regime – D out to 35 nm – that is solely attributable to electrostatic forces. The forces measured in this regime asymptotically decay with an exponential decay length of 11 ± 2 nm, and are well-fitted by equations describing overlapping diffuse electric double-layers. For surface separations $D <$ 3 nm, short range forces, arising from a nontrivial interplay of van der Waals forces, ion-

surface binding forces, and forces induced by ion structuring begin to dominate the force profiles. Solid lines overlaying the experimental points in Fig. 3.2 were fitted using Equations 3.1–3.4.

$$\frac{F}{R} = -\frac{A_H}{6D^2} + \frac{8\pi nkT}{\kappa}\frac{y_M s_{Au} - 0.5(y_M^2 - s_{Au}^2)\exp(-\kappa D)}{\exp(\kappa D) + \exp(-\kappa D)} + 2\pi W_0 \exp(-\frac{D}{\lambda_0}) \qquad (3.1)$$

$$\kappa^2 \equiv \frac{2ne^2}{\varepsilon\varepsilon_0 kT} \qquad (3.2)$$

$$y_M = \frac{e\Psi_M}{kT} \qquad (3.3)$$

$$s_{Au} = \frac{e\sigma_{Au}}{\kappa\varepsilon\varepsilon_0 kT} \qquad (3.4)$$

Where A_H (J) is the Hamaker constant, D (m) is the surface separation, ε (11.6) is the relative permittivity of $[C_4mim][NTf_2]$ [4], κ^{-1} (m) is the Debye screening length, Ψ_M (V) is the Outer Helmholtz Plane (OHP) mica potential, σ_{Au} (C/m^2) is the OHP gold charge density, λ_0 (m) is a steric decay length, W_0 (J/m^2) is a fitted steric prefactor, T (295 K) is the temperature, e (C) is the elementary charge, n (m^{-3}) is the number density of dissociated ions, k (J/K) is Boltzmann's constant, and ε_0 (F/m) is the permittivity of free space. The parameter values can be found in Tables 3.1 and 3.2.

Equation 3.1 represents a "DLVO-type" interaction potential, where the first term is the mica-gold van der Waals interaction, the second is a linearized Poisson-Boltzmann equation for overlapping electric double-layers [29, 30], and the third is an empirical steric repulsion potential arising from surface-bound ions.

3.3.3 van der Waals forces

Thin films of strongly adsorbed molecules can cause Hamaker constants, A_H, to vary with surface separation distance, D [36, 48]. In this system, when $D >>$ than the thickness of any adsorbed films ($D > 5$ nm), the bulk dielectric properties of the gold and mica surfaces can be inserted into the Lifshitz theory to calculate A_H. However, as D progressively approaches the combined thickness of the adsorbed ion films, the effective Hamaker constant can be significantly impacted by the adsorbed ion films. Thus, the properties of the thin films must be explicitly considered to carry out an *ab initio* calculation of the effective A_H for each D [36, 48]. In the distance regime of relevance for this work ($D < 5$ nm), the ionic liquid ions are observed to screen the mica-gold van der Waals attraction by about 40% compared to the value of A_H calculated via the Lifshitz theory for the mica-gold van der Waals interaction in a solvent of $\varepsilon = 11.6$.

3.3.4 Diffuse double-layer forces

The form of the linearized Poisson-Boltzmann (PB) equation used in Equation 3.1 is for mixed constant charge (gold) – constant potential (mica) (PC) boundary conditions (29). PC boundary conditions were found to be consistent with the experimental data. Neither both surfaces constant charge (CC) nor both surfaces constant potential (PP) were found to agree with the experimental data [29, 30].

The linearized PB equation is only quantitatively exact for low surface potentials ($\Psi < 25$ mV). However, the errors introduced by this linearized approach are typically not excessive for potentials as high as 200 mV, except for distances that are significantly shorter than one Debye length [30]. Since the highest surface potential fitted for this system, ~ -200 mV for the mica surface (Table 3.1) is in excess of 25 mV, the fitted values of the surface charges and

potentials should be taken as approximate values that highlight the following general effect: ionic liquids form diffuse electric double-layers to screen surface charges/potentials that extend beyond strongly-bound ion layers. The full, nonlinear PB equation will have the same exponential form (same decay behavior), but a different pre-factor. Solving this equation would yield more exact values of the surface charges and potentials.

The mica Outer Helmholtz Plane (OHP) potential (~ -200 mV) was independently determined by fitting the $F(D)$ profiles for ΔU = OCP and -500 mV, where the gold surface was fully screened by the bound $[C_4mim][NTf_2]$ ions. An OHP potential of ~ -200 mV corresponds to a mica surface charge density of approximately 10% of the maximum mica charge density that can result from the thermal dissociation of the surface-bound K^+ ions that are present at the surface of muscovite mica - as calculated through the Grahame equation (linear approximation) [45]. This mica surface potential was then taken as a constant for the $F(D)$ profiles where the gold surface was not fully screened within the bound ion layer ($\Delta U >$ OCP). The mica surface was observed to exhibit behavior closer to constant potential than constant charge, and any changes observed in the measured long range portion of the force-distance profiles upon the application of electrochemical potentials, ΔU, were assumed to result from changes in the OHP charge density at the gold surface.

The CC boundary conditions were determined to be inconsistent with our data because the $F(D)$ profiles measured for ΔU = OCP and -500 mV exhibit weak long range attractions. These are the potentials where the ionic liquid ions fully screen the gold surface ($\sigma_{Au} = 0$ mC/m^2). When the mica surface is taken to behave as constant charge, the calculated electrostatic interactions always exhibit a weak long range repulsion [29]. When the mica surface was instead taken to behave as constant potential, then the calculated electrostatic

interactions exhibit a weak long range attraction consistent with the experimental data. Therefore, the mica surface behaves as a constant potential surface.

The PP boundary conditions were determined to be inconsistent with our data because the range and magnitude of the experimentally measured F(D) profiles are qualitatively different than the F(D) profiles calculated with PP boundary conditions: for PP boundary conditions under the case of positive gold charging, the range and magnitude of the electrostatic attraction would be expected to be much larger and exhibit a qualitatively different distance dependence, with no gradual slowing of the rate of change of the attraction as the surface separation distance approaches 0 nm [29]. Therefore, the gold surface behaves as a constant charge surface.

For dissimilar surfaces, the electric double-layer interactions can be attractive for all separations, repulsive for all separations, or change sign from attractive to repulsive (or vice versa) at finite distances. Figs. 3.2B and 3.2C show the relative magnitude and distance dependence of each of the three calculated force contributions, as well as the total calculated force-distance potential (the contributions are additive) for ΔU = +500 mV and OCP. Importantly, while the electrochemical potential that is applied to the gold surface, ΔU, ultimately determines the OHP charge density of the isolated gold surface, σ_{Au}, there is no equation that directly relates the two values; the value of σ_{Au} must be determined by fitting the measured force-distance profiles.

Table 3.1. Measured, calculated and fitted parameters using Equations 3.1–3.4.

Equation Parameters	**Δ*U*, -500 mV**	**OCP**	**Δ*U*, 0 mV**	**Δ*U*, +500 mV**
Gold charge, σ_{Au}	0 ± 0.1 mC/m^2	0 ± 0.1 mC/m^2	0.4 ± 0.1 mC/m^2	3.6 ± 0.1 mC/m^2
Mica potential, Ψ_M	-198 ± 8 mV	-191 ± 8 mV	-196 ± 8 mV	-193 ± 5 mV
Debye length κ^{-1}	13 ± 2 nm	12 ± 2 nm	12 ± 2 nm	10 ± 2 nm
Dissoc. ion conc., C_i	0.8 ± 0.3 × 10^{-4} M	0.9 ± 0.3 × 10^{-4} M	0.9 ± 0.3 × 10^{-4} M	1.4 ± 0.3 × 10^{-4} M

Table 3.2. Calculated, and fitted parameters using in Equations 3.1–3.4.

Equation Parameters	**Δ*U*, -500 mV**	**OCP**	**Δ*U*, 0 mv**	**Δ*U*, +500 mV**
Gold charge, s_{Au}	0 ± 0.3	0 ± 0.2	1.7 ± 0.5	13 ± 0.3
Mica potential, y_M	-7.8 ± 0.3	-7.5 ± 0.3	-7.7 ± 0.3	-7.8 ± 0.2
Hamaker constant, A_H	9 ± 6 ×10^{-21} J	9 ± 3 × 10^{-21} J	9 ± 2 × 10^{-21} J	2 ± 0.2 × 10^{-20} J
Steric prefactor, W_0	23 ± 2 mJ/m^2	3.7 ± 0.4 mJ/m^2	1.6 ± 0.2 mJ/m^2	7.9 ± 0.5 mJ/m^2
Steric decay length, λ_0	0.65 ± 0.05 nm	0.70 ± 0.05 nm	0.50 ± 0.02 nm	0.45 ± 0.03 nm
OHP shift	3 nm	0 nm	0 nm	0 nm

The long range interaction forces are well-fitted by a Debye screening length of κ^{-1} = 11 ± 2 nm for all applied potentials, which agrees with the asymptotic form of Equation 3.1 that decays as $\exp(-\kappa D)$, where κ^{-1} is the Debye length. This long range effect indicates that the surface-bound ions (i.e., the ions within the Inner Helmholtz Plane IHP) or Stern layer) are not able to fully screen the charged surface. The level of agreement between Equation 3.1 and the measured force-distance profiles (Fig. 3.2) indicates that the residual potential propagating past the bound ion layers (two charged surfaces) is screened by an exponentially-decaying diffuse electric double-layer -type mechanism (Fig. 3.3). Since ionic liquids are solvent-free, the diffuse double-layer must consist of an effectively neutral, coordinated cation-anion network (i.e., like "solvent molecules") that exists in equilibrium with a small fraction of effectively dissociated ions (Fig. 3.3) - analogous to the double-layer electrode screening found for dilute solvent-salt mixtures [31, 32], where the plane of origin for this electrostatic interaction is the OHP. For $[C_4mim][NTf_2]$, the OHP is shifted out from the surfaces by between 0 ± 0.1 nm (OCP, ΔU = 0 and +500 mV) and 1.5 ± 0.1 nm (ΔU = -500 mV) per surface, depending on the relative surface potentials.

Strikingly, the long range portions of the measured equilibrium force-distance profiles for applied potentials, ΔU, that are more positive than the OCP are fundamentally different than the profiles measured for applied potentials that are more negative than the OCP (Fig. 2). For ΔU > OCP, the force profiles exhibit a long range attraction that is consistent with a positive OHP charge at the gold surface and a negative OHP potential at the mica surface. Therefore, the bound ion layers formed at both the mica and gold surfaces do not fully electrostatically screen the surfaces.

For $\Delta U \leq$ OCP, the force profiles exhibit a weaker long range attraction, whereas an electrostatic repulsion would be expected for the case of negative gold charging. Shifting the OHP out by 3 nm for ΔU = -500 mV, hence accounting for the fact that a thicker layer of bound ions is required to screen the increasingly-negative gold surface charge density, brings the range and magnitude of this electrostatic attraction into quantitative agreement with the ΔU = OCP (Fig. 2): both force-distance profiles exhibit $\kappa^{-1} = 12 \pm 2$ nm, $\Psi_M \sim$ -195 mV, and $\sigma_{Au} = 0 \pm 0.1$ C/m^2. Thus, the bound ion layer at the gold surface fully screens the electrode for ΔU = OCP and -500 mV, while the bound ion layer at the mica, again, does not fully screen the surface.

From these results, we discern that bound ion layers enriched in $[C_4mim]^+$ cations electrostatically screen polycrystalline gold surfaces more effectively than bound ion layers enriched in $[NTf_2]^-$ anions. This contrast in screening efficiency likely arises from the substantial differences between the molecular structures of the $[C_4mim]^+$ and $[NTf_2]^-$ ions: $[C_4mim]^+$ cations are largely planar, contain well-defined polar and non-polar regions, and exhibit a lower degree of conformational flexibility as compared to the bulkier $[NTf_2]^-$ anions (Fig. 3.1B). These observations are consistent with studies of ionic liquids at the free vacuum interface, where the size, polarity, and shape asymmetry of ionic liquid cations and anions are shown to differently impact their structuring at the free vacuum interface, with ionic liquids forming increasingly charge-separated electric double-layers at the ionic liquid-vacuum interface as the degree of cation-anion asymmetry is increased [33, 34].

3.3.5 Steric ion binding forces

The short range portions (D < 3 nm) of the force-distance profiles are fitted by the superposition of a mica-gold van der Waals attraction and a monotonic steric "hydration-type"

repulsion (decay length = 0.6 ± 0.15 nm) corresponding to a characteristic length of the adsorbed ions (Fig. 3.1B). The superposition of these two short range force contributions qualitatively captures the transition from the force regimes where the long range diffuse double-layer forces are the sole contributor to the measured force-distance profiles, to the regimes where the force profiles are dominated by short range, specific ion-ion and ion-surface interactions. This empirical monotonic repulsion is, however, unable to fully describe the complex, non-monotonic features of the short range portions of the measured force-distance profiles. In particular, the force-distance profiles measured at the OCP (Fig. 3.2) exhibit non-monotonic behavior that is indicative of complex ion ordering. As a result, the agreement between the measured and theoretically modeled forces progressively diverges as the surface-surface separation distance, D, decreases from D = 1 to D = 0 nm. The physical origins of the forces measured in the short range portions of the profiles are extremely complex since continuum theories of colloidal interactions no longer apply.

3.3.6 Thermodynamic model for effective free ion concentration

Our results indicate that the general electrostatic screening behavior of [C_4mim][NTf_2] (long range) is consistent with a diffuse electric double-layer mechanism when the Stern layers, "solvent molecules" and dissociated ions (Fig. 3.3) are properly defined. Remarkably, the 11 ± 2 nm Debye length, κ^{-1}, for this system indicates that the concentration of freely dissociated ions in [C_4mim][NTf_2] at 295 K is $C_i = 1.1 \pm 0.5 \times 10^{-4}$ M (mol/L), corresponding to 0.003% dissociation. Therefore, the dissociation constant is $K_d = 7.3 \pm 0.7 \times 10^{-10}$ (pK_d = 9.14).

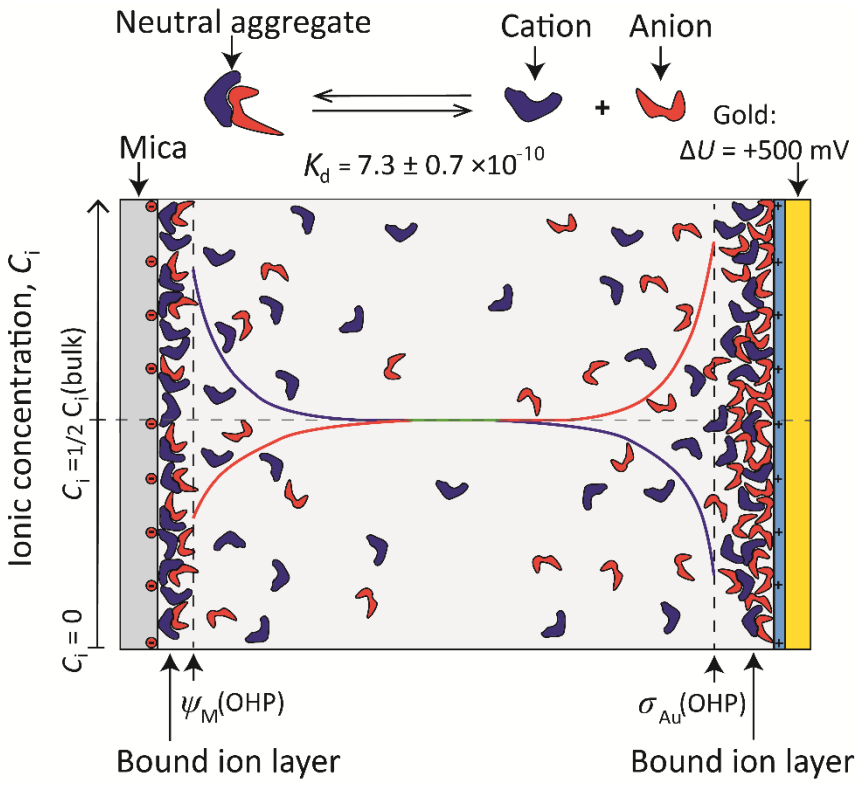

Figure 3.3. Diagram of the diffuse electric double-layers formed by [C_4mim][NTf_2] ions for ΔU = +500 mV. Analogous electric double-layers are formed for all other potentials. Effectively dissociated pairs of ions are generated via the equilibrium dissociation reaction above. Light grey shading in the interface outside the Outer Helmholtz Plane (OHP) represents a dielectric fluid consisting of an effectively neutral cation-anion network. Lines overlaying the diagram indicate the relative concentration gradient of dissociated ions: blue represents cations, red anions, and green: C_{cation} = C_{anion} = 1/2 $C_{i,bulk}$. The bound and diffuse electric double-layers are enriched in cations (blue) at the negative mica surface and anions (red) at the positive gold surface.

The value for K_d appears to be explicable in terms of the energetics of thermally dissociable ions interacting in a dielectric medium, providing further evidence for electric double-layer formation by ion dissociation: as a first approximation, the equilibrium mole *fraction* (solubility) of dissociated (uncoordinated) pairs of ions (for electroneutrality) in a dielectric medium of associated (electrically neutral) [C_4mim][NTf_2] ions, X_d, can be calculated from the Boltzmann distribution:

$$X_d = \exp[-\frac{\Delta\mu^i}{kT}] \cong \exp[-\frac{E_d}{\varepsilon kT}] \quad (3.5)$$

where $\Delta\mu^i$ (J) is the chemical potential change for ions going from the associated to dissociated state in a dielectric medium, E_d (J) is the ion dissociation energy (interaction potential) in vacuum, k (J/K) is Boltzmann's constant, T (295 K) is the temperature, and ε (11.6) is the relative permittivity of $[C_4mim][NTf_2]$ [4]. While Equation 3.5 only accounts for low-frequency dielectric screening of the interaction potential, Coulombic interactions typically account for greater than 90% of the total interaction energy between ionic liquid ions [7, 35]. Electronic structure calculations show that E_d = 315.26 kJ/mol (128.50 k_BT per pair of ions) for $[C_4mim][NTf_2]$ [35], and this value yields a dissociated ion concentration of $C_i = 1.2 \times 10^{-4}$ M (mol/L), agreeing with the experimental results to within 10%.

3.4 Discussion

While our results may, at first glance, appear to stand in contradiction to previous SFA and AFM studies on ionic liquids which found only short range structural forces [13–19], we discuss why our higher resolution results are not only consistent with the existing scientific literature, but also provide insights into the apparent discrepancies that exist regarding the ranges of electrostatic screening and surface-induced molecular ordering in ionic liquids.

Notably, results from AFM measurements with *in situ* electrochemical control of substrate surfaces indicate that the near surface structuring of the ionic liquid ions depends on the magnitude and sign of the applied electrochemical potentials [19]. The authors of this study concluded that electrode surface potentials are entirely screened by adsorbed ion layers, and ruled out screening by a diffuse electric double-layer [19]. However, the forces arising from the overlap of two diffuse electric double-layers scales as the radius of the AFM tip ($R \sim 10^{-9}$

m) for the sphere-on-flat geometry employed in AFM studies. The crossed-cylinder geometry used in the SFA leads to the same local sphere-on-flat scaling for the measured forces, where the radius of the sphere, *R*, is equal to the geometric mean of the curvature of the cylinders ($R \sim 10^{-2}$ m). As a result, the magnitude of the diffuse double-layer forces that we measured in this series of experiments, which are on the order of 10^{-5} N after accounting for the radius normalization (well within the experimental accuracy of the SFA technique), would correspond to a force of 10^{-12} N for a nano-scale AFM tip, which is 3 orders of magnitude lower than the 10^{-9} N sensitivity reported for current AFM studies on ionic liquids [18, 19].

Additionally, previous SFA studies on ionic liquids utilized symmetric ceramic surfaces to explore the electric double-layers formed by ionic liquids [13–17]. The force profiles that have been consistently measured across ionic liquids between symmetric interfaces are repulsive and oscillatory in nature [13–17]. The measurement of oscillatory force-distance profiles across fluids arises from to the presence of layered, phase separated regions within confined fluid films [36–38]. However, short range oscillatory forces, when present, are typically only one contribution to the forces that are measured across confined liquid films [36, 37]. For example, in SFA measurements of two symmetric mica surfaces interacting across a 1.0×10^{-3} M aqueous KCl solution, oscillatory forces were shown to be superimposed on a steep, short range monotonic double-layer and/or hydration repulsion at surface-surface separation distances, *D*, of less than 2 nm [36]. The oscillatory force profiles measured across ionic liquids also appear to be superimposed on monotonically-increasing *repulsions* that are consistent, in both range and magnitude, with the electric double-layer forces measured in the current study [13–17].

In our system, we expect the isolated single-crystalline mica surfaces to induce alternating cation-anion layering motifs that extend into the $[C_4mim][NTf_2]$, as has been observed previously [17, 20]. However, the ion structures templated by the polycrystalline gold surfaces will necessarily be more disordered than the structures induced by single-crystalline mica surfaces. Since the presence of even a sub-nm scale surface roughness can be sufficient to smear out the discrete oscillatory character of force-distance profiles [36, 39], we infer that the polycrystalline nature of the gold surfaces used in our experiments is responsible for the suppression of pronounced discrete oscillatory instabilities. Nevertheless, the trends in the short range repulsions that arise from the overlap of the strongly bound ion layers is consistent with previous work on ionic liquids and dilute electrolyte solutions [13–17, 31, 32, 36].

We do, however, note that the room temperature effective dissociated ion concentration on the order of 50–80% of the total ionic density that has been postulated by comparing ionic conductivity to diffusivity measurements for ionic liquids (i.e., the 'ionicity' approach) [24, 25] stands in stark contrast to the freely dissociated ion concentration of 0.003% calculated from our equilibrium force measurements. However, conductivity and diffusivity measurements inherently include kinetic (dynamic transport) effects, and thus are not directly related to the equilibrium association and dissociation of pairs of ions [40]. Furthermore, the 'ionicity' approach to predicting the effective concentration of dissociated ions in ionic liquids [24, 25] never explicitly considers the energetics of dissociating ionic liquid ions. Therefore, while the 'ionicity' approach has great utility with regards to studying the dynamic properties of ionic liquids, we reason that these ratios do not appear to be directly proportional to the equilibrium effective ionic concentration that contributes to electrostatic screening in ionic liquids.

3.5 Summary and conclusions

In conclusion, our results show that the ionic liquid $[C_4mim][NTf_2]$ screens charged surfaces through the formation of both bound (Stern) and diffuse electric double-layers, where the diffuse double-layer is composed of effectively dissociated $[C_4mim]^+$ and $[NTf_2]^-$ ions. Additionally, we employed the energetics of thermally dissociating ions in a dielectric medium to quantitatively predict the equilibrium for the effective dissociation reaction of $[C_4mim][NTf_2]$ ions, in excellent agreement with the measured value (Debye length). The theories that we have used during our analysis are general, thermodynamically-rigorous theories, thus we expect these observations to be widely applicable to other ionic liquids. We therefore deduce that each combination of ionic liquid ions should have a unique, temperature-dependent dissociation constant, K_d, that can be used as a design parameter to help rationalize and tune both the bulk and interfacial interactions of the liquid. We also suggest that K_d can be calculated with reasonable accuracy by independently knowing ε and E_d for each pair of ions, which makes comparing the effective dissociated ion concentration and electrostatic screening lengths for a wide range of ionic liquids a straightforward task.

3.6 Materials and methods

The ionic liquid 1-butyl-3-methylimidazolium bis(trifluoromethanesulfonyl)imide ($[C_4mim][NTf_2]$) was synthesized, purified, dried and characterized using a previously established procedure for the preparation of electrochemical-grade ionic liquids [41]. The $[C_4mim][NTf_2]$ was clear and colorless, and NMR and UV-Vis spectroscopy were used to establish that the $[C_4mim][NTf_2]$ was of electrochemical-grade purity. Raman spectroscopy found that the ionic liquid has a negligible fluorescence background, further confirming its purity, as ionic liquid impurities are often strongly fluorescent. After synthesis and drying,

Karl Fischer titration was utilized to determine that the (trace) water content of the $[C_4mim][NTf_2]$ was 7 ppm. The $[C_4mim][NTf_2]$ was stored under vacuum until use in the EC SFA experiments.

Before each EC SFA experiment, the $[C_4mim][NTf_2]$ was dried a second time by heating in a vacuum oven under vacuum at 373 K for at least 48 h. Following drying, the ionic liquid was immediately injected into a gas-tight SFA through an injection port under dry nitrogen purge conditions - the nitrogen pressure flowing through the SFA was higher than ambient pressures. After injection, the SFA was resealed, and all experiments were performed in the presence of a reservoir of the desiccant phosphorus pentoxide (P_2O_5) that was placed in the SFA chamber. Each experiment lasted between 12 and 36 h, and the P_2O_5 that was removed from the box was unsaturated at the conclusion of each experiment. Additionally, post-experimental cyclic voltammetry measurements showed that the $[C_4mim][NTf_2]$ exhibited an electrochemical window in excess of 4 V, and previous work has shown that the electrochemical window of $[C_4mim][NTf_2]$ is 4.3 V when dried, but only 2.9 V when saturated with water [42].

The schematic of our EC SFA setup is shown in Fig. 3.1A. The EC SFA setup is a modification to the standard SFA 2000, which has been previously described [46]. In order to minimize the volume of ionic liquid required for each experimental measurement, a silicon dioxide (SiO_2) glass cup with a volume of 3 mL was designed to be a liquid reservoir. The base of the SiO_2 cup was coated with a 15 nm layer of titanium dioxide (TiO_2 - an adhesion promoter) followed by a 500 nm layer of platinum (Pt) to allow the base of the cup to be utilized as a counter electrode. TiO_2 and Pt were deposited via electron beam deposition. The electrical contact with the counter electrode was made by soldering a gold (Au) wire to the

base of the cup, and the solder contact point was isolated with ultraviolet (UV) curing glue. The UV glue used was NOA 81 (Norland Adhesives) and was found to be insoluble in $[C_4mim][NTf_2]$ when cured.

The bottom surface consisted of a single-crystalline sheet of back-silvered muscovite mica that was prepared using the standard procedure for preparing mica SFA surfaces [46]. Briefly, a single-crystalline mica sheet (back-silvered) was glued onto a cylindrical SiO_2 disc (radius, *R*, of 1 cm) using UV glue. The SiO_2 disc containing the mica surface was mounted into the base of the SiO_2 cup by also using UV glue.

The top surface consisted of a molecularly-smooth polycrystalline Au surface (0.2 nm RMS roughness – confirmed through AFM measurements) that functioned as the working electrode in the electrochemical setup. The molecularly-smooth Au electrode surfaces were prepared on 1 cm glass discs using the previously reported mica-templating procedure [47]: electron beam deposition was used to deposit a 42.5 nm thick film of Au onto a freshly-cleaved mica surface, which templates the Au to molecular smoothness at the mica-gold interface. The Au surface (still deposited on mica) was then glued to a cylindrical SiO_2 disk using UV glue, and immediately before beginning each experiment the mica surface was cleaved off of the Au, leaving behind a clean (fresh) molecularly-smooth Au surface.

3.7 References

1. Freemantle M. Designer solvents – ionic liquids may boost clean technology development. *Chem. & Eng. News* **76,** 32–37 (1998).
2. Rogers, Seddon K. Ionic liquids – solvents of the future? *Science* **302,** 792–793 (2003).
3. Galinski M., Lewandowski A., Stepniak I. Ionic liquids as electrolytes. *Electrochim. Acta* **51,** 5567–5580 (2006).

4. Weingärtner H. Understanding ionic liquids at the molecular level: facts, problems, and controversies. *Angew. Chem. Int. Ed.* **47,** 654–670 (2008).
5. Antonietti M., Kuang D., Smarsly B., Zhou Y. Ionic liquids for the convenient synthesis of functional nanoparticles and other inorganic nanostructures. *Angew. Chem. Int. Ed.* **43,** 4988–4992 (2004).
6. Ye C., Liu W., Chen Y., Yu L. Room-temperature ionic liquids: a novel versatile lubricant. *Chem. Commun.* **21,** 2244–2245 (2001).
7. Tsuzuki S., Tokuda H., Hayamizu K., Watanabe M. Magnitude and directionality of interaction in ion pairs of ionic liquids: relationship with ionic conductivity. *J. Phys. Chem. B* **109,** 16474–16481 (2005).
8. Armand M. et al. Ionic-liquid materials for the electrochemical challenges of the future. *Nature Mat.* **8,** 621–629 (2009).
9. Kornyshev A. A. Double-layer in ionic liquids: paradigm change? *J. Phys. Chem. B* **111,** 5545–5557 (2007).
10. Crowhurst L., Lancaster N. L., Pérez J., Welton T. Manipulating solute nucleophilicity with room temperature ionic liquids. *J. Am. Chem. Soc.* **126,** 11549–11555 (2004).
11. Castner E. W. Jr., Wishart J. F., Shirota H. Intermolecular dynamics, interactions, and solvation in ionic liquids. *Acc. Chem. Res.* **40,** 1217–1227 (2007).
12. Mezger M. et al. Molecular layering of fluorinated ionic liquids at a charged sapphire (0001) surface. *Science* **322,** 424–428 (2008).
13. Horn R., Evans D. F., Ninham B. W. Double-layer and solvation forces measured in a molten salt and its mixtures with water. *J. Phys. Chem.* **92,** 3531–537 (1988).

14. Bou-Malham I., Bureau L. Nanoconfined ionic liquids: effect of surface charges on flow and molecular layering. *Soft Matter* **6,** 4062–4065 (2010).
15. Ueno K. et al. Resonance shear measurement of nanoconfined ionic liquids. *Phys. Chem. Chem. Phys.* **12,** 4066–4071 (2010).
16. Perkin S., Albrecht T., Klein J. Layering and shear properties of an ionic liquid, 1-ethyl-3-methylimidazolium ethylsulfate, confined to nano-films between mica surfaces. *Phys. Chem. Chem. Phys.* **12,** 1243–1247 (2010).
17. Perkin S. et al. Self-assembly in the electrical double layer of ionic liquids. *Chem. Commun.* **47,** 6572–6574 (2011).
18. Hayes R., Warr G. G., Atkin R. At the interface: solvation and designing ionic liquids. *Phys. Chem. Chem. Phys.* **12,** 1709–1723 (2010).
19. Hayes R. et al. Double layer structure of ionic liquids at the Au(111) electrode interface: an atomic force microscopy investigation. *J. Phys. Chem. C* **115,** 6855–6863 (2011).
20. Zhou H. at al. Nanoscale perturbations of room temperature ionic liquid structure at charged and uncharged interfaces. *ACS Nano* **6,** 9818–9827 (2012).
21. Feng G., Cummings P. T. Supercapacitor capacitance exhibits oscillatory behavior as a function of nanopore size. *J. Phys. Chem. Lett.* **2,** 2859–2864 (2011).
22. Bazant M. Z., Storey B. D., Kornyshev A. A. Double layer in ionic liquids: overscreening versus crowding. *Phys. Rev. Lett.* **106,** 046102 (2011).
23. Lynden-Bell R. M., Frolov A. I., Fedorov M. V. Electrode screening by ionic liquids. *Phys. Chem. Chem. Phys.* **14,** 2693–2701 (2012).
24. Tokuda H. et al. How ionic are room-temperature ionic liquids? An indicator of the physicochemical properties. *J. Phys. Chem. B* **110,** 19593–19600 (2006).

25. MacFarlane D. R. et al. On the concept of iconicity in ionic liquids. *Phys. Chem. Chem. Phys.* **11,** 4962–4967 (2009).
26. Lockett V. et al. Differential capacitance of the double layer at the electrode/ionic liquids interface. *Phys. Chem. Chem. Phys.* **12,** 12499–12512 (2010).
27. Fedorov M. V., Kornyshev A. A. Towards understanding the structure and capacitance of electric double layer in ionic liquids. *Electrochim. Acta* **53,** 6835–6840 (2008).
28. Feng G., Zhang J. S., Qiao R. Microstructure and capacitance of the electrical double layers at the interface of ionic liquids and planar electrodes. *J. Phys. Chem. C* **113,** 4549–4559 (2009).
29. Parsegian V. A., Gingell D. On the electrostatic interaction across a salt solution between two bodies bearing unequal charges. *Biophys. J.* **12,** 1192–1204 (1972).
30. McCormack, Carnie, Chan D. Calculations of electric double-layer force and interaction free energy between dissimilar surfaces. *J. Coll. Int. Sci.* **169,** 177–196 (1995).
31. Hillier A. C., Kim S., Bard A. J. Measurement of double-layer forces at the electrode/electrolyte interface using the atomic force microscope: potential and anion dependent interactions. *J. Phys. Chem.* **100,** 18808–18817 (1996).
32. Fréchette J., Vanderlick T. Double layer forces over large potential ranges as measured in an electrochemical surface forces apparatus. *Langmuir* **17,** 7620–7627 (2001).
33. Lockett V. et al. Angle-resolved X-ray photoelectron spectroscopy of the surface of imidazolium ionic liquids. *Phys. Chem. Chem. Phys.* **10,** 1330–1335 (2008).
34. Lockett V. et al. Orientation and mutual location of ions at the surface of ionic liquids. *Phys. Chem. Chem. Phys.* **12,** 13816–13827 (2010).

35. Hunt P. A., Gould I. R., Kirchner B. The structure of imidazolium-based ionic liquids: insights from ion-pair interactions. *Aus. J. Chem.* **60,** 9–14 (2007).

36. Israelachvili J. N., Pashley R. M. Molecular layering of water at surfaces and ordering of repulsive hydration forces. *Nature* **306,** 249–250 (1983).

37. Christenson H. K., Gruen D. W. R., Horn R. G., Israelachvili J. N. Structuring in liquid alkanes between solid surfaces: force measurements and mean-field theory. *J. Chem. Phys.* **87,** 1834–1841 (1987).

38. Cummings P. T., Docherty H., Iacovella C., Singh. Phase transitions in nanoconfined fluids: the evidence from simulation and theory. *AIChE J.* **56,** 842–848 (2010).

39. Frink L. J. D., van Swol F. Solvation forces between rough surfaces. *J. Chem. Phys.* **108,** 5588–5598 (1998).

40. Atkins P., dePaula J. *Physical Chemistry* (Oxford Univ. Press, Oxford), 7th Ed., pp. 832–854 (2009).

41. Zhou Q., Fitzgerald K., Boyle P. D., Henderson W. A. Phase behavior and crystalline phases of ionic liquid-lithium salt mixtures with 1-alkyl-3-methylimidazolium salts. *Chem. Mat.* **22,** 1203–1208 (2010).

42. O'Mahony A. M. et al. Effect of water on the electrochemical window and potential limits of room-temperature ionic liquids. *J. Chem. Eng. Data* **53,** 2884–2891 (2008).

43. Valtiner M. et al. The electrochemical surface forces apparatus: the effect of surface roughness, electrostatic surface potentials, and anodic oxide growth on interaction forces, and friction between dissimilar surfaces in aqueous solutions. *Langmuir* **28,** 13080–13093 (2012).

44. Rappé A. K. et al. UFF, a full periodic table force field for molecular mechanics and molecular dynamics simulations. *J. Am. Chem. Soc.* **114,** 10024–10035 (1992).
45. Grahame D. C. Diffuse double-layer theory for electrolytes of unsymmetrical valence types. *J. Chem. Phys.* **21,** 1054–1060 (1954).
46. Israelachvili J. N. et al. Recent advances in the surface forces apparatus (SFA) technique. *Rep. Prog. Phys.* **73,** 036601 (2010).
47. Chai L., Klein J. Large area, molecularly smooth (0.2 nm rms) gold films for surface forces and other studies. *Langmuir* **23,** 7777–7783 (2007).
48. Israelachvili J. N., Tabor D. Measurement of van der Waals dispersion forces in range 1.5 to 130 nm. *Proc. Roy. Soc. Lon. Series A – Math. And Phys. Sci.* **331,** 19 (1972).

4 Long range electrostatic screening in ionic liquids

Gebbie M. A., Dobbs H. A., Valtiner M., Israelachvili J. N. *Proc. Natl Acad. Sci. USA* **112** (24), 7432–7437 (2015).

4.1 Abstract

Electrolyte solutions with high concentrations of ions are prevalent in biological systems and numerous energy storage technologies. Nevertheless, the high interaction free energy and long range nature of electrostatic interactions makes the development of a general conceptual picture of concentrated electrolytes a significant challenge. In this work, we study ionic liquids, single component liquids composed solely of ions, in an attempt to provide a novel perspective on electrostatic screening in very high concentration (non-ideal) electrolytes. We use temperature-dependent surface force measurements to demonstrate that the long range, exponentially decaying diffuse double-layer forces observed across ionic liquids exhibit a pronounced temperature dependence: increasing the temperature decreases the measured exponential (Debye) decay length, implying an increase in the thermally-driven effective free ion concentration in the bulk ionic liquids. We use our quantitative results to propose a general model of long range electrostatic screening in ionic liquids, where thermally-activated charge fluctuations, either free ions or correlated domains (quasiparticles), take on the role of ions in traditional dilute electrolyte solutions. This picture represents a crucial step towards resolving several inconsistencies surrounding electrostatic screening and charge transport in ionic liquids that have impeded progress within the interdisciplinary ionic liquids community. More broadly, our work provides a new way of envisioning highly concentrated electrolytes, with

implications for diverse areas of inquiry, ranging from designing electrochemical devices to rationalizing electrostatic interactions in biological systems.

4.2 Introduction

Electrolyte solutions are multicomponent liquids that are composed of ions (solutes) dissolved in a liquid phase (solvent), with a classic example being salt water. Like any ideal mixture, the driving force for the dissolution of ions in electrolyte solutions is entropic. Unlike ideal mixtures, the long range nature and high interaction free energy of the electrostatic interactions between ions ensures that the physical properties of all but the most dilute electrolyte solutions exhibit pronounced deviations from ideal behavior. These deviations primarily arise from the steric "crowding" of ions and the electrostatic correlation of ions, for example the formation of neutral ion pairs, both of which tend to increase the range of electrostatic interactions, as compared to ideal solutions [1]. As a result, the development of a general conceptual picture of concentrated electrolyte solutions remains challenging. Nevertheless, electrolytes with high ionic concentrations are prevalent in biological systems [2] and technological applications, such as energy storage devices [3–5], so overcoming this challenge remains an important task.

In this work, we study room temperature ionic liquids (RTILs), single component liquids composed solely of ions, in an attempt to provide a starting point for a new conceptual understanding of electrostatic screening in concentrated electrolytes. While RTILs do not have neutral solvent molecules separating the ions, the high degrees of ion "crowding" and electrostatic correlations present in RTILs are expected to be fundamentally related to ion "crowding" and electrostatic correlations in highly concentrated electrolyte solutions [5]. To date, thousands of RTILs have been identified with diverse physical properties that can be

tuned via careful design of cation-anion pairs [6]. While these properties are largely governed by the same strong Coulombic interactions that underlie the 801 °C melting point of crystalline sodium chloride, the large sizes and asymmetric charge distributions of RTIL ions suppress the formation of ordered crystals. Notably, the high thermal and electrochemical stabilities, negligible volatilities, and variable intrinsic ionic conductivities of many RTILs make them promising materials for numerous applications, including: electric double-layer capacitors, batteries, and self-assembly media [3–10]. Many of these applications depend critically on interfaces between charged surfaces and RTILs. Nevertheless, the fundamental characteristics of RTIL electric double-layers remains an active area of research and discussion [5, 11].

A generally accepted picture is that the electric double-layers formed by RTILs consist of ordered layers of cations and anions, with these perturbed ionic concentrations quickly approaching bulk distributions on the order of several ionic diameters [5]. Much of this understanding was developed through nanoscale computational studies of coarse-grained ionic systems [5, 11–16] that are reminiscent of high temperature molten salts. These studies predict that the electric double-layers formed by RTILs should be short range and exhibit pronounced charge density oscillations, similar to the screening behavior identified in pioneering work on molten KCl [15]. Recent theoretical studies emphasize that complex ion ordering in RTILs can intimately depend on the electrochemical potentials of the charged surfaces [5, 17–19], but these studies have left intact the picture that the electric double-layers formed by RTILs should be very short ranged.

Experimentally, the short range, surface-induced ordering of ions in RTILs has been confirmed with x-ray scattering experiments, atomic force microscopy (AFM) force measurements and surface forces apparatus (SFA) measurements [17, 20–23], with these

studies highlighting that the ordering of RTIL ions at surfaces exhibits many subtleties. For example, Atkin and coworkers [22] used AFM to demonstrate that gold electrode surfaces immersed in RTILs can undergo ion-mediated surface reconstructions under externally applied electrochemical potentials. Perkin et al. [23] have shown that RTIL ions self-assemble into ordered (smectic-like) bilayers when the cations contain pronounced nonpolar domains. Recent SFA measurements have added to these pictures by demonstrating the presence of a long range monotonic, exponentially decaying, equilibrium force that extends to distances of up to 35 ionic diameters per surface [24, 25]. Modeling this force as a diffuse double-layer interaction with a decay length corresponding to the Debye length led to the hypothesis that RTILs can be conceptualized as very weakly dissociated electrolyte "solutions," where the electrostatic screening behavior is dominated by a small population of effectively dissociated ions [24].

However, the molecular mechanism of this apparent ion dissociation in RTILs remained to be explored. Unlike conventional, fully dissociated dilute electrolyte solutions where the free ion concentration is independent of temperature and the Debye length only modestly increases with temperature, one would expect the concentration of effectively dissociated ions and Debye length of RTILs, and other highly concentrated electrolytes where ionic aggregation is prominent, to strongly depend on the temperature. For these weakly dissociated electrolytes, increasing the temperature will dissociate ionic aggregates, significantly decreasing the Debye length.

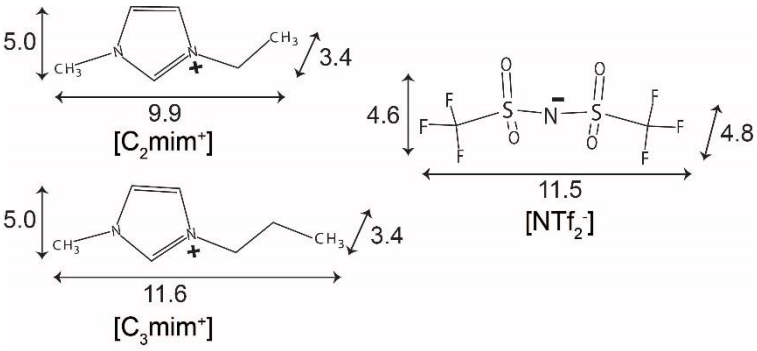

Figure 4.1. Chemical structures and approximate dimensions of the RTIL ions. Molecular dimensions were calculated from the van der Waals radii of the constituent atoms.

Using the SFA technique, we studied two common aprotic ionic liquids with the bis(trifluorosulfonyl)imide (NTf_2) anion and two different 1-alkyl-3-methylimidazolium cations: $[C_2mim]^+$ and $[C_3mim]^+$ (Fig. 4.1). Our results suggest that a long range, monotonic force may be a general feature of the electric double-layers formed by RTILs in contact with macroscopic charged surfaces, whenever surface-bound ion layers are unable to fully compensate surface charges. For mica surfaces, we find this long range force to be in series with a short range, non-monotonic "oscillatory" structural force that is in agreement with the nanoscale surface-induced ion ordering identified in previous work on RTILs [17, 20–25]. Further, we show that the long range screening behavior of RTILs can be rationalized via a thermally-activated population of either free ions or correlated charge domains, reminiscent of the free electron/hole approximation used in semiconductor physics.

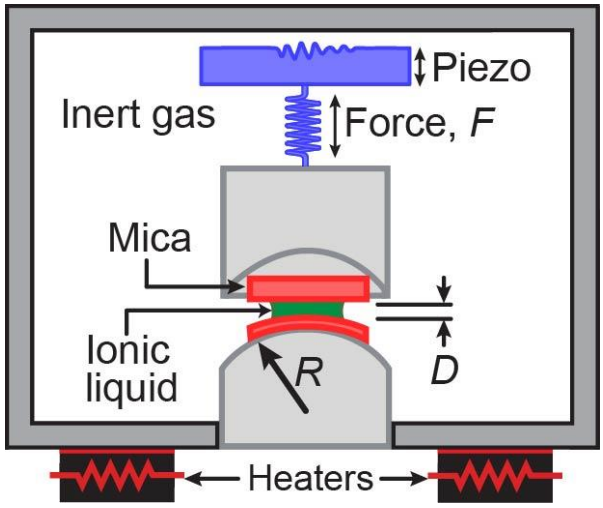

Figure 4.2. Schematic of the surface forces apparatus (SFA) [26]. The temperature was controlled via resistive heaters, and the distance between the two surfaces, *D*, was defined with respect to the contact of the two mica surfaces in the absence of RTIL, where $D = 0$.

4.3 Results and analysis

4.3.1 Equilibrium force-distance measurements

Force-distance $F(D)$ measurements were performed using a standard Surface Forces Apparatus 2000 (SFA) [26], with resistive heating coils incorporated into the steel SFA housing (Fig. 4.2). A detailed description of the force and distance measuring methods can be found in Ref. 26. Briefly, the top surface was actuated at constant Å/s displacement rates via a piezoelectric crystal, while the distance between the surfaces, *D*, was monitored with Å-scale resolution through interferometry. The two surfaces move at constant rates when the surfaces are not interacting, and colloidal interaction forces cause the surfaces to accelerate or decelerate. The deflection of a double cantilever spring was used to determine the interaction force between the two surfaces at each distance to nN resolution. This procedure enabled us to determine the distances between, and forces across, the surfaces with experimental errors of $F/R = \pm 0.02$ mN/m and $D = \pm 0.2$ nm.

Each SFA experiment was set up with two freshly prepared single-crystalline mica surfaces. $[C_2mim][NTf_2]$ and $[C_3mim][NTf_2]$ were synthesized, purified, dried, and characterized using a previously established procedure for the preparation of electrochemical-grade RTILs [27]. The sizes of these $[C_Rmim]^+$ cations and $[NTf_2]^-$ anions (Fig. 4.1) both exceed the size of the 4 Å radius of K^+ sites on mica surfaces, and mica surfaces develop negative surface potentials [17, 23–25] when exposed to bulk $[C_Rmim][NTf_2]$ RTILs. This negative potential likely develops through a combination of the dissociation of surface-bound K^+ ions present at cleaved mica surfaces, which are then replaced by larger $[C_Rmim^+]$ cations – "crowding" [13] – and/or the overadsorption of $[NTf_2]$ anions in the first surface-bound RTIL layer – "overscreening" [13]. Our experiments cannot distinguish between these two possibilities, and the actual negative potential of mica surfaces may result from a complex combination of these two mechanisms. The resulting K^+ concentration in the RTILs would be negligible, even if every K^+ ion were to be replaced by $[C_Rmim]^+$ cations.

Forces were measured on approach rates below which dynamic forces are negligible, as ascertained by forces that are independent of approach rates. Representative force-distance profiles, $F(D)$, measured while bringing together two mica surfaces across $[C_2mim][NTf_2]$ and $[C_3mim][NTf_2]$ are shown by the data points in Fig. 4.3. Attractive forces arising from separating the surfaces more quickly than the extremely long times required for the viscous RTILs to flow back into the interface were measured during retraction of the mica surfaces, even for separation rates as slow as 2 Å/s (Fig. 4.4). Only equilibrium force-distance measurements are reported in this study.

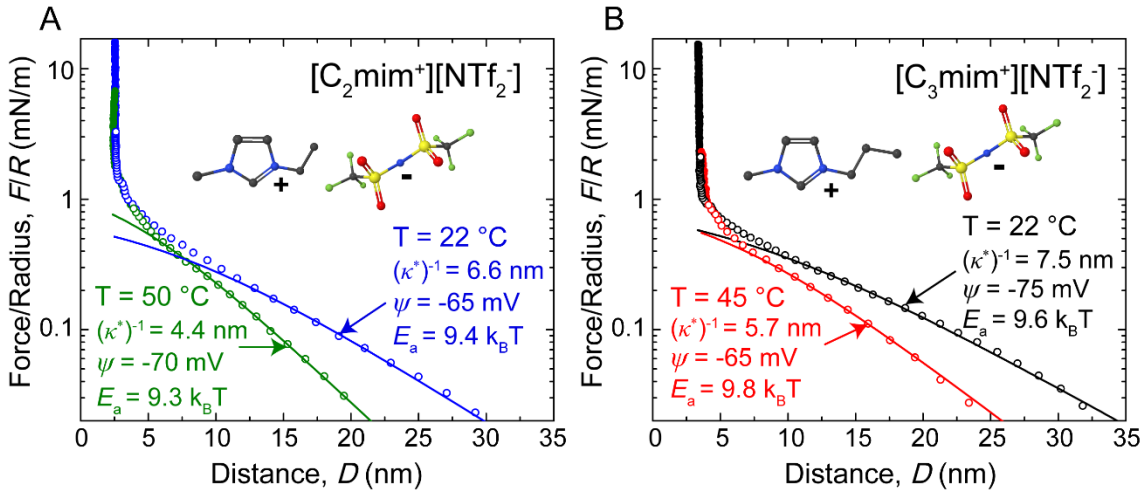

Figure 4.3. Representative force-distance profiles measured across A) $[C_2mim][NTf_2]$ at T = 22 °C (blue data points) and 50 °C (green data points) and B) $[C_3mim][NTf_2]$ at T = 22 °C (black data points) and 45 °C (red data points). The open circles represent distances where the forces were measured without surface deformations, and the filled circles indicate progressive flattening of the surfaces under increasing loads, where the pressure applied to the bound ion layers stays approximately constant. The solid lines are fitted using the diffuse double-layer interaction potential, Equation 4.1. The interaction potential is plotted for all D, but fits were numerically optimized for $D > 1.5\ (\kappa^*)^{-1}$, as discussed in the text. The parameter values presented on the plot correspond to the fitted parameters of the representative data. The average fitted parameters and standard errors are presented in Tables 4.1 and 4.2.

To increase the sensitivity of our measurements in the long range regime of the force-distance profiles ($10 < D < 100$ nm), we employed surfaces with larger radii (lower curvatures) than the typical 1-2 cm radius surfaces used previously by us and other researchers [23–25]. This strategy is similar to using colloid probes in AFM to increase sensitivity of AFM measurements to weak, long range colloidal forces. The 4–5 cm radius surfaces we used in the majority of these experiments enabled us to increase our sensitivity to colloidal forces by a factor of ~5 relative to our previous measurements, where we used surfaces with R≈1 cm radii [24], as the force resolution is set by the absolute value of the measured forces, while the

magnitudes of the long range double-layer forces scale as F/R, via the Derjaguin approximation [26, 28]. The inherent trade-off to this strategy is that extensive surface deformations (flattening) begin to occur at surface separations D < 5 nm with the larger radius surfaces, limiting the final pressures that we can apply to the strongly surface-bound ion layers. As a result, we cannot fully "force out" all of the ion layers to access the entire range of "oscillatory" forces [21–23].

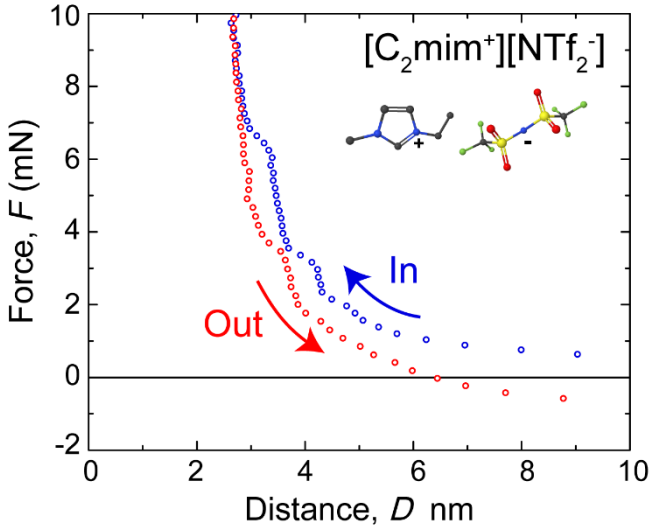

Figure 4.4. Representative short range interaction forces measured across $[C_2mim][NTf_2]$ with R = 1 cm surfaces on approach (blue) and separation (red). The y-axis is presented in units of force, F (without R normalization), as the Derjaguin approximation fails within the "oscillatory" regime due to a combination of surface deformation and curvature effects. On separation, we still observe evidence of solvation and double-layer forces; however these equilibrium forces are superimposed on an additional weakly-attractive dynamic force. This dynamic attractive force results from separating of the surfaces at rates that exceed the extremely long times required for the viscous RTILs to flow back into the interface under equilibrium conditions. Thus, the red points should not be interpreted as true equilibrium forces. In the absence of dynamic effects and/or energy dissipation, the forces measured when separating the two surfaces should exactly overlay the forces measured when bringing the two surfaces together.

To ensure consistency with previous studies and to rule out large surface radii as the origin of the monotonic forces we report, we also prepared 1 cm radius surfaces for a subset of experiments. These experiments exhibited quantitative agreement with the larger radius surfaces in the intermediate ranges of the force-distance profiles (D > 5 nm) and enabled us to measure pronounced non-monotonic forces at surface separations of D < 5 nm. Representative results we obtained with these 1 cm surfaces are presented in Fig. 4.5.

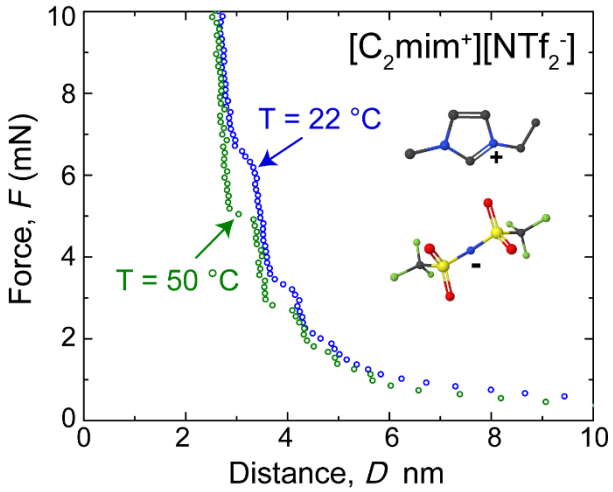

Figure 4.5. Representative short range interaction forces measured across [C_2mim][NTf_2] with R = 1 cm surfaces at room temperature (blue) and 50 °C (green). The y-axis is presented in units of force, F (without R normalization), as the Derjaguin approximation fails within the "oscillatory" regime due to a combination of surface deformation and curvature effects. For the room temperature force profile (blue), $(\kappa^*)^{-1}$ = 6.7 nm and ψ = 80 mV. For the 50 °C force profile (green), $(\kappa^*)^{-1}$ = 4.2 nm and ψ = 100 mV.

4.3.2 Dynamic force-distance measurements

When bringing the mica surfaces together, we found dynamic forces to be unmeasurably small, within error, for the approach rates we report in this manuscript (5–10 Å/s). In contrast, we always measure dynamic attractive forces when separating the two

surfaces, even for separation rates as slow as 2 Å/s (Fig. 4.4). These attractive dynamic forces are much stronger than those that would be predicted via traditional hydrodynamic drag models that assume continuum fluids of bulk viscosity.

From a molecular point of view, the magnitudes of these dynamic forces should be significantly larger on separation than approach, in agreement with our experimental results, due to differences in the fluid flow mechanisms when the RTIL ions flow out of, rather than into, nano-confined gaps. The expulsion of ions out of confined spaces should only involve molecular motions on the order of ionic diameters for layered instabilities.

In contrast, the fluid must be moved out of the bulk reservoir and into the entire micron-scale area of the nano-confined interface as two surfaces are pulled apart, involving the motion of many RTIL ions over distances that are extremely large compared to the size of the individual ions. This is likely a much slower and more complex process than the expulsion of ions. Separation rates on the order of Å/min or even Å/hr would likely be required to avoid overloading the spring and inducing additional non-equilibrium dynamic attractions as the surfaces are separated. Unfortunately, such slow separation rates are impractical for our experiments, as we need to collect dozens of force runs at different temperatures.

4.3.3 Analysis of force-distance profiles

The lines plotted in Fig. 4.3 correspond to fits of a constant potential solution to the linearized Poisson-Boltzmann equation, Equation 4.1, to the asymptotic long range distance regime of each force profile, $D > 1.5\ (\kappa^*)^{-1}$, where the equation is well approximated by a simple exponential decay [28, 29].

$$\frac{F}{R} = 2\pi E = \frac{8\pi e^2 n^*}{k_B T \kappa^*} \frac{\psi^2 (1 - \exp(-\kappa^* D))}{\exp(\kappa^* D) - \exp(-\kappa^* D)} \approx \frac{8\pi e^2 n^*}{k_B T \kappa^*} \psi^2 \exp(-\kappa^* D) \qquad (4.1)$$

$$(\kappa^*)^{-1} \equiv \sqrt{\frac{\varepsilon \varepsilon_0 k_B T}{2 n^* (q^*)^2}} \qquad (4.2)$$

Where $(\kappa^*)^{-1}$ (m) is the effective Debye length, n^* (m^{-3}) is the number density of effective charge carriers (free ions or coordinated aggregates of ions that behave as electrostatic monopoles, i.e, "quasiparticles"), $q^* = ze$ (C) is the effective carrier charge, $z = 1$ is the carrier valence, ψ (V) is the diffuse double-layer potential of the mica surfaces, ε = 12.3 for $[C_2mim][NTf_2]$ and ε = 11.6 for $[C_3mim][NTf_2]$ is the (measured) low frequency bulk dielectric permittivity [30], ε_0 (F/m) is the vacuum permittivity, T (K) is the temperature, and k_B (J/K) is the Boltzmann constant. At distances of $D \leq (\kappa^*)^{-1}$, the $F(D)$ profiles deviate from the predictions of mean-field theory and exhibit non-monotonic "oscillatory" features. The ranges and magnitudes of these repulsive forces are consistent with previous work that attributed these oscillatory forces to the ordering of the RTIL ions next to charged mica surfaces, with the instabilities corresponding to the abrupt ejection of mixed layers of ions into the reservoir [21–25].

Table 4.1. $[C_2mim][NTf_2]$ Average electrostatic parameters (Equations 4.1 and 4.2) and calculated activation energies (Equation 4.4).

Temperature, (°C)	**Effective Debye length, $(\kappa^*)^{-1}$ (nm)**	**Diffuse double layer potential, Ψ (mV)**	**Activation energy, E_a (k_BT_{295})**
22	6.7 ± 0.1	90 ± 25	9.4
40	5.7 ± 0.1	100 ± 20	9.6
50	4.3 ± 0.5	90 ± 25	9.3
60	3.4 ± 0.2	100 ± 25	9.1

Table 4.2. [C_3mim][NTf_2] Average electrostatic parameters (Equations. 4.1 and 4.2) and calculated activation energies (Equation 4.4).

Temperature, (°C)	Effective Debye length, $(\kappa^*)^{-1}$ (nm)	Diffuse double layer potential, Ψ (mV)	Activation energy, E_a (k_BT_{295})
22	7.4 ± 0.1	72 ± 9	9.6
32	6.6 ± 0.2	75 ± 7	9.7
45	5.5 ± 0.5	66 ± 4	9.8
74	3.5 ± 0.2	50 ±11	9.5

The average values of the fitting parameters obtained from analyzing force-distance profiles measured over multiple independent experiments are found in Tables 4.1 and 4.2. The quoted uncertainties are based on statistical analysis of at least 15 different force profiles for each temperature, with a 95% confidence interval. Forces were also measured at intermediate and higher temperatures to those shown in Figure 4.3.

Based on the current literature, a mean-field theory describing the distributions of point charges would appear be incapable of capturing the asymptotic decay behavior of the electric double-layers formed by RTILs. Indeed, if every ion is assumed to independently contribute to electrostatic screening (i.e., full "dissociation") then the room temperature Debye length of the [C_2mim][NTf_2] and [C_3mim][NTf_2] RTILs used in this study should be on the order of 0.1 Å (calculated with ε = 1–10), which is orders of magnitude smaller than the ionic sizes. However, we propose that the much larger interaction decay lengths that we measure across [C_2mim][NTf_2] and [C_3mim][NTf_2], $(\kappa^*)^{-1}$ = 6.6 nm and 7.5 nm (room temperature), respectively, are effective Debye lengths, where the effective ionic strength (activity) of the RTILs, n^* (m^{-3}), substantially differs from the total ionic concentration determined from the RTIL density and molar mass.

The effective Debye lengths that we report always exceed the accepted theoretical Bjerrum length, l_B [5], for $[C_2mim][NTf_2]$ and $[C_3mim][NTf_2]$ (4.6 and 4.9 nm at room temperature), Equation 4.3:

$$l_B = \frac{ze^2}{4\pi\varepsilon\varepsilon_0 k_B T} \tag{4.3}$$

Where e (C) is the elementary charge, ε_0 is the vacuum permittivity, ε is the relative permittivity of each RTIL, k_B (J/K) is the Boltzmann constant, and T (K) is the temperature. l_B is the distance beyond which electrostatic interactions between free ions or quasiparticle domains are disrupted by thermal energy. Thus, our rescaled mean-field approach fulfills the fundamental requirement that $(\kappa^*)^{-1} > l_B$. For particles and/or length scales that are smaller than l_B, RTILs cannot be modeled using this approach.

As an extension of our recent "dilute electrolyte" analogy [24], we rationalize these measured effective ionic strengths by considering RTILs to behave as thermally dissociable dielectric fluids that are in equilibrium with a Boltzmann-distributed population of either free ions or quasiparticle "ions" (electrostatic monopoles) that exceed a RTIL specific activation energy, E_a. We are not suggesting that the RTIL ions form exclusive ion pairs where each ion coordinates with only one specific counterion, rather we propose that the strong Coulombic interactions between RTIL ions that drive local charge neutrality by causing each cation to be preferentially surrounded by anions (and vice versa), result in the bulk fluid behaving, for large ensembles, as a dipolar network. This picture is consistent with x-ray and neutron reflectivity measurements that independently establish that the strong electrostatic interactions between RTIL ions drive the ions to order into nanoscale bicontinuous cation-anion networks [31, 32]. In our model, we use the measured bulk low frequency dielectric permittivities, ε, [30] to account for the dielectric behavior of this network. Thermally activated charge

fluctuations, either free ions or correlated charge domains, then behave as (mathematical) point charges (Fig 4), taking on the role of ions in the traditional Poisson-Boltzmann model for dilute electrolyte solutions.

As an example of the underlying physics, even a simple ion, like K+, is, in reality, composed of highly correlated charged particles (protons and electrons), with the formal positive charge coming from one missing electron. Nevertheless, K^+ ions can be modeled as point charges for length scales (Gaussian surfaces) that are much larger than the ångstrom-scale size of K^+ ions. For RTILs, the length scales (Gaussian surfaces) over which electrostatic screening in RTILs can be envisioned in terms of point charges needs to be large enough average over distances that exceed l_B (Fig. 4.6). This picture shares conceptual similarities with the "Dressed Ion" theory of electrolyte solutions [29], an exact statistical mechanical theory that uses charged quasiparticles to model the electrostatic interaction forces between surfaces that are immersed in (non-ideal) primitive model electrolyte solutions. However, RTILs have yet to be fully analyzed within this framework.

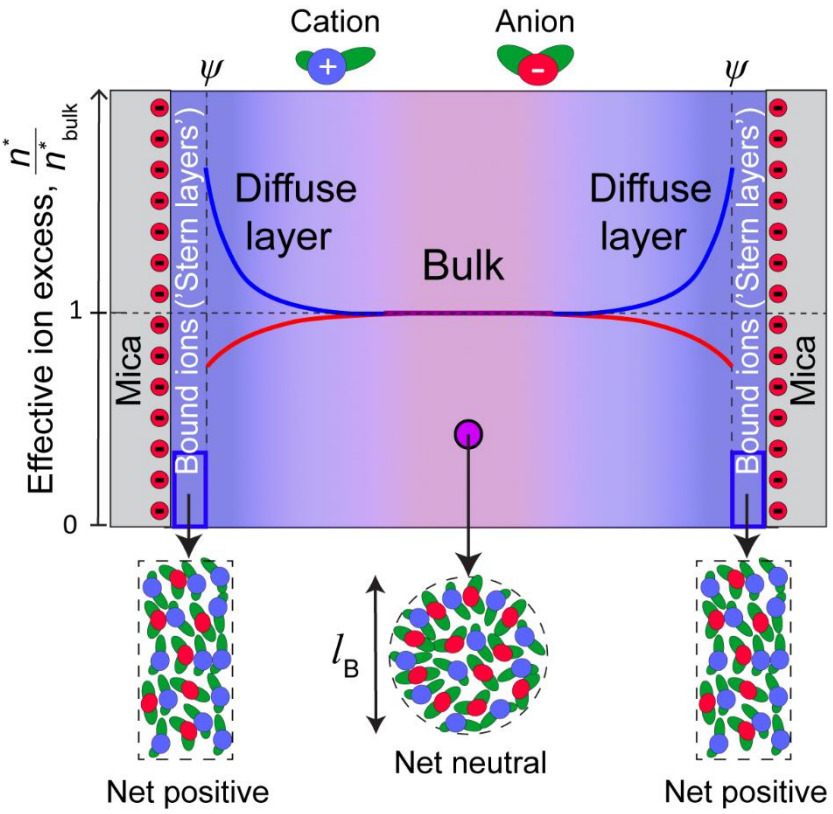

Figure 4.6. Electric double-layers formed by the RTILs between two surfaces with $D >> (\kappa^*)^{-1}$. In the "Bound ions ('Stern layers')" region a portion of the negative surface charge is screened via surface-bound cation-rich ion layers. For $[C_2mim][NTf_2]$ and $[C_3mim][NTf_2]$ at mica surfaces, this region extends approximately 4–6 ion layers per surface. In the "Diffuse layer" the residual negative potential – the diffuse layer potential, ψ, - is screened via a monotonic, steeply decaying concentration of excess positive charge. The blue (cation) and red (anion) lines and blue (positive)-to-purple (neutral) shading approximate the smeared-out excess effective ionic concentrations throughout the diffuse double-layer, n^*/n^*_{bulk}. The temperature dependence of the measured decay (Debye) length demonstrates that the charge carriers can be viewed as a Boltzmann distributed population of effective ions with thermal energy exceeding a RTIL specific activation energy, E_a. The purple circle in the region labeled "Bulk" has a diameter that is approximately the Bjerrum length, l_B (Equation 4.3). RTILs behave as nanoscale, highly charge ordered (correlated) liquids over distances shorter than l_B.

The physical relevance of viewing bulk RTILs as thermally dissociable dielectric fluids is substantially strengthened by our observation that the measured effective Debye lengths, $(\kappa^*)^-$

[1], decrease as the temperature increases. In the absence of thermally driven ion dissociation, double-layer interactions would *increase* in range at higher temperatures. Furthermore, several recent theoretical studies proposing that RTILs already behave as highly dissociated (uncorrelated) "electrolytes" at room temperature also appear to predict that the electric double-layers formed by RTILs should increase in range with increasing temperature [5, 11]. In contrast, our weakly dissociated "dilute electrolyte" model [24] predicts that the double-layers formed by RTILs should decrease in range with increasing temperature, as we observe in the current study. Thus, these temperature-dependent measurements provide an unambiguous way to distinguish between the various models.

4.3.4 Calculation of charge carrier activation energies

Charge carrier activation energies of $E_a = 9.4 \pm 0.3\ k_BT$ for $[C_2mim][NTf_2]$ and $E_a = 9.7 \pm 0.2\ k_BT$ for $[C_3mim][NTf_2]$ were calculated from the Boltzmann distribution, Equation 4.4:

$$n^* = n_{tot} \exp(\frac{-E_a}{k_B T}) \qquad (4.4)$$

Where n^* (m^{-3}) is the (measured) number density of effective charge carriers, n_{tot} (m^{-3}) is the total ionic concentration, as determined from the RTIL density and molar mass, and E_a is the charge carrier activation energy. E_a values are reported in units of k_BT with T = 295 K. The calculated values of E_a were found to be constant over the 22-75 °C temperature range studied, consistent with an electrostatic screening mechanism that is dominated by thermally excited charge carriers. This temperature independence is not expected to hold for substantially elevated temperatures. For extremely high temperatures ($T \geq 1500$ K), the Bjerrum length would become smaller than the size of the RTIL ions, and n^* will approach the actual molar density of the RTILs. If this temperature limit could be reached without decomposing the

RTIL ions, then RTILs should behave as fully "dissociated" ionic melts, as has been observed for high temperature molten salts [5, 15].

These activation energies of $E_a = 9.4 \pm 0.3$ k_BT for $[C_2mim][NTf_2]$ and $E_a = 9.7 \pm 0.2$ k_BT for $[C_3mim][NTf_2]$ compare well with the activation energy of $E_a = 11$ k_BT that we determined for $[C_4mim][NTf_2]$ [24] and follow the same trend as the dielectric permittivity for this $[C_2mim][NTf_2]$, $[C_3mim][NTf_2]$, $[C_4mim][NTf_2]$ series of RTILs. Using our previous approach of estimating the charge carrier activation energy as the energy required to separate a reference RTIL ion pair within a bulk dielectric fluid also works well for these two RTILs (Equation 4.5).

$$E_a = \Delta\mu^i \approx \frac{\Delta E_d}{\varepsilon} \tag{4.5}$$

Where ΔE_d is taken as the calculated vacuum interaction energy between a $[C_Rmim]^+$ cation and $[NTf_2]$ anion averaged over all configurations, and ε, corresponds to the measured low frequency bulk permittivity for each RTIL. For example, the ΔE_d of 132 k_BT [33] and ε of 12.3 [30] for $[C_2mim][NTf_2]$ yields an estimated E_a of 10.7 k_BT, which agrees with the measured E_a of 9.4 k_BT to within 15%. The success of such a simple electrostatic model highlights that electrostatic interactions are the primary determinant of the measured E_a. Further, the simplicity of this molecular-scale model may enable one to quickly estimate, and ultimately tune, the electrostatic screening of properties of RTILs by judiciously balancing bulk dielectric properties with molecular ion pair interaction energies.

Notably, if effectively free "dissociated" ions are taken to be the charge carrier that dominates diffuse layer screening, then these $[C_Rmim][NTf_2]$ RTILs, and by extension other similar aprotic RTILs, would exhibit bulk dissociated ion concentrations of less than 0.1% at

room temperature. A similar approach was recently proposed to model the bulk autoionization of pure water [34].

4.3.5 Short range non-monotonic forces and colloidal stability

The non-monotonic features (~0.5 nm plateaus) in the force-distance profiles correspond to "oscillatory" transitions, where ordered layers of ions are forced out from between the mica surfaces and into the bulk reservoir (Fig. 4.5). Given the highly correlated nature of strongly interacting RTIL ions, we expect that these ion layers consist of both cations and anions but are enriched in cations, due to the negative mica surface potential. The surface separation distance at which we detect the first oscillation is $D \approx 5$ nm (~2.5 nm per surface) for both $[C_2mim][NTf_2]$ and $[C_3mim][NTf_2]$, in excellent agreement with previous measurements across other RTILs [22–26]. Assuming that the plateau distance of ~0.5 nm for each RTIL corresponds to a characteristic effective molecular "diameter" for each ion pair, the RTILs form solvation layers of about 5 molecular "diameters" per surface.

As the temperature is raised, the number and location of observed ion layers remains unchanged, and the layers are forced out of the interface under similar compressions, with an observed likelihood of being removed under slightly decreased pressures at increased temperatures. This observation suggests that the ions pack into similar surface-induced structures for the entire temperature range of 22–75 °C. Perhaps the strong Coulombic interactions between RTIL ions enables them to maintain surface-induced structures at these elevated temperatures. However, the solvation layers formed by cyclohexane confined between mica surfaces was also observed to remain unchanged between 22–41 °C [40].

At all temperatures, the surfaces begin to progressively flatten under very large applied loads ($F > 10$ mN). Once the surfaces enter this regime of flattening, the surface area increases

in proportion to the load, so the pressure applied to the strongly bound ion layers stays approximately constant. As a result, no additional ions are forced out of the interface. For $[C_2mim][NTf_2]$, the final film thickness was measured to be ~2.5 nm under high loads. Noting that each ion layer that is forced out of the interface yields a plateau that is ~0.5 nm in distance, we conclude that the measured final film thickness of ~2.5 nm corresponds to a confined structure consisting of between 4-6 total layers of ions between the surfaces (2–3 ion layers per surface). The final film thickness increases to ~ 3 nm for $[C_3mim][NTf_2]$. Since the $[C_3mim]^+$ cation is larger than the $[C_2mim]^+$ cation by only one $–CH_2-$ group, the final number of confined ion layers most likely corresponds to the same number of ion layers or, at most, one additional ion layer at high compressions for $[C_3mim][NTf_2]$.

In comparison, seminal experiments on the formation of (room temperature) solvation layers by traditional liquids demonstrate that the range of surface-induced layering can be as short as 1 nm per (mica) surface for small, highly mobile molecules like water [41], and as long as 4.5 nm per (mica) surface for octamethylcyclotetrasiloxane (OMCTS) [42], a large oblate spheroid molecule. For a wide variety of polar and nonpolar liquids confined between mica surfaces, liquids typically form solvation layers that extend to distances of about 5 molecular diameters (of the liquid) per surface at room temperature [42–44]. These layers result in alternating repulsive and attractive "oscillatory" contributions to the force-distance profiles measured across confined liquids, analogous to those measured across RTILs. For traditional liquids, these "oscillatory" forces are always superimposed with the van der Waals and electric double-layer forces of standard DLVO theory [40–42].

For $[C_2mim][NTf_2]$ and $[C_3mim][NTf_2]$ confined between mica surfaces, these "oscillatory" solvation forces are clearly superimposed with a strongly repulsive electrostatic

force, as shown in Fig 3. Surface-surface van der Waals interactions also occur across RTILs, and the dielectric/optical properties of RTILs should be used to account for the screening of van der Waals attractions. In the current study, the combination of strongly repulsive double-layer and solvation forces overwhelms any possible van der Waals attraction down to the final measured separation distances of $D \sim 2.5–3$ nm.

While the formation of solvation layers by RTILs in contact with solid surfaces is one of the most widely discussed aspects of RTIL interfaces, we conclude RTILs show a propensity for forming solvation layers that is similar to many other polar and non-polar liquids.

The practical implication of this conclusion is that is that the solvation layers formed by RTILs should be viewed as fundamentally similar to the solvation layers formed by other liquids. Namely, these solvation layers will indeed contribute to colloidal stability, but the ultimate dispersion (aggregation) state of colloidal particles immersed in RTILs will also critically depend on other colloidal interactions. After all, a knowledge of solvation interactions alone is not sufficient to predict the colloidal stability of particles immersed in other liquids that form solvation structures of comparable ranges and magnitudes.

4.4 Discussion, conclusions, and outlook

The electrostatic screening properties of $[C_2mim][NTf_2]$ and $[C_3mim][NTf_2]$ that we report in the current study are in excellent agreement with our previous study of $[C_4mim][NTf_2]$ in electrochemically active interfaces [24]. In both studies, we find that the electric double-layers formed by RTILs exhibit a near surface regime composed of multiple strongly bound layers of ions, where the degree of ordering of the bound ion layers depends on the crystallinity of the confining surfaces. This ubiquitous near surface regime is in series with a longer range exponentially decaying diffuse double-layer, when the bound ion layers

cannot fully screen charged surfaces (Fig 4.6). In essence, we propose a Gouy-Chapman-Stern [1] picture of electric double-layers in RTILs, where the bound Stern layer is several ion layers thick, and the diffuse layer "ions" are either free ions or charged quasiparticles.

A key implication of this study, and of our previous work [24], is that long range electrostatic interactions should be observed when $[C_Rmim][NTf_2]$ RTILs are confined between (mica) surfaces. In agreement with this prediction, Espinosa-Marzal and colleagues [25] measured similar long range electrostatic interactions between two mica surfaces across $[C_2mim]^+$ and $[C_6mim]^+$ based RTILs. In contrast, Perkin and coworkers studied $[C_4mim][NTf_2]$ and $[C_6mim][NTf_2]$ between symmetric mica surfaces using an SFA [23], but did not report any long range electrostatic interactions. Perhaps the origin of this discrepancy is that Perkin et al. focused on short range ion structuring interactions, which would make the simultaneous identification of weaker long range interactions challenging. From our point of view, there may be a monotonic repulsion in the $D > 8$ nm portion of the force-distance profiles presented by Perkin et al for $[C_4mim][NTf_2]$ in Fig. 2 of Ref. 23.

As noted previously [5], the groundbreaking SFA measurements by Horn and coworkers [21] on a RTIL confined between mica surfaces also reported solely short range ion structuring interactions. Horn et al. studied the protic RTIL ethylammonium nitrate (EAN), and recent AFM work [35] demonstrate that RTILs with small primary ammonium cations like EAN bind to mica surfaces with an epitaxial cation spacing that matches the charge site spacing of the underlying mica substrates. In contrast, the sizes of $[C_Rmim]^+$ cations significantly exceed the 4 Å radius of charge sites on mica surfaces. Thus, we hypothesize that the lack of long range interactions across EAN arises from an epitaxial compensation of mica surface charges

by bound ion layers, an effect that is reminiscent of our observation that [C_4mim][NTf_2] can fully screen negative gold electrodes via bound ion layers [24].

RTILs are typically imagined as strongly dissociated, highly concentrated "electrolytes" when viewed from the perspective of nanoscale simulations [5]. In contrast, our experiments portray RTILs as extremely weakly dissociated "electrolytes." We reconcile this apparent contradiction by proposing that the degree of ionic correlations and resultant apparent dissociation of RTIL ions very likely depends on the observed length and time scales of the experiment or computation. Similar ideas have been used to explain why RTILs appear to simultaneously behave as highly polar liquids ($\varepsilon > 50$) over short distance and time scales, but as moderate polarity liquids ($\varepsilon = 10–15$) over larger distances and longer times [30, 36].

Perhaps the apparently independent diffusion of neighboring ions identified in molecular dynamics simulations [5] only looks independent for the very short length and time scales, and the small number of ions, available to current simulations. Our results reveal that much larger ensembles of ions exhibit complex collective phenomena featuring qualitative differences - in both distance and time - from the behavior identified in nanoscale simulations of ions. Thus, our results should prove useful for the design of energy storage devices, such as electrochemical capacitors [3], where RITLs form double-layers at extended surfaces and ionic association strongly impacts the stored energy density and conductivity properties of electrochemical devices.

As a practical example, the double-layer capacitance of several RTILs significantly increases with increasing temperature [5], an effect that Lockett and colleagues [37] explained via the thermal dissociation of neutral ionic aggregates. Our current work supports this hypothesis and provides a quantitative framework for estimating the activation energy of ion

dissociation in aprotic RTILs, yielding additional insight into the electrochemical performance of RTIL-based capacitors. More broadly, we provide a molecular-scale framework that can be used to design RTILs with carefully tuned degrees of ionic association by balancing ion pair interaction energies with bulk dielectric properties.

Beyond RTILs, the general physical insight we offer is that the simple picture of dissociation equilibria between neutral ion pairs and dissociated ions that is often invoked to explain moderately concentrated electrolytes [1] needs to be refined for very highly concentrated electrolytes, where distinguishing between specific pairs of ions loses meaning. We instead propose that local excess charge densities fundamentally determine the length scales of electrostatic screening and show that a "dissociation reaction" between effectively neutral ionic networks and either free ions or higher order correlated charge domains can provide a useful framework for understanding such systems. For example, recent SFA measurements across concentrated aqueous electrolyte solutions [38, 39] establish that the range of electric double-layer interactions increases as the aqueous electrolyte concentrations are increased from 1 to 3 M, but only as long as the electrolyte cation differs from the K^+ ion that is native to mica surfaces. Our results suggest that this trend may be due to the progressive formation of effectively neutral ionic networks involving large numbers of strongly interacting ions. Over the longer term, our results may also prove useful to help explain how electrostatic interactions maintain such a dominant role near the active sites of proteins, ion channels, and similar self-assembling biological systems [2], where local effective salt concentrations can exceed 10 M.

4.5 Materials and methods

The $[C_2mim][NTf_2]$ and $[C_3mim][NTf_2]$ samples were clear and colorless, and NMR, UV-Vis spectroscopy and electrochemical analysis were used to establish that the RTILs were of electrochemical grade purity. After synthesis and drying, Karl Fischer titration was used to ensure that the (trace) water content of the $[C_2mim][NTf_2]$ and $[C_3mim][NTf_2]$ RTILs were under 15 ppm, and the samples were stored under vacuum at all times.

Before each SFA experiment, the $[C_2mim][NTf_2]$ and $[C_3mim][NTf_2]$ samples were dried under vacuum at 373 K for at least 72 h. After drying, a droplet of RTIL (50-100 μL) was immediately injected between mica surfaces in a gas tight SFA under dry nitrogen purge conditions, and the SFA was resealed. All experiments were performed in the presence of a reservoir of the desiccant phosphorous pentoxide (P_2O_5). Each experiment lasted between 24 and 72 hours, and the P_2O_5 reservoirs were found to be unsaturated after each experiment.

The temperature was monitored during each experiment via a thermistor with a 0.2 °C tolerance. The thermal expansion of mica was accounted for by calibrating the mica thermal expansion in the absence of RTIL samples. The mica thermal expansion coefficient was found to be 1.5×10^{-5} C^{-1}, in agreement with literature values.

4.6 References

1. Atkins P., de Paula J. *Physical Chemistry* (Oxford Univ Press, Oxford, UK), 7th Ed, pp 252–289 (2009).
2. Eisenberg B. Interacting ions in biophysics: real is not ideal. *Biophys J* **104** (9), 1849–1866 (2013).
3. Simon P., Gogotsi Y. Materials for electrochemical capacitors. *Nature Materials* **7,** 845–854 (2008).

4. Alias N., Mohamad A. A. Advances of aqueous rechargeable lithium-ion battery: a review. *J Power Sources* **274,** 237–251 (2015).
5. Fedorov M. V., Kornyshev A. A. Ionic liquids at electrified interfaces. *Chem Rev* **114,** 2978–3036 (2014).
6. Welton T. Room-temperature ionic liquids. Solvents for synthesis and catalysis. *Chem Rev* **99,** 2071–2083 (1999).
7. Antonietti M., Kuang D., Smarsly B., Zhou Y. Ionic liquids for the convenient synthesis of functional nanoparticles and other inorganic nanostructures. *Angew Chem Int Ed* **43,** 4988–4992 (2004).
8. Galiński M., Lewandowski A., Stepniak I. Ionic liquids as electrolytes. *Electrochim Acta* **51,** 5567–5580 (2006).
9. Armand M., Endres F., MacFarlane D. R., Ohno H., Scrosati B. Ionic liquid materials for the electrochemical challenges of the future. *Nature Materials* **8,** 621–629 (2009).
10. Ye C., Liu W., Chen Y., Yu L. Room-temperature ionic liquids: a novel versatile lubricant. *Chem Commun* 2244–2245 (2001).
11. Lee A. A., Vella D., Perkin S., Goriely A. Are room-temperature ionic liquids dilute electrolytes? *J Phys Chem Lett* **6,** 159–163 (2015).
12. Kornyshev A. A. Double-layer in ionic liquids: paradigm change? *J Phys Chem B* **111,** 5545–5557 (2007).
13. Bazant M. Z., Storey B. D., Kornyshev A. A. Double layer in ionic liquids: overscreening versus crowding. *Phys Rev Lett* **046102** (2014).
14. Wu J., Jiang T., Jiang D., Jin Z., Henderson D. A classical density functional theory for interfacial layering of ionic liquids. *Soft Matter* **7,** 11222–11231 (2011).

15. Heyes D. M., Clarke J. H. R. Computer simulation of molten-salt interphases. *J Chem Soc Faraday Trans 2* **77,** 1089–1100 (1981).
16. Merlet C., Salanne M., Rotenberg B., Madden P. A. Imidazolium ionic liquid interfaces with vapor and graphite: interfacial tension and capacitance from coarse-grained molecular simulations. *J Phys Chem C* **115,** 16613–16618 (2011).
17. Zhou H. et al. Nanoscale perturbations of room temperature ionic liquid structure at charged and uncharged interfaces. *ACS Nano* **6** (11), 9818–9827 (2012).
18. Lynden-Bell R. M., Frolov A. I., Fedorov M. V. Electrode screening by ionic liquids. *Phys Chem Chem Phys* **14,** 2693–2701 (2012).
19. Yochelis A. Spatial structure of electrical diffuse layers in highly concentrated electrolytes: a modified Poisson-Nernst-Planck approach. *J Phys Chem C* **118,** 5716–5724 (2014).
20. Mezger M. et al. Molecular layering of fluorinated ionic liquids at a charged sapphire (0001) surface. *Science* **322,** 424–428 (2008).
21. Horn R. G., Evans D. F., Ninham B. W. Double-layer and solvation forces measured in a molten salt and its mixtures with water. *J Phys Chem* **92,** 3531–3537 (1988).
22. Atkin R. et al. An *in situ* STM/AFM and impedance spectroscopy study of extremely pure 1-butyl-1-methylpyrrolidinium tris(pentafluoroethyl)trifluorophosphate/Au(111) interface: potential dependent solvation layers and the herringbone reconstruction. *Phys Chem Chem Phys* **13,** 6849–6857 (2011).
23. Perkin S. et al. Self-assembly in the electrical double layer of ionic liquids. *Chem Commun* **47,** 6572–6574 (2011).

24. Gebbie M. A. et al. Ionic liquids behave as dilute electrolyte solutions. *Proc Nat Acad Sci USA* **110** (24), 9674–9679 (2013).

25. Espinosa-Marzal R. M., Arcifa A., Rossi A., Spencer N. D. Microslips to "avalanches" in confined, molecular layers of ionic liquids. *J Phys Chem Lett* **5,** 179–184 (2014).

26. Israelachvili J. N. et al. Recent advances in the surface forces apparatus (SFA) technique. *Rep Prog Phys* **73,** 036601 (2010).

27. Zhou Q., Fitzgerald K., Boyle P. D., Henderson W. A. Phase behavior and crystalline phases of ionic liquid-lithium salt mixtures with 1-alkyl-3-methylimidazolium salts. *Chem Mater* **22,** 1203–1208 (2010).

28. Parsegian V. A., Gingell D. On the electrostatic interaction across a salt solution between two bodies bearing unequal charges. *Biophys J* **12,** 1192–1204 (1972).

29. Kjellander R., Mitchell D. J. Dressed ion theory for electric double layer structure and interactions; an exact analysis. *Molecular Phys* **91** (2), 173–188 (1997).

30. Weingärtner H. Understanding ionic liquids at the molecular level: facts, problems, and controversies. *Angew Chem Int Ed* **47,** 654–670 (2008).

31. Hardacre C., Holbrey J. D., Nieuwenhuyzen M., Youngs T. G. A. Structure and solvation in ionic liquids. *Acc Chem Res* **40,** 1146–1155 (2007).

32. Atkin R., Warr G. The smallest amphiphiles: nanostructure in protic room temperature ionic liquids with short alkyl groups. *J Phys Chem B Lett* **112,** 4164–4166 (2008).

33. Tsuzuki S., Tokuda H., Hayamizu K., Watanabe M. Magnitude and directionality of interaction in ion pairs of ionic liquids: relationship with ionic conductivity. *J Phys Chem B* **109,** 16474–16481 (2005).

34. Todorova M., Neugebauer J. Extending the concept of defect chemistry from semiconductor physics to electrochemistry. *Phys Rev Applied* **1,** 014001 (2014).

35. Elbourne A., Voïtchovsky K., Warr G. G., Atkin R. Ion structure controls ionic liquid near-surface and interfacial nanostructure. *Chem Sci* **6,** 527–536 (2015).

36. Lui M. Y., Crowhurst L., Hallett J. P., Hunt P. A., Niedermeyer H., Welton T. Salts dissolved in salts: ionic liquid mixtures. *Chem Sci* **2,** 1491–1496 (2011).

37. Lockett V., Horne M., Sedev R., Rodopoulos T., and Ralston J. Differential capacitance of the double layer at the electrode/ionic liquids interface. *Phys Chem Chem Phys* **12,** 12499–12512 (2010).

38. Espinosa-Marzal R. M., Drobek T., Balmer T., Heuberger M. P. Hydrated-ion ordering in electrical double layers. *Phys Chem Chem Phys* **14,** 6085–6093 (2012).

39. Baimpos T., Shrestha B. R., Raman S., Valtiner M. Effect of interfacial ion structuring on range and magnitude of electric double layer, hydration, and adhesive interactions between mica surfaces in 0.05-3 M Li^+ and Cs^+ electrolyte solutions. *Langmuir* **30,** 4322–4332 (2014).

40. Christenson H. K. Experimental measurements of solvation forces in nonpolar liquids. *J Chem Phys* **78** (11), 6906–6913 (1983).

41. Israelachvili J. N., Pashley R. M. Molecular layering of water at surfaces and origin of repulsive hydration forces. *Nature* **306** (17), 249–250 (1983).

42. Horn R. G., Israeleachvili J. N. Direct measurement of structural forces between two surfaces in a nonpolar liquid. *J Chem Phys* **75** (3), 1400–1411 (1981).

5 Bridging adhesion of mussel-inspired peptides: role of charge, chain length, and surface type

Reprinted with permission from Wei W., Yu J., Gebbie M. A., Tan Y., Martinez-Rodriguez N. R., Isrealachvili, J. N., Waite J. H. *Langmuir* **31** (3), 1105-1112 (2015).

5.1 Abstract

The 3,4-dihydroxyphenylalanine (Dopa)-containing proteins of marine mussels provide attractive design paradigms for engineering synthetic polymers that can serve as high performance wet adhesives and coatings. Although the role of Dopa in promoting adhesion between mussels and various substrates has been carefully studied, the context by which Dopa mediates a bridging or nonbridging macromolecular adhesion to surfaces is not understood. The distinction is an important one both for a mechanistic appreciation of bio-adhesion and for an intelligent translation of bioadhesive concepts to engineered systems. On the basis of mussel foot protein-5 (Mfp-5; length 75 res), we designed three short, simplified peptides (15–17 res) and one relatively long peptide (30 res) into which Dopa was enzymatically incorporated. Peptide adhesion was tested using a surface forces apparatus. Our results show that the short peptides are capable of weak bridging adhesion between two mica surfaces, but this adhesion contrasts with that of full length Mfp-5, in that (1) while still dependent on Dopa, electrostatic contributions are much more prominent, and (2) whereas Dopa surface density remains similar in both, peptide adhesion is an order of magnitude weaker (adhesion energy $E_{ad} \sim 0.5$ mJ/m^2) than full length Mfp-5 adhesion. Between two mica surfaces, the magnitude of bridging adhesion was approximately doubled ($E_{ad} \sim 1$ mJ/m^2) upon doubling the peptide length. Notably, the short peptides mediate much stronger adhesion ($E_{ad} \sim 3.0$

mJ/m^2) between mica and gold surfaces, indicating that chain length is less important when different interactions are involved on each of the two surfaces.

5.2 Introduction

Marine mussels and sandcastle worms use a suite of proteins rich in 3,4-dihydroxyphenyl-L-alanine (Dopa) to attach to diverse hard surfaces in the sea [1, 2]. In 2006, an elegant demonstration of a strong (~1 nN) but reversible interaction between a single tethered Dopa and a wet TiO_2 surface raised the possibility that any polymer backbone functionalized with Dopa might be rendered adhesive [3, 4]. For a variety of reasons, this promise has remained elusive [5–9]. For example, a synthetic acrylamide copolymer functionalized with Dopamine achieved less than 70 pN of adhesion per catechol on TiO_2 [10], and most poly(ethylene glycol) constructs with Dopa show adhesion to biological surfaces only following oxidation with periodate [11-14]. To better understand the interplay between the surface activity of Dopa and its associated macromolecular backbone, Lin et al. [6] examined the adhesion to mica of two mussel foot proteins (mfp) with similar Dopa contents using a surface forces apparatus and identified two distinctly different Dopa-mediated adhesive modes, that is, a bridging and a nonbridging adhesive mode (Fig. 5.1). In the first mode, molecules span the gap between two solid surfaces with adhesive interactions on both sides; in the second, molecules confine most of their adhesive interactions to one surface. One protein, mfp-3F, exhibited strong and rapid bridging adhesion between the mica surfaces, whereas the other, mfp-1, bound to one mica surface only with little to no tendency to bridge over to the other side, except under high shear. Only two mussel foot proteins, mfp-3 and mfp-5, exhibit strong bridging adhesion. Not surprisingly, these proteins are localized to the interface between the plaque and the substratum. Of the mussel foot proteins, mfp-5 has the highest Dopa content

(~30 mol %) and achieves an adhesion energy per unit area on mica that approaches the interaction between tethered biotin and avidin [5]. On the basis of the known primary sequence of mfp-5, we explore the following questions here: (1) Do the amino acid sequences flanking Dopa affect bridging adhesion? (2) Do interactions besides those involving Dopa help to mediate the bridging adhesion of mfps [15]? (3) Is bridging adhesion dependent on chain length and surface type?

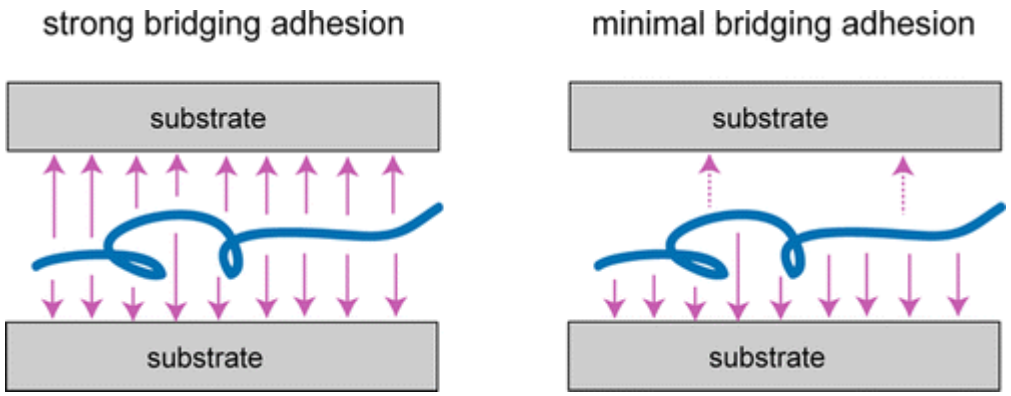

Figure 5.1. Schematic of a molecule interacting with substrates in strong and minimal bridging modes. In the first mode, molecules span the gap between two solid surfaces with energetic interactions on both sides; in the second, molecules confine most of their energetic interactions to one surface. Figure credit: Wei Wei.

To address these questions, three mfp-5-inspired peptides 15–16 residues long were prepared with and without enzymatic modification of tyrosine (Y → Y* denotes Tyr to Dopa): VGSGY*DGY*SDGY*Y*DG (PEP-pI-4), HY*HSGGSY*HGSGY*HG (PEP-pI-6.5), GY*KGKY*Y*GKG KKY*YY*K (PEP-pI-10) (Fig. 5.2). The effect of chain length on bridging adhesion was tested by also preparing a peptide consisting of the PEP-pI-4 sequence repeated twice in a linear fashion (PEP-pI-4-dimer). Our rationale in selecting these particular peptides was that they represent more than half the sequence and most of the sequence diversity of mfp-5 with the smallest possible number of amino acids. The repulsive and

attractive forces of these peptides on mica and gold surfaces were investigated with a surface forces apparatus (SFA) [16].

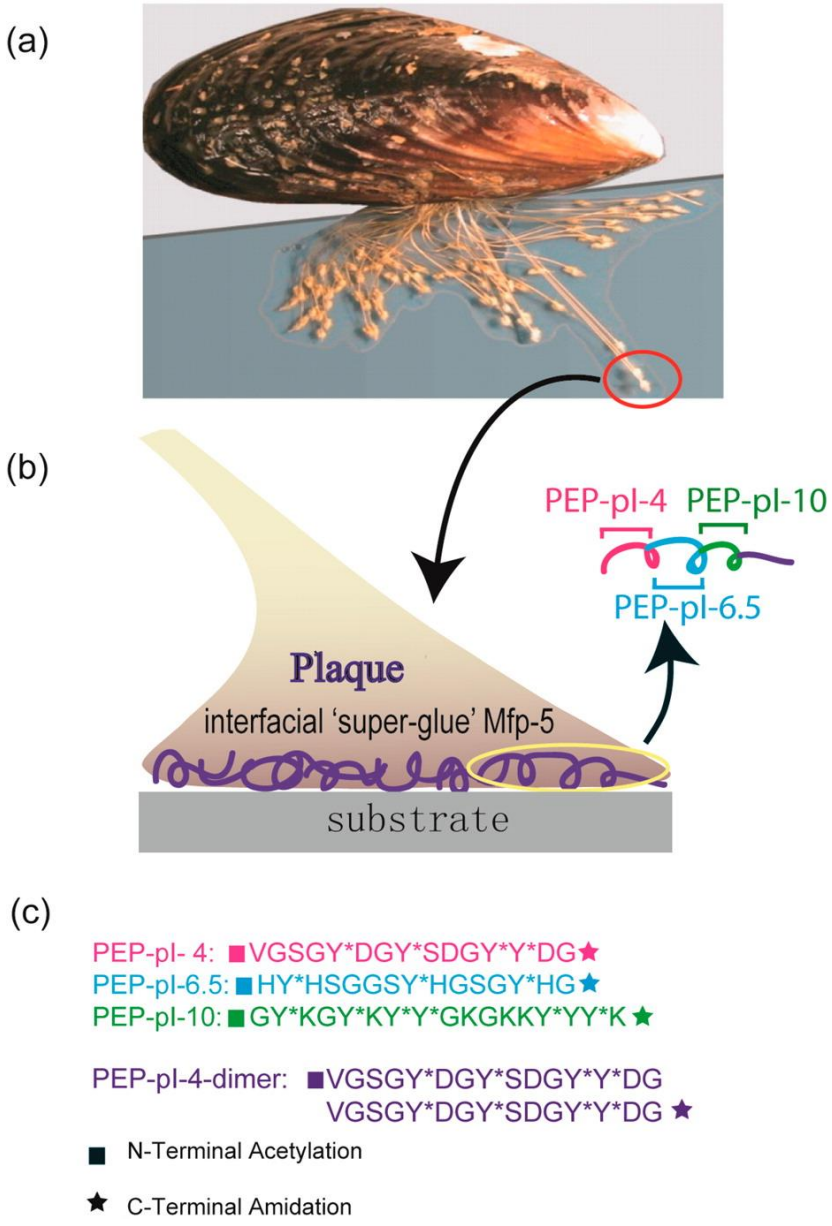

Figure 5.2. Dissecting mussel adhesive protein mfp-5 into distinct peptides. (a) Adult mussel attached to a glass surface by a byssus containing many threads and plaques. (b) Schematic zoom of a plaque, showing the "super glue" mfp-5 at the plaque interface. (c) Three unique sequences with 15–16 amino acid residues, representing about three-fifths of mfp-5 were selected from sections of the parent sequence with different pIs. A dimeric peptide was created by connecting two PEP-pI-4 monomers in tandem. Figure credit: Wei Wei.

5.3 Results

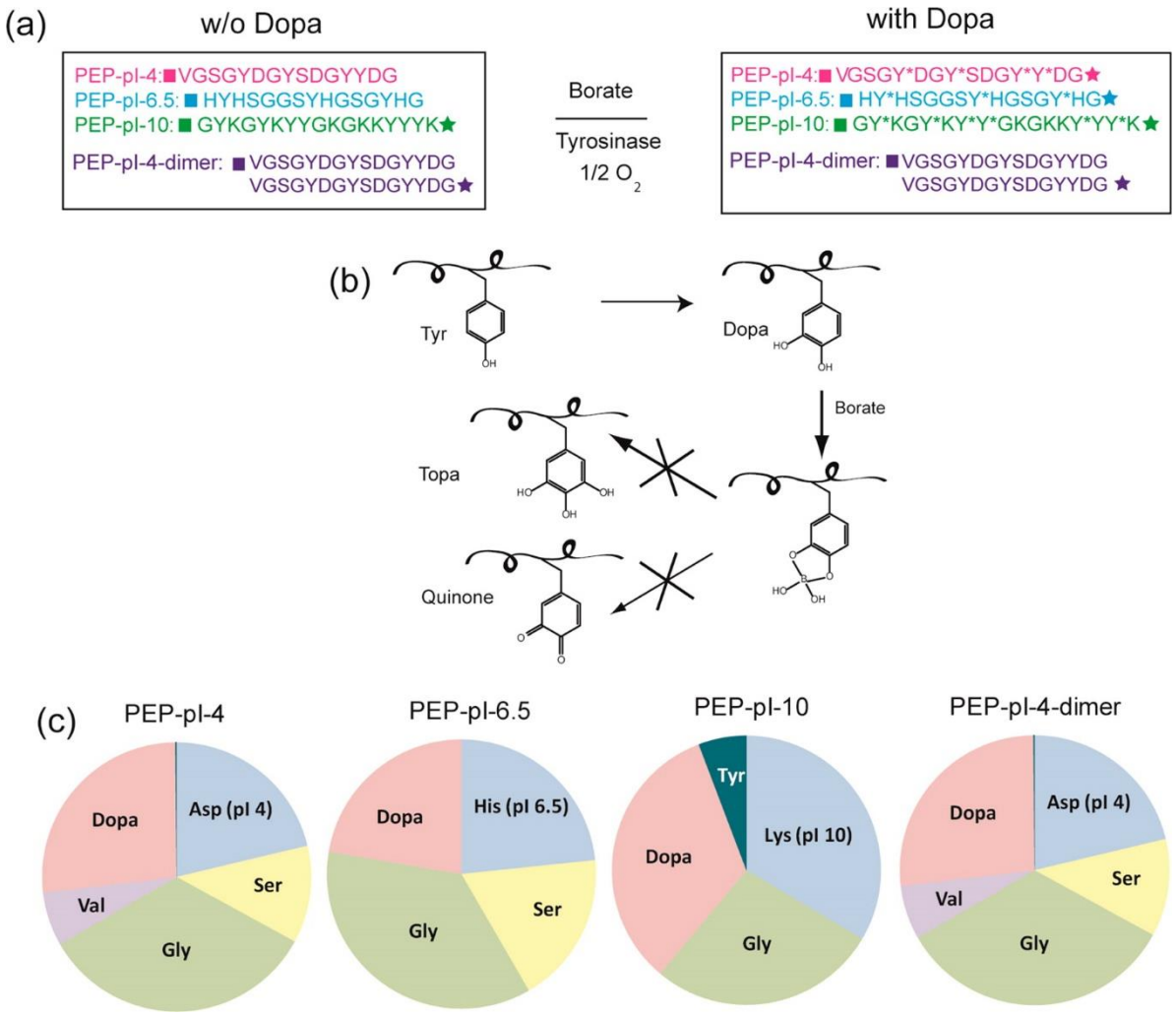

Figure 5.3. Preparation of synthetic mfp-5 inspired peptides. (a) Tyr residues in the three different peptides were enzymatically hydroxylated to Dopa. However, (b) mushroom tyrosinase action is not limited to o-hydroxylation of Tyr but further converts Dopa to Dopa quinone or Topa. To avoid these products, borate was added to capture Dopa by formation of a reversible borate–Dopa chelate complex. (c) Pie chart of amino acid composition of each modified peptide after enzymatic conversion and purification. Figure credit: Wei Wei.

5.3.1 Peptide modification

Mushroom tyrosinase is known to *o*-hydroxylate peptidyl Tyr to Dopa (Fig. 5.3b) and was thus used for this purpose in the peptides [17, 18]. The conversion by tyrosinase requires

safeguards to minimize the formation of undesirable side products such as 3,4,5-trihydroxyphenylalanine (Topa) and Dopaquinone (Fig. 5.3b) [17]. By reversibly capturing Dopa immediately after it has formed, borate significantly improves Dopa yield and decreases side-reactions. After stopping the reaction, modified peptides were separated by reverse phase HPLC, which typically eluted three types of modified peptides, i.e., those that were (a) partially modified (some unmodified Tyr residues remain), (b) completely modified (every Tyr residue is modified), or (c) hypermodified (one or more Tyr residues were converted to Topa) peptides. Electrospray ionization mass spectrometry (ESI) and matrix assisted laser desorption ionization (MALDI) with time-of-flight (TOF) were used to measure the peptide masses in the eluting fractions (Fig. 5.3c). Those fractions with masses matching the calculated mass of completely modified (type b) peptides were pooled for amino acid analysis and sequencing by tandem MS. Amino acid analysis results demonstrate that the compositions of pure modified PEP-pI-4, PEP-pI-6.5, and PEP-pI-4-dimer are consistent with calculated masses: only traces of Tyr remained, and no Topa was detectable. For PEP-pI-10, there is one Tyr that persistently eludes conversion to Dopa: this is Y-14, the central member in the Y-triad. Contact between tyrosinase and Y-14 is presumably impeded by the bulky borate groups on Y*-13 and Y*-15 during the modification.

5.3.2 Bridging adhesion of short peptides between two mica surfaces

Bridging adhesion was measured in the surface forces apparatus (SFA) using an asymmetric configuration; that is, a monolayer of peptides (diameter of hydration ∼2–3 nm) was adsorbed to one mica surface which was then brought into contact with the clean surface, compressed, and separated. Modified peptides PEP-pI-4, PEP-pI-6.5, and PEP-pI-10 all adhered to mica surfaces, with the strongest adhesion force, −4 mN/m (corresponding to a

work of adhesion of 0.64 mJ/m^2), associated with PEP-pI-10. PEP-pI-6.5, although having the lowest Dopa content (only 3 Dopa out of 15 residues), exhibited an intermediate adhesion force of −3.0 mN/m, and the weakest adhesion force (−2.6 mJ/m) was observed for PEP-pI-4 (Fig. 5.4a). These work of adhesion values are notable in being more than an order of magnitude less than full-length mfp-5, even though each peptide represents approximately a fifth of the native sequence. The most likely explanation for this vastly decreased adhesion relative to the native sequence is that the shortened 15–17 residue peptide chains have a much smaller probability of adsorbing in configurations where “loops” or “tails” of the peptides adsorbed onto one mica surface are of sufficient length to make a bridging contact with the opposing mica surface. As a result, most of the short peptides end up interacting intimately with one mica surface, and with few remaining groups available for intimate contact with the other surface, they rely on longer range Coulombic attractions, e.g., positive Lys or His to negative siloxyl groups, for adhesive bridging (Fig. 5.1).

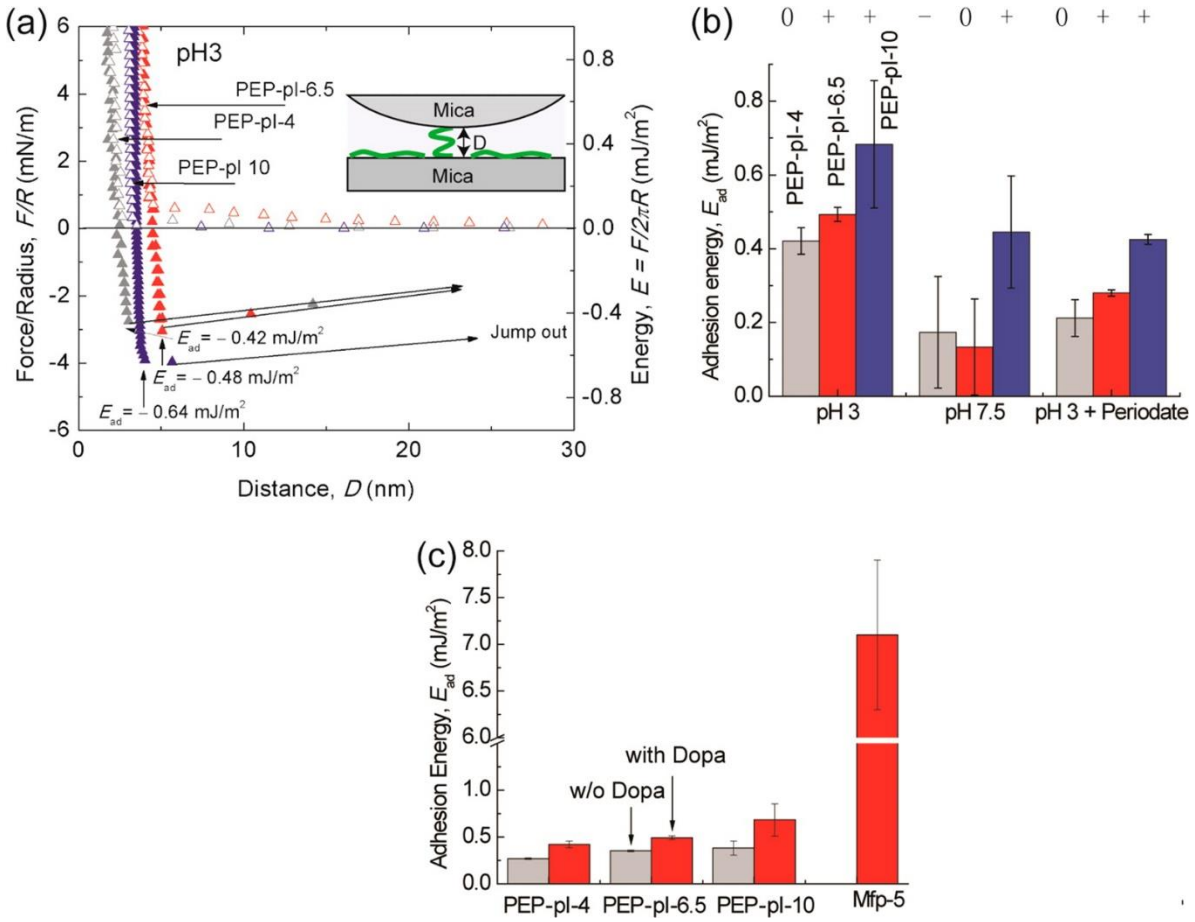

Figure 5.4. Adhesion to mica by mfp-5-derived peptides with and without Dopa. (a) Force–distance profiles of three short peptides in asymmetric configuration on mica surfaces. (b) Summary of adhesion energy of three short peptides measured in pH 3, pH 7.5, and pH 3 following periodate oxidation. '0", "+", and "–" represent respectively the neutral, positive, and negative charge the peptides carry at each condition. (c) Comparison of the adhesion energy of three short peptides with and without tyrosinase modification and mfp-5. The adhesion energies of three short peptides shown in (b) and (c) are averaged from between 6 and 12 repetitive force runs from two different experiments at each treatment. Mfp-5 data are from Ref. 8. Figure credit: Jing Yu.

Consistent with previous work, the results confirm that Dopa plays an essential role in the adhesion of each of the peptides to mica surfaces. All three peptides adhered most strongly to mica surfaces at pH 3 where Dopa is stable, and increasing the solution pH to 7.5, where much of the Dopa is quickly oxidized to the nonadhesive quinone form (Fig. 5.3), significantly

reduced the measured adhesion: the work of adhesion dropped by 80%, 60%, and 35% for PEP-pI-6.5, PEP-pI-4, and PEP-pI-10, respectively, at pH 7.5 (Fig. 5.4b). Previous tests on mussel proteins [5, 9] have shown that Dopa undergoes auto-oxidation at pH 7.5, leading to diminished mfp adhesion. Given their derivation from mfp-5 sequences, the Dopa-containing peptides should be prone to similar oxidation tendencies. Notably, adhesion between two mica surfaces is never eliminated under Dopa oxidizing conditions, even for PEP-pI-4 at pH 7.5, where both the peptide and the mica surface are negatively charged. In addition to this residual adhesion, Dopa oxidation alone also fails to provide an explanation for why the pH affects the three short peptides so differently.

In addition to issues associated with Dopa auto-oxidation at alkaline pH, changes in peptide adhesion also reflect changing electrostatic interactions due to the protonation and/or deprotonation of amino acids and surface siloxyl groups [19]. Increasing pH significantly changes the charge densities (or the overall charge) in the three short peptides. At pH 3, PEP-pI-6.5 and PEP-pI-10 are both positively charged due to the histidine and lysine residues, respectively, so both can favorably interact with the negatively charged mica surface through attractive electrostatic interactions [20]. Increasing the solution pH to 7.5 greatly reduces the positive charges in PEP-pI-6.5; therefore, PEP-pI-6.5 loses both the hydrogen-bonding ability of Dopa to mica surfaces (due to oxidation) and the attractive electrostatic interactions offered by positive amino acid residues (by histidine deprotonation), which results in the largest decrease in terms of the percentage of the adhesion force (75% decrease). In comparison, the sign and density of the charges in PEP-pI-10 remain unchanged at pH 7.5, enabling PEP-pI-10 to maintain interactions between two mica surfaces, despite depletion of Dopa by oxidation (35% decrease of adhesion).

Notably, PEP-pI-4 maintains high bridging adhesion between mica surfaces upon increasing the pH from 3 to 7.5, which would not be expected with both Dopa oxidation and carboxylate formation in PEP-pI-4, resulting in electrostatic repulsion between PEP-pI-4 and mica. The magnitude of the PEP-pI-4 adhesion only fell by 60%. One plausible explanation for this apparent anomaly is that interfacial proton concentration is rarely the same as that of the bulk [21] and that a strongly acidic interface such as that formed between mica and PEP-pI-4 can shield interfacial Dopa from the oxidation expected in solution at pH 7.5. Thus, the bidendate binding of intact Dopa would counteract the repulsion by the acidic groups.

The contribution of electrostatic interactions relative to H-bonding was explored by injecting periodate, an artificial oxidant, into the solution between two mica surfaces at pH 3: after periodate injection, all three peptides exhibited reductions in the measured attractive forces. Further, PEP-pI-6.5 and PEP-pI-4 exhibited higher adhesions at pH 3 with periodate than were measured at pH 7.5. The work of adhesion measured for PEP-pI-6.5 at pH 3 in the absence of Dopa residues is 0.28 mJ/m^2, almost 3 times the value measured at pH 7.5 (0.1 mJ/m^2). The work of adhesion for periodate-treated PEP-pI-4 was measured to be about twice as much as that at pH 7.5. Both of these observations implicate the involvement of electrostatic interactions in the binding of peptides to mica surfaces (Fig. 5.4b).

To further resolve the relative contributions of charged residues and Dopa to the adhesion of three short peptides, SFA tests were performed on the unmodified peptides (without converting tyrosines to Dopa). The work of adhesion of the three unmodified peptides to mica surfaces ranged from 0.27 to 0.35 mJ/m^2 (Fig. 5.4c), with trends similar to those seen with Dopa containing peptides, that is, PEP-pI-4 < PEP-pI-6.5 < PEP-pI-10, which come from electrostatic interactions as well as multiple Tyr-mediated monodentate H-bonds. Tyrosine

conversion to Dopa as much as doubled the adhesion energies on the same surface, which further confirms the importance of Dopa for the bridging adhesion of all the peptides. After oxidizing the Dopa group in the peptides by periodate, the adhesion energies of three modified peptides dropped to values approaching the unmodified peptides, again indicating the effect of enzymatic modification (Fig. 5.5a). No change of adhesion energy was observed for unmodified PEP-pI-10 (Fig. 5.5b).

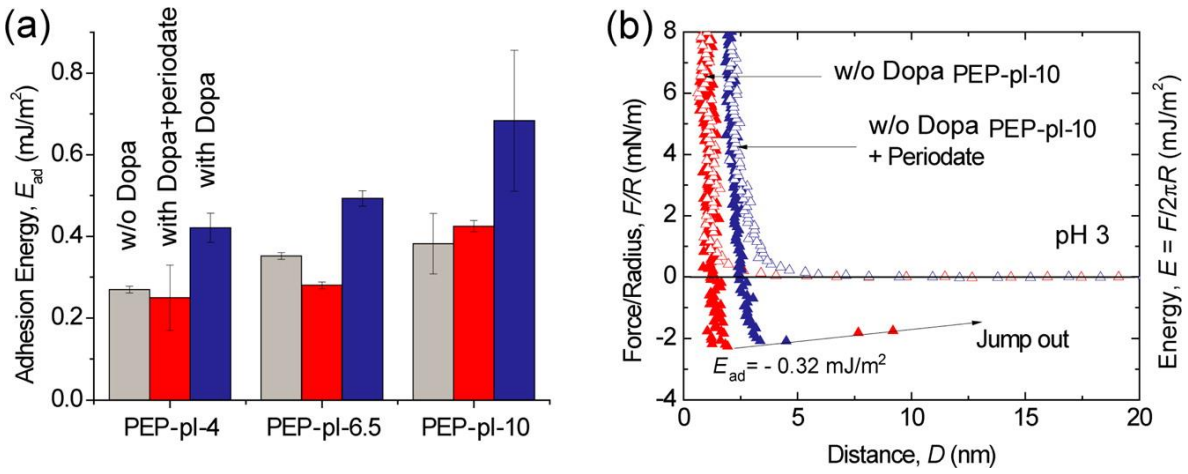

Figure 5.5. Effect of periodate oxidation on peptide adhesion. (a) Adhesion of three short peptides after periodate oxidation resembles the adhesion energy of three unmodified peptides. The adhesion energies are averaged from the values of 6–12 repeating force runs under each condition. (b) Force–distance curves of PEP-pI-10 before and after adding periodate but keeping the pH unchanged (pH = 3). Adding periodate did not alter the adhesion force of unmodified PEP-pI-10, but increased the thickness slightly. Figure credit: Jing Yu.

5.3.3 Bridging adhesion of PEP-PI-4-Dimer between mica surfaces

To evaluate how peptide length affects adhesion and to provide a better functional synthetic model system for bridging adhesion on mica, the PEP-pI-4-dimer sequence was subjected to evaluation by SFA. Increasing chain length should enhance the formation of loops and tails in the polymer chain. As π-cation interactions between aromatic and cationic residues in the peptides can complicate their conformation [22] as well as self-association [23], the

PEP-pI-4 sequence was chosen for the dimer study as the only peptide sequence without (pH-dependent) positively charged residues. The adhesive properties of this peptide dimer were characterized before and after mushroom tyrosinase modification by depositing the modified and unmodified peptide dimers onto a single freshly cleaved mica surface and then measuring the adhesive bridging of this peptide dimer to another mica surface. At pH 3, PEP-pI-4-dimer promotes adhesion between the mica surfaces of ~6 mN/m (corresponding to a work of adhesion of ~1 mJ/m^2) (Fig. 5.6), which is approximately twice the adhesion exhibited by the PEP-pI-4 monomer sequence. Given that the pep-pI-4 monomer and dimer were deposited at the same solution mass fractions (as opposed to molar concentrations), surface Dopa amounts in two cases should be roughly equal. Higher adhesion of dimer should be due to its higher tendency of forming "loops" and "tails" which are favorable for bridging. As in the case of the short peptides, increasing pH to 7.5 decreased adhesion of PEP-pI-4-dimer to mica by approximately 65% to a value of about 0.35 mJ/m^2 due to Dopa oxidation. Since both the PEP-pI-4-dimer sequence and the mica surface should be negatively charged at this pH, the presence of residual adhesion is unexpected. Our explanation for this anomaly remains the same "interfacial pH" explanation that was invoked for the PEP-pI-4 monomer. The adhesion of unmodified PEP-pI-4-dimer (without Dopa) on mica at pH 3 was measured to be 0.4 mJ/m^2 (Fig. 5.7), which is approximately half the adhesive energy measured for the Dopa-containing dimer. Interestingly, the adhesion measured for the unmodified PEP-pI-4-dimer was seen to be independent of pH for the pH 3 and 7.5 conditions tested in the current study (Fig. 5.7). Tyrosine residues do not undergo autoxidation or deprotonation at pH 7.5 and may interact favorably with muscovite mica surfaces through either monodentate hydrogen bonds

(analogous to the bidentate bonding exhibited by Dopa) or cation-π interactions with the K^+ ions present at mica surfaces.

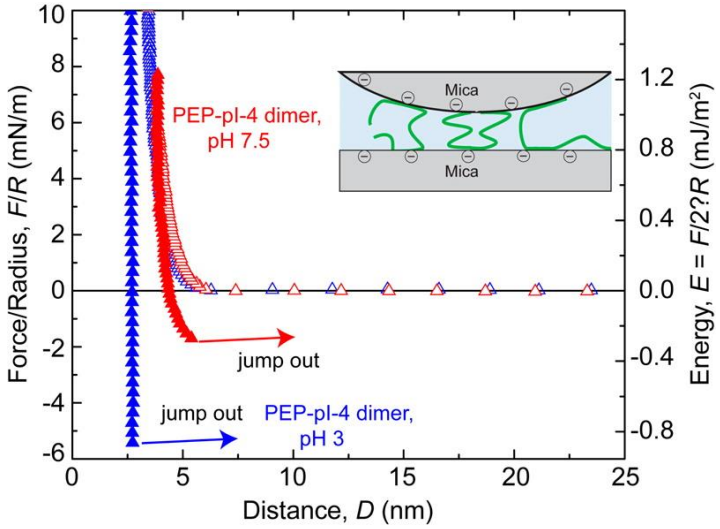

Figure 5.6. Force profiles of the Dopa-modified PEP-pI-4-dimer on mica at pH 3 and 7.5. Adhesion is approximately double that of the corresponding monomer in Figure 2 and shows similar losses due to auto-oxidation at pH 7.5.

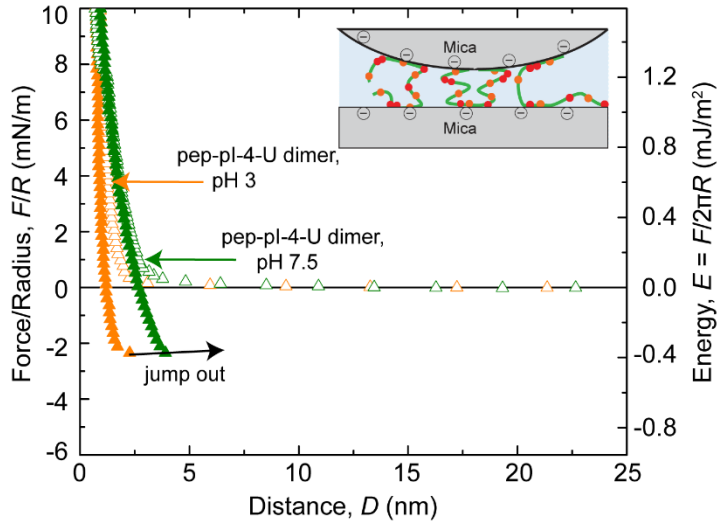

Figure 5.7. Force profiles of unmodified PEP-pI-4-dimer without Dopa on mica surfaces at pH 3 and pH 7.5.

5.3.4 Bridging adhesion of PEP-PI-10 between mica and gold surfaces

To test for bridging adhesion between dissimilar surfaces, SFA measurements were performed where one of the mica surfaces was replaced with a smooth gold surface (0.5 nm RMS roughness). PEP-pI-10 mediated the strongest adhesion between two mica surfaces (Fig. 5.4a) and hence was selected for adhesive bridging between asymmetric mica/gold surfaces. PEP-pI-10 was first deposited onto mica where many of the Dopa groups form strong, specific interactions with the mica substrate, and this film was then compressed against an opposing gold surface at pH 3 (Fig. 5.8). The adhesion of PEP-pI-10 in this gold/peptide/mica geometry (~3 mJ/m^2) was much stronger than the adhesion measured in the mica/peptide/mica geometry. This strong adhesion is attributed to the high surface energy of gold, which has strong so-called "soft epitaxial" binding with Dopa, the other amino acid side chains, and backbone amides of protein/peptides [24-28]. As a result, PEP-pI-10 binds gold surfaces, even when most of the Dopa side chains have been recruited to the mica surface during the initial film deposition.

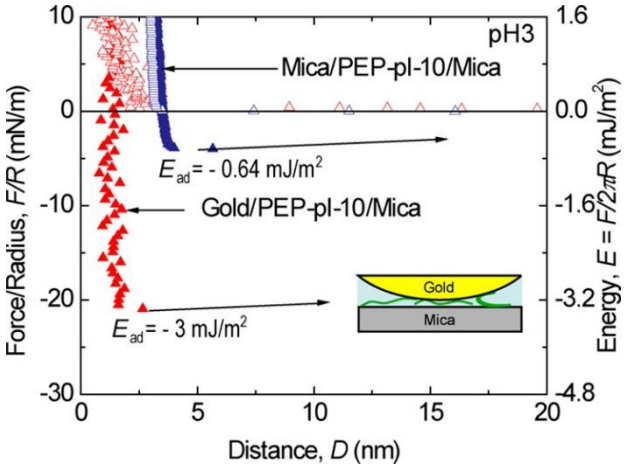

Figure 5.8. Force profiles of PEP-pI-10 coated on a mica surface against a gold surface. PEP-pI-10 showed 5 times stronger adhesion force, compared to the adhesion between two mica surfaces. Figure credit: Jing Yu.

5.4 Discussion

In previous SFA studies of mfp-based adhesion, little attention was given to the electrostatic interactions between mfps and substrates. In this work, however, the range of peptide ionizations enabled a systematic study of electrostatic contributions to adhesion in Dopa-containing systems. These measurements were performed at high salt concentration (0.35 M) that, like seawater, typically reduces the Debye length to ~0.5 nm. Here, we show that electrostatic interactions between mfps and substrates make a significant contribution to bridging adhesion. These results also highlight the importance of electrostatic interactions in highly concentrated electrolyte solutions, which are typically ignored. Electrostatic interactions are advantageous in that they are nonspecific and long range in nature (potentially extending over several nanometers), whereas Dopa-mediated interactions have ångstrom length scales and require complementary target geometry for H-bond or coordination bond formation. As most biological molecules and surfaces are charged, long range electrostatic interactions may serve to guide mussel adhesive proteins and various mussel inspired adhesive polymers toward target binding sites on substrate surfaces, paving the way for Dopa residues to make strong, specific bonds [29, 30].

Another major finding of this study is that increasing peptide length enhances Dopa-mediated bridging adhesion on surfaces. With Dopa residues scattered along the sequence, adhesive proteins or peptides have to be long enough to adopt appropriate conformations on one mica surface that enable the presentation of Dopa containing side chains to the other surface. All three mfp-5-derived short peptides showed adhesion energies that are at least an order of magnitude lower than the adhesion energy of intact mfp-5, about 7.1 mJ/m^2, measured by the SFA [5]. Mfp-5 consists of about 74 amino acid residues, 20 of which are Dopa (~30

mol %). Given their size and flexible extended conformations, mfp-5 molecules are likely to have wormlike structures on the mica surface. The longer protein backbone and many Dopa side chains give mfp-5 molecules an opportunity to bridge two surfaces and to have Dopa residues from the same backbone firmly planted on both sides (Fig. 5.9).

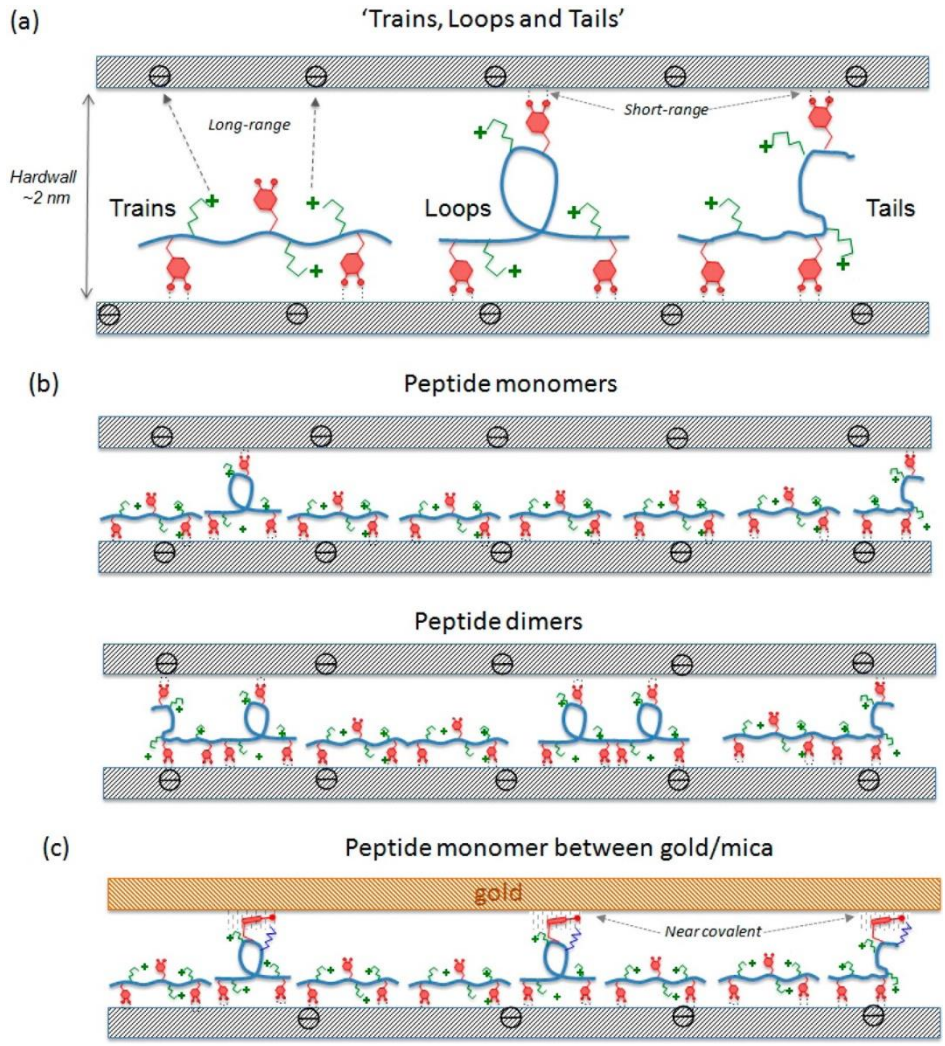

Figure 5.9. Binding models of peptides. (a) Different conformations of peptides on surface: train loop and tail. (b) Peptide monomers and dimers bridging two mica surfaces. (c) Peptide monomers bridging between mica and gold. The red side chains represent Dopa, green side chains represent positive charge (Lys), and blue ones represent side chains of the other amino acids. Figure credit: Wei Wei.

The peptides, in contrast, are much shorter, with between 3 and 5 Dopa groups in their sequence. During the deposition, an entire peptide may stick as a train to one mica surface, leaving few or no "loops" or "tails" with Dopa groups to bridge to the other mica surface. This would result in fewer bridging opportunities (Fig. 5.9). A critical peptide length in adhesion is supported by the SFA results of PEP-pI-4-dimer, which demonstrates that doubling the length of the peptide sequence roughly doubles the adhesive forces. This mechanism is consistent with polymer scaling theory, where, in the simplest picture, the mean-squared radius of a solvated polymer in solution, $\langle r^2 \rangle^{1/2}$, scales as $N^{3/5}$, where N is the number of monomers along a polymer backbone. Thus, doubling the length of a 15–17 residue peptide should be expected to increase $\langle r^2 \rangle^{1/2}$ by a factor of ~1.5, and increasing the length of a 15 residue peptide by a factor of 5 (mfp-5 is a 75-residue protein) should be expected to roughly increase $\langle r^2 \rangle^{1/2}$ by a factor of ~2.63. Both cases demonstrate that increasingly compact and "looped" solution configurations of the proteins and peptides become highly favored with increasing length. DLS (Fig. 5.10) shows pep-pI-4 monomer and dimer have similar hydrodynamic diameter in solution, which indicates dimer has more compact configuration than monomer. Since solution configurations are intimately connected to adsorption configurations in cases where polymers quickly and irreversibly bind to surfaces, we assert that on surfaces the dimer adopts a more compact configuration, too, which results in more "loops" and "tails" structure to stick to the second surface. When a peptide is deposited onto a surface, entropy maximization will be in competition with the chemical free energy reduction change by Dopa/surface binding. With longer peptides, the entropic contribution to the free energy offered by adopting a random structure will win out over the free energy decrease due to chemical binding, which would result in peptides lying flat on surfaces. When

the opposing surface is presented, a flexible random structure is more favorable for the peptide to bridge two surfaces when adhesion depends on forming Dopa mediated interactions on both sides.

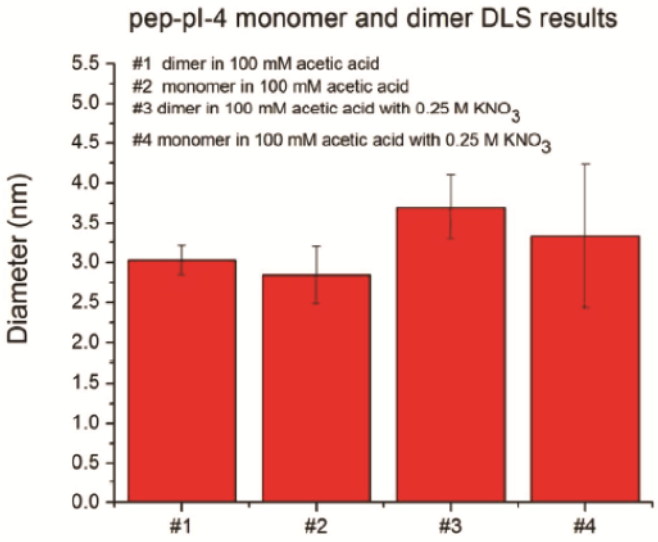

Figure 10. Hydrodynamic diameter of pep-pI-4-monomer and dimer without Dopa in 100 mM acetic acid and 100 mM acetic acid with 250 mM KNO_3, respectively. Figure credit: Wei Wei.

The unevenly distributed Dopa binding of PEP-pI-10 is further suggested by the strong bridging adhesion (~3 mJ/m^2) of PEP-pI-10 in a gold/peptide/mica geometry by measuring the adhesion of a PEP-pI-10 deposited mica surface against an opposing gold surface in pH 3 buffer (Fig. 8). On the peptide/gold interface, PEP-pI-10 interacts with the gold surface through "soft epitaxial" binding [24]; adding Dopa functions as a "surface anchor" [25]. Thus, strong adhesion can be promoted between the mica and gold surfaces, even if few Dopa residues are available to interact with the gold surface. Further, assuming that the binding of PEP-pI-10 to mica is the weakest link in the bridge between gold and mica, the adhesion of 3 mJ/m^2 is about 40% of the value of intact mfp-5 on the mica surface.

Mussel adhesive proteins have inspired numerous investigations of Dopa- or catechol-functionalized synthetic materials for various applications including wet adhesives [10, 12, 31-33], antifoulant coatings [34, 35], magnetic imaging agents [36], tissue glues, and pH-sensitive hydrogels. Most of these materials have been designed by a trial-and-error approach after many costly and time-consuming iterations. We maintain that a systematic understanding of factors that contribute to bridging or coating adhesion in mussels proteins can accelerate the practical implementation of important design concepts.

5.5 Summary and outlook

The design and synthesis of mussel-inspired peptides allowed us to investigate the role of electrostatic—especially cationic—contributions to the bridging adhesion of Dopa-containing peptides. Electrostatic effects in the adhesion of mfp-5 were not previously detected, perhaps because of steric constraints imposed by the long native protein backbone. The chain-length-dependent adhesion of PEP-pI-4-dimers and monomers explicitly illustrates the significance of peptide length on promoting adhesion between two surfaces when the adhesion of peptides to each of the surfaces is dominated by Dopa-mediated interactions. Increasing chain length promotes increasingly disordered structures, rather than the flattened conformations where most, if not all, the Dopa-containing side chains are bound to a single surface, and thus promotes interaction with a second approaching surface. In this light, the strong adhesion of mfp-5 might result not only from its long sequence but also to synergistic or cooperative effects between amino acid residues over the whole protein sequence. Given the fact that nature has optimized mussel proteins for adhesion over millions of years, these synergistic effects should not be so surprising. Another important message conveyed by this study is that, in practice, when the second surface (e.g., gold) does not rely on Dopa for bridging adhesion,

relatively short molecules can mediate bridging between different surfaces via different binding mechanisms even though Dopa residues have been mostly occupied by the first surface (e.g., mica). Analysis of adhesion by short mfp-derived peptide sequences provides a simpler way to design better mussel inspired adhesives for complex/heterogeneous surface chemistries and is more cost-effective from the engineering perspective.

5.6 Materials and methods

5.6.1 Peptide modification and purification

The peptides HYHSGGSYHGSGYHG (PEP-pI-6.5), VGSGYDGYSDGYYDG (PEP-pI-4), GYKGKYYGKGKKYYYK (PEP-pI-10), and VGSGYDGYSDGYYDGVGSGYDGYSDGYYDG (PEP-pI-4-dimer) were synthesized by GenScript (Piscataway, NJ) using routine solid-phase synthesis that included N-terminal acetylation and C-terminal amidation and were provided as a desalted solid. Mushroom tyrosinase (3000 U/mg) was from Aldrich-Sigma, and all other reagents were of analytical grade. *Enzymatic modification*: The peptides (1 mg) were dissolved in 1 mL of pH 7.0, 20 mM borate, 0.1 M phosphate-ascorbate buffer, in an Eppendorf microfuge tube. After adding mushroom tyrosinase (0.3 mg), the tube was shaken for 4 h at ambient room temperature and pressure. Each reaction was stopped by adding 40 μL of glacial acetic acid, and the resulting product was subjected to reverse phase HPLC column, eluted with a linear gradient of aqueous acetonitrile. Eluant was monitored continuously at 230 and 280 nm, and 0.33 mL fractions containing peptides were pooled and freeze-dried. Sample purity and hydroxylation were assessed by amino acid analysis and electrospray ionization mass spectrometry. Fractions with pure hydroxylated peptides were dissolved in 0.1 M acetic acid (Sigma-Aldrich) and 0.25 M

potassium nitrate (Sigma-Aldrich) buffer (pH 3) with a peptide concentration of 100 μg/mL and kept in a −80 °C freezer.

5.6.2 Mass spectroscopy

A Micromass QTOF2 tandem mass spectrometer (Waters Corp.) with an electrospray ionization source and matrix assisted laser desorption ionization (MALDI) with time-of-flight mass (TOF) (Bruker Microflex LRF) were used to obtain spectrometry of peptides. For QTOF2-ESI, samples were infused at 10 μL/min via a Harvard Apparatus syringe pump. Capillary voltage was held at 3.5 kV. Source and desolvation temperatures were 80 and 100 °C, respectively. MS/MS experiments were carried out with argon as collision gas and a collision voltage of 10 V. For MALDI-TOF, the N_2 laser (337 nm) fires at 60 Hz. 1–2 μL of sample peptide was spotted onto the gold-plated sample plate and vacuum-dried, on top of which 1 μL of matrix solution (α-cyano-3-hydroxycinnamic acid in aqueous 50% acetonitrile and 0.1% trifluoroacetic acid) was added. External calibrant was peptide calibration standard mixture from Bruker containing seven standard peptides with a mass range between ~1000 and 3500 Da.

5.6.3 Amino acid analysis

The amino acid composition of the hydrolyzed peptides was determined on a Hitachi L8900 amino acid analyzer system with ninhydrin detection. Polypeptides were hydrolyzed in 100 μL of 6 M HCl with 8% phenol in vacuum at 158 °C for 40 min. After being washed with water and methanol, the hydrolyzed products were dissolved in 0.2 M HCl and injected into amino acid analyzer.

5.6.4 Surface forces apparatus

The adhesion of each peptide to mica was then measured by a SFA in a reported configuration. Prior to each experiment, 10 μL of peptide solution was added on top of 1 mica surface, letting the peptide adsorb on mica for 20 min followed by rinsing excessively with the same buffer to remove the nonadsorbed peptide molecules. The adhesion force measured was normalized by the radius of curved disks used in the SFA experiment, typically 2 cm, and further converted into adhesion energy (or work of adhesion) by using the Derjaguin approximation: $E = F/2\pi R$.

5.6.5 Dynamic light scattering

The sizes of pep-pI-4 monomer and dimer in solution (2 mg/mL) in 100 mM acetic acid and 100 mM acetic acid containing 0.25 M KNO_3 were obtained using the Malvern Nano ZS, which is calibrated regularly using Malvern Zeta Potential Transfer standard (P/N DTS1230, batch number 380901).

5.7 References

1. Stewart R. J., Weaver J. C., Morse D., Waite J. H. The tube cement of Phragmatopoma californica: a solid foam. *J. Exp. Biol.* **207,** 4727– 4734 (2004).
2. Lee B. P., Messersmith P. B., Israelachvili J. N., Waite J. H. Mussel-inspired adhesives and coatings. *Annu. Rev. Mater. Res.* **41,** 99– 132 (2011).
3. Anderson T. H., Yu J., Estrada A., Hammer M. U., Waite J. H., Israelachvili J. N. The contribution of DOPA to substrate-peptide adhesion and internal cohesion of mussel-inspired synthetic peptide films. *Adv. Funct. Mater.* **20,** 4196– 4205 (2010).

4. Lee H., Scherer N. F., Messersmith P. B. Single-molecule mechanics of mussel adhesion. *Proc. Natl. Acad. Sci. U. S. A.* **103,** 12999– 13003 (2006).
5. Danner E. W., Kan Y., Hammer M. U., Israelachvili J. N., Waite, J. H. Adhesion of mussel foot protein Mefp-5 to mica: An underwater superglue. *Biochemistry* **51,** 6511– 6518 (2012).
6. Lin Q., Gourdon D., Sun C. J., Holten-Andersen N., Anderson T. H., Waite J. H., Israelachvili J. N. Adhesion mechanisms of the mussel foot proteins mfp-1 and mfp-3. *Proc. Natl. Acad. Sci. U. S. A.* **104,** 3782– 3786 (2007).
7. Lu Q., Hwang D. S., Liu Y., Zeng H. Molecular interactions of mussel protective coating protein, mcfp-1, from Mytilus californianus. *Biomaterials* **33,** 1903– 1911 (2012).
8. Qin Z., Buehler M. Molecular mechanics of dihydroxyphenylalanine at a silica interface. *Appl. Phys. Lett.* **101,** 083702 (2012).
9. Yu J., Wei W., Danner E., Ashley R. K., Israelachvili J. N., Waite J. H. Mussel protein adhesion depends on interprotein thiol-mediated redox modulation. *Nat. Chem. Biol.* **7,** 588– 590 (2011).
10. Wang J. J., Tahir M. N., Kappl M., Tremel W., Metz N., Barz M., Theato P., Butt H. J. Influence of binding-site density in wet bioadhesion. *Adv. Mater.* **20,** 3872 (2008).
11. Matos-Perez C. R., White J. D., Wilker J. J. Polymer composition and substrate influences on the adhesive bonding of a biomimetic, cross-linking polymer. *J. Am. Chem. Soc.* **134,** 9498– 9505 (2012).
12. You I., Kang S. M., Lee S., Cho Y. O., Kim J. B., Lee S. B., Nam Y. S., Lee H. Polydopamine microfluidic system toward a two-dimensional, gravity-driven mixing device. *Angew. Chem., Int. Ed.* **51,** 6126– 6130 (2012).

13. Mann L. K., Papanna R., Moise K. J., Byrd R. H., Popek E. J., Kaur S., Tseng S. C. G., Stewart R. J. Fetal membrane patch and biomimetic adhesive coacervates as a sealant for fetoscopic defects. *Acta Biomater.* **8,** 2160– 2165 (2012).
14. Brubaker C. E., Messersmith P. B. Enzymatically degradable mussel-inspired adhesive hydrogel. *Biomacromolecules* **12,** 4326– 4334 (2011).
15. Krivosheeva O., Dedinaite A., Claesson P. M. Adsorption of Mefp-1: Influence of pH on adsorption kinetics and adsorbed amount. *J. Colloid Interface Sci.* **379,** 107–113 (2012).
16. Israelachvili J., Min Y., Akbulut M., Alig A., Carver G., Greene W., Kristiansen K., Me yer E., Pesika N., Rosenberg K., Zeng H. Recent advances in the surface forces apparatus (SFA) technique. *Rep. Prog. Phys.* **73** (2010).
17. Taylor S. W. Chemoenzymatic synthesis of peptidyl 3,4-dihydroxyphenylalanine for structure-activity relationships in marine invertebrate polypeptides. *Anal. Biochem.* **302,** 70–74 (2002).
18. Wilke P., Borner H. G. Mussel-glue derived peptide-polymer conjugates to realize enzyme-activated antifouling coatings. *ACS Macro Lett.* **1,** 871– 875 (2012).
19. Patwardhan S. V. E., Berry R. J., Jones S. E., Naik R. R., Deschaume O., Heinz H., Perry C. C. Chemistry of aqueous silica nanoparticle surfaces and the mechanism of selective peptide adsorption. *J. Am. Chem. Soc.* **134,** 6244– 6256 (2012).
20. Israelachvili, J. N. *Intermolecular and Surface Forces*, 3rd ed.; Acad. Press: Burlington, MA, **2011**.
21. Hartvig R. A., van de Weert M., Ostergaard J., Jorgensen L., Jensen H. Protein adsorption at charged surfaces: The role of electrostatic interactions and interfacial charge regulation. *Langmuir* **27,** 2634– 2643 (2011).

22. Khandelia H., Kaznessis Y. N. Cation-pi interactions stabilize the structure of the antimicrobial peptide indolicidin near membranes: Molecular dynamics simulations. *J. Phys. Chem. B* **111,** 242– 250 (2007).

23. Shi Z. S., Olson C. A., Kallenbach N. R. Cation-pi interaction in model alpha-helical peptides. *J. Am. Chem. Soc.* **124,** 3284– 3291 (2002).

24. Feng J. P., Berry R. J., Farmer B. L., Naikc R. R., Heinz H. Adsorption mechanism of single amino acid and surfactant molecules to Au {111} surfaces in aqueous solution: design rules for metal-binding molecules. *Soft Matter* **7** (5), 2113–2120 (2011).

25. Weinhold M., Soubatch S., Temirov R., Rohlfing M., Jastorff B., Tautz F. S., Doose C. Structure and bonding of the multifunctional amino acid L-DOPA on Au(110). *J. Phys. Chem. B* **110,** 23756– 23769 (2006).

26. Plekan O., Feyer V., Ptasinska S., Tsud N., Prince K. C. Cyclic dipeptide immobilization on Au(111) and Cu(110) surfaces. *Phys. Chem. Chem. Phys.* **16,** 6657–666 (2014).

27. Humblot V., Tejeda A., Landoulsi J., Vallée A., Naitabdi A., Taleb A., Pradier C. M. Walking peptide on Au(110) surface: Origin and nature of interfacial process. *Surf. Sci.***628,** 21– 29 (2014).

28. Heinz H., Farmer B. L., Pandey R. B., Slocik J. M., Patnaik S. S., Pachter R., Naik R. R. Nature of molecular interactions of peptides with gold, palladium, and Pd-Au bimetal surfaces in aqueous solution. *J. Am. Chem. Soc.* **131,** 9704– 9714 (2009).

29. Valtiner M., Donaldson S. H., Gebbie M. A., Israelachvili J. N. Hydrophobic forces, electrostatic steering, and acid-base bridging between atomically smooth self-assembled monolayers and end-functionalized PEGolated lipid bilayers. *J. Am. Chem. Soc.* **134,** 1746– 1753 (2012).

30. Heinz H. The role of chemistry and pH of solid surfaces for specific adsorption of biomolecules in solution—accurate computational models and experiment. *J. Phys.: Condens. Matter* **26,** 244105 (2014).
31. Lee H., Dellatore S. M., Miller W. M., Messersmith P. B. Mussel-inspired surface chemistry for multifunctional coatings. *Science* **318,** 426– 430 (2007).
32. Park K. M., Park K. D. Facile surface immobilization of cell adhesive peptide onto TiO_2 substrate via tyrosinase-catalyzed oxidative reaction. *J. Mater. Chem.* **21,** 15906–15908 (2011).
33. Shafiq Z., Cui J. X., Pastor-Perez L., San Miguel V., Gropeanu R. A., Serrano C., del Campo A. Bioinspired underwater bonding and debonding on demand. *Angew. Chem., Int. Ed.* **51,** 4332– 4335 (2012).
34. Kuang J. H., Messersmith P. B. Universal surface-initiated polymerization of antifouling zwitterionic brushes using a mussel-mimetic peptide initiator. *Langmuir* **28,** 7258–7266 (2012).
35. Dalsin J. L., Hu B. H., Lee B. P., Messersmith P. B. Mussel adhesive protein mimetic polymers for the preparation of nonfouling surfaces. *J. Am. Chem. Soc.* **125,** 4253–4258 (2003).
36. Lee Y. H., Lee H., Kim Y. B., Kim J. Y., Hyeon T., Park H., Messersmith P. B., Park T. G. Bioinspired surface immobilization of hyaluronic acid on monodisperse magnetite nanocrystals for targeted cancer imaging. *Adv. Mater.* **20,** 4154 (2008).

6 Tuning underwater adhesion with cation-π interactions

6.1 Abstract

Cation-π interactions drive the self-assembly and cohesion of many biological molecules, including the adhesive proteins of several marine organisms. While the molecular origin of cation-π bonds in isolated pairs has been extensively studied, the energetics of cation-π driven self-assembly in molecular films remains uncharted. Here, we use nanoscale force measurements to show that the cohesive properties of simple aromatic- and lysine-rich peptides rival that of the strong, reversible, intermolecular cohesion exhibited by marine mussel adhesive proteins. In particular, we show that peptides incorporating the amino acid phenylalanine, a functional group that is conspicuously sparing in the sequences of mussel proteins, exhibit reversible adhesive interactions significantly exceeding that of analogous mussel-mimetic peptides. More broadly, we demonstrate that interfacial confinement fundamentally alters the energetics of cation-π mediated assembly, an insight that should prove relevant for diverse areas, ranging from rationalizing biological assembly to engineering peptide-based biomaterials.

6.2 Introduction

Nature employs a variety of noncovalent interactions to tune the structures and functions of proteins, peptides and other complex biological molecules, with cation-π interactions featuring prominently in biological self-assembly [1–4], molecular recognition [5–7], and molecular cohesion and adhesion [8–10]. In this chapter, we distinguish between cohesive failure, where failure occurs within a glue (peptide) film, and adhesive failure, where failure

occurs at a glue-surface (peptide-surface) interface. These two terms are often used interchangeably in the broader scientific literature, and many adhesives actually fail via cohesive mechanism [11–13]. Cation-π interactions are electrostatic in origin and occur between cations and electron-rich π-orbitals [1, 14, 15]. Particularly strong cation-π binding occurs when cations interact with the delocalized π-orbitals perpendicular to the plane of aromatic rings. While cation-π interactions are much stronger in the gas phase than in condensed phases, cation-π interactions still exceed the strength of hydrogen bonds, and possibly even charge-charge interactions, in aqueous solutions [1, 16].

As a result, cation-π interactions provide an attractive molecular design paradigm for developing molecules that can function as adhesives in underwater environments. Such materials could be used to address a number of substantial engineering challenges, ranging from functioning as biomedical adhesives that can replace damaging screws in surgical applications [17], to providing cohesive binding domains that hold together tissue engineering scaffolds [18]. Despite this technological promise, the relative binding energetics of cation-π interactions at interfaces cannot yet be predicted *a priori*. In fact, much of the current understanding of cation-π binding strengths in condensed phases is either extrapolated from gas phase experiments and calculations [1, 14–16], or inferred from the proximity of aromatic and cationic amino acids in protein crystal structures [2, 3, 6]. Nevertheless, it remains unclear whether these insights are directly applicable to rationalizing cation-π energetics at interfaces.

Notably, cation-π binding at interfaces typically involves the formation of several cation-π binding pairs in close proximity, where the electrostatic repulsion between two closely-spaced (positive) pairs can compromise the favorable free energy gained by forming the two cation-π bonds. The complexation of anions with cation-π pairs could provide the necessary

charge compensation to eliminate this electrostatic repulsion. Indeed, researchers have studied the impact of anions on isolated ternary cation-π-anion binding groups [19–23], but reached the general conclusion that anions induce anti-cooperative three body interactions that reduce the strength of (destabilize) cation-π binding pairs. However, these previous studies did not account for the electrostatic repulsion between closely spaced cation-π binding groups, which we hypothesize is an important general effect at interfaces and in the interiors of folded proteins. As a result, gaining insight into the impact of electrostatic correlations between adjacent cation-π binding pairs is of practical relevance.

In the context of engineered biomaterials, cation- and aromatic-rich sequences are prevalent in the adhesive proteins of several marine organisms, including mussels [17], sandcastle worms [24], and barnacles [25]. Many researchers have sought to translate these protein sequences into synthetic, bio-inspired adhesives by focusing predominantly on the role of the catecholic functional group 3,4-dihydroxyphenylalanine (Dopa) [17, 26–29]. However, Dopa is conspicuously sparing or nonexistent in the highly adhesive proteins of some marine organisms like green mussels [8] and barnacles [25]. Further, Dopa is prevalent in non-adhesive proteins, such as the plaque coating proteins of some marine mussels [17]. These facts imply that the inclusion of Dopa alone is not sufficient to render a molecule with adhesive functionality in underwater environments. More recent studies [29–31] identified a possible synergistic relationship between Dopa and cationic amino acids; yet none of these studies systematically explored how changes to the aromatic molecular structure impacts the strength of cation-π interactions in adhesive films.

In this work, we test the hypothesis that cation-π interactions may provide a broader molecular motif that can be used to rationally imbue peptide-based materials with robust

underwater cohesive binding interactions and pursue fundamental insight into the energetics of interfacial cation-π interactions. To test this proposal, we designed a series of adhesive lysine- and aromatic-rich peptides and used nanoscale force measurements to quantitatively determine the cohesive interaction strength present within films composed of each peptide.

6.3 Results

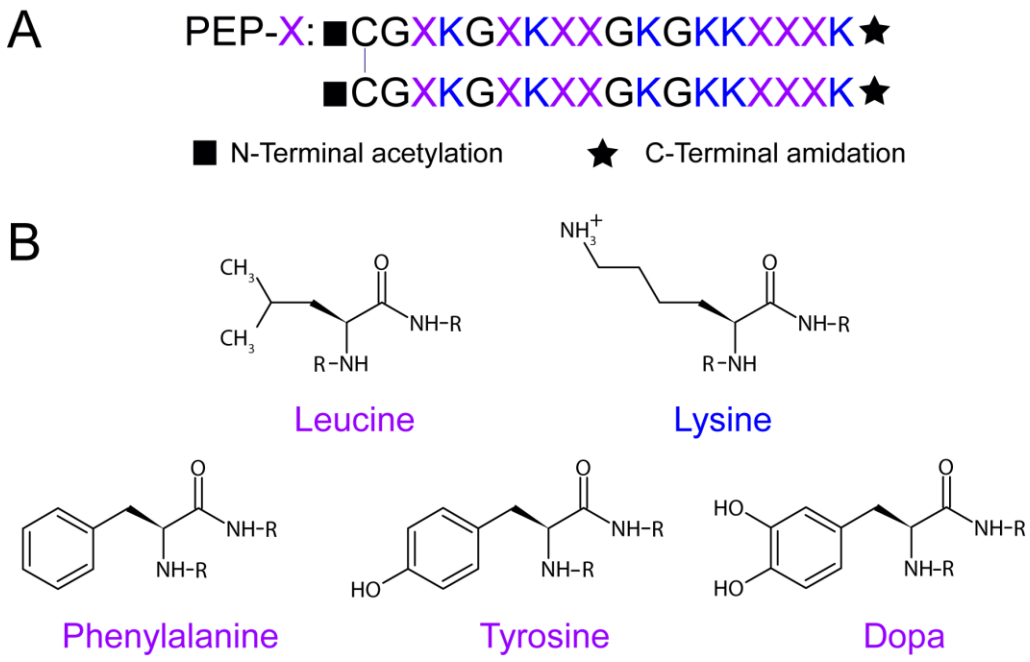

Figure 6.1. Sequences and molecular structures of the peptides studied. Each of the four peptides included one of the amino acids illustrated in panel **(B)** incorporated in the sequence locations marked by a purple "X" in panel **(A)**. The Lys residues are conserved in each peptide sequence and are marked in blue to emphasize the positive charge of Lys at a pH of 2.5.

6.3.1 Peptide design

All four of the peptides are composed of a sequence of 36 amino acids, with the numbers and locations of the glycine (Gly), lysine (Lys), and cysteine (Cys) residues conserved (Fig. 6.1). The locations of the aromatic residues and leucine (Leu) hydrophobic control (X) were also conserved. The four peptides differ only by progressive hydroxylation of the

aromatic residue in three of the peptides: phenylalanine (Phe), tyrosine (Tyr), 3,4-dihydroxyphenylalanine (Dopa). The fourth peptide is a Leu analogue to test whether the strong adhesive forces we measure result from non-specific hydrophobic and/or hydrogen bonding interactions.

The overall sequence is inspired by a Lys- and Dopa-rich sequence of 16 amino acids that is present in the mussel foot protein (mfp), mefp-5, a strongly adhesive mussel foot protein that is prominently featured at the mussel adhesive plaque-solid interface [30, 32]. Dopa is also the dominant aromatic residue in many mussel foot proteins, so we refer to the Dopa peptide as a mussel-mimetic peptide sequence. While some mussel proteins also contain an appreciable Tyr content, Phe is conspicuously deficient in marine mussel adhesive proteins.

Mica was selected as the substrate material since primary amines, like Lys, strongly bind to the surface of mica via ion exchange with the K^+ ions present at the surface of single-crystalline mica [9, 33]. While individual Lys-mica Coulomb bonds are weaker than covalent interactions, the peptides form multiple Lys-mica bonds with an energy of between 3-5 k_BT each. The peptides adsorb irreversibly to mica under the conditions tested, so the adhesive forces across the confined peptide films are proportional to the cohesive interactions between peptide molecules.

6.3.2 Analysis of force-distance profiles

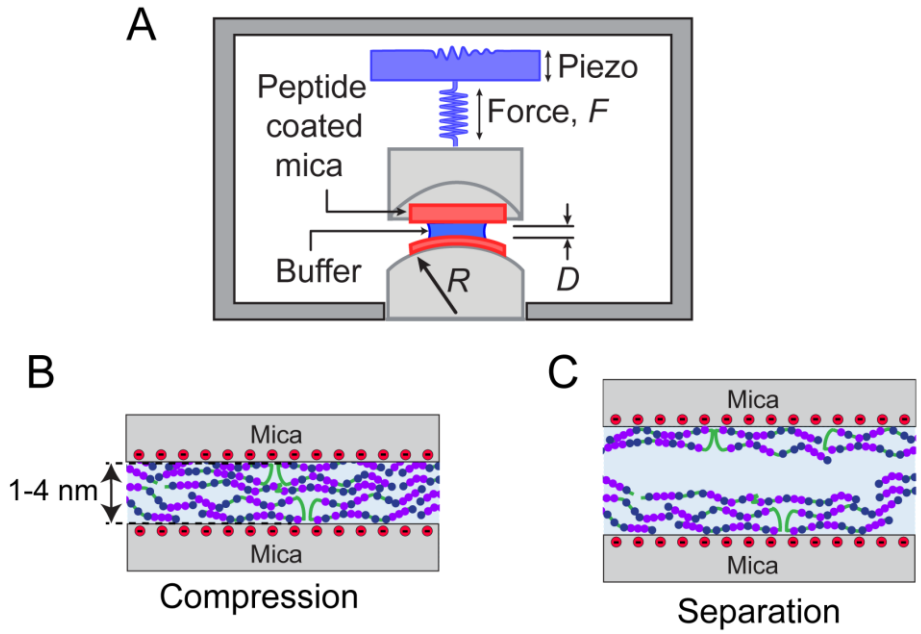

Figure 6.2. (A) Schematic of the SFA experimental setup. Peptide was solution deposited onto mica surfaces before placing into the SFA, and all experiments were performed in a pH 2.5 buffer solution of 100 mM acetic acid and 250 mM KNO_3, without additional dissolved peptide. **(B)** When the two surfaces are compressed into hard contact, a multilayer adhesive peptide film is confined between the two surfaces. **(C)** When the surfaces are separated, the adhesive failure occurs within the peptide film, meaning that the measured work of adhesion is proportional to the cohesive intermolecular interactions between peptide molecules.

When mica surfaces are approached and separated in the background buffer solution (no peptide) using the Surface Forces Apparatus (SFA) [34] (Fig. 6.2), the forces are reversibly repulsive on both approach and separation (Fig. 6.3). For these measurements, the surface separation distance, D, is defined with respect to the hard contact of two mica surfaces in an inert nitrogen atmosphere, where $D = 0$ nm. The non-monotonic features measured for surface separation distances, D, of less than 2 nm are consistent with other measurements across highly concentrated electrolyte solutions and likely result from the complex ordering and/or correlation of ions between the mica surfaces.

All four of the peptides form a diffusive, hydrated surface film that is approximately 3-5 nm thick when solution deposited onto a single mica surface, as confirmed via SFA (Fig. 6.3). The (positive) repulsive forces that are measured when bringing peptide-coated surfaces together originate from the compressing the diffusive films into tightly packed configurations (Fig. 6.2). The ranges of these repulsive forces differs by 1-2 nm among different experiments. As discussed in the Methods section, some of this variability is systematic error introduced during the deposition procedure. Unavoidable changes in the optical path occur when the surfaces are removed from the SFA after collecting distance references to deposit peptides, resulting in up to 2 nm uncertainty in the film thicknesses. Critically, the magnitudes of the repulsive forces and the distances over which one is able to compress the films is characteristic of the peptides molecular structure and is independent of any slight variability in the measured film thickness. In this regime, the slope of the force-distance profiles indicate the compressibility of the peptide films, so we conclude that the peptide films exhibit very similar mechanical properties during compression, with the Leu peptide forming slightly more compact films during deposition than the aromatic peptides.

In contrast, the adhesive forces that are measured when separating the mica surfaces exhibit a significant dependence on the peptide molecular structure (Fig. 6.3). For the Leu peptide (hydrophobic control), the work of adhesion is measured to be 1.3 ± 0.4 mJ/m^2, with the attractive force extending over a distance of 1-2 nm. The range and magnitude of this force is consistent with the pulling apart of weak nonspecific cohesive interactions that likely result primarily from nonspecific hydrophobic interactions, but intermolecular hydrogen bonding along the peptide backbones may also play a role.

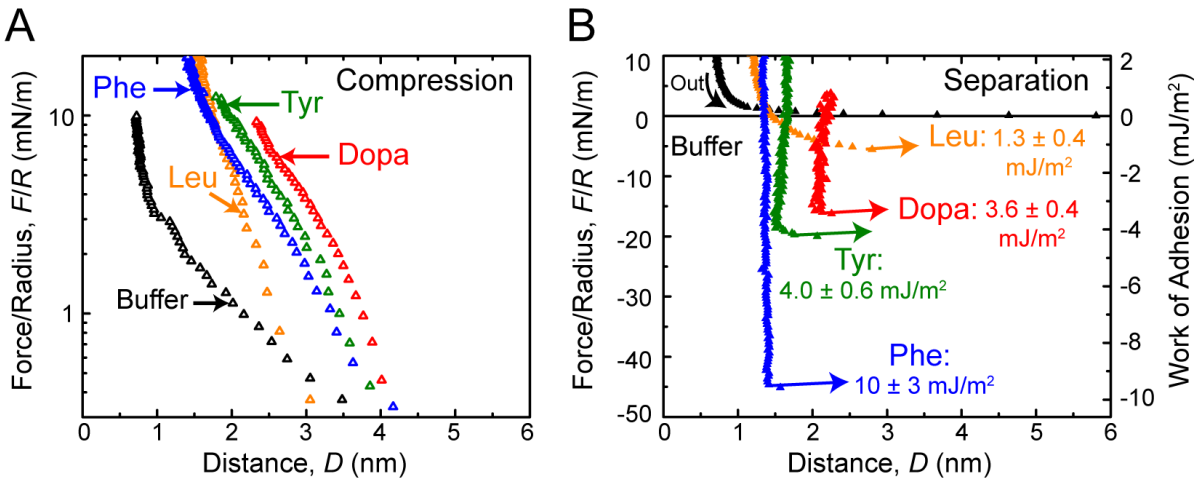

Figure 6.3. (A) Representative force-distance profiles measured when bringing together two mica surfaces. Positive forces are repulsive and negative forces are attractive. The black data was measured in the absence of adsorbed peptide, and each of the colored curves correspond to an experiment where the peptide was adsorbed onto a single mica surface. **(B)** Representative profiles measured when separating mica surfaces. The black force-distance profile measured in the absence of peptide exhibits repulsive behavior, demonstrating that the adhesion measured in the presence of peptide films results from cohesive peptide intermolecular interactions. The average work of adhesion and associated uncertainty quoted on the plot is obtained from at least 10 different force-distance profiles for each peptide. Small variations in peptide film thicknesses were measured between different experiments, and these variations exhibit no dependence on the peptide molecular structure. Importantly, the work of adhesion does not exhibit a systematic dependence on the film thickness, implying that the cohesive interactions are independent of these minor variations.

All three of the aromatic peptides exhibit dramatically increased adhesive forces relative to the Leu control (Fig. 6.3). The work of adhesion measured for the mussel-mimetic Dopa peptide, 3.6 ± 0.4 mJ/m^2, and the Tyr peptide, 4.0 ± 0.6 mJ/m^2, are similar, with the Tyr peptide yielding an average work of adhesion slightly exceeding that of the mussel-mimetic Dopa peptide. The most likely source of this adhesion is cation-π cohesive interactions, so this result shows that the interfacial Lys-Tyr and Lys-Dopa cation-π complexation energies are

similar. This result also implies that cation-π interactions between Dopa and Lys is a dominant mechanism for mediating molecular cohesion in Dopa- and Lys-containing proteins, peptides, and synthetic molecules.

Unexpectedly, the measured the work of adhesion for the Phe peptide is 10 ± 3 mJ/m^2, which is more than double that measured for the Tyr and Dopa peptides. From this result, we conclude that the Phe-Lys cation-π complexation energy is surprisingly strong, compared to the Tyr-Lys and Phe-Lys complexation energies.

6.4 Discussion

The adhesive forces that we measure for all three of aromatic- and Lys-containing peptides are competitive with the work of adhesion measured previously for various Dopa-containing mussel adhesive proteins between mica surfaces, under similar conditions of salinity and pH [17]. Notably, the Phe peptide exhibits adhesive performance between mica surfaces that outcompetes that of the mussel-mimetic Dopa peptide and even rivals that of the most adhesive mussel foot proteins (mfps) tested to date, mefp-5 [32] (after accounting for small differences in salinity and pH).

Dopa is a biologically important functional group that exhibits diverse chemical reactivity [17]. For example, Dopa can chelate multivalent ions [35] and exhibits a propensity to autoxidize and irreversibly crosslink at neutral-to-basic pH conditions [36, 37]. Certainly, this reactivity can be used to advantage, for example, by irreversibly crosslinking, i.e., "curing," molecular films. Unfortunately, the oxidation state of Dopa cannot be easily controlled in many circumstances [36, 38], leaving the adhesive properties of Dopa-containing molecules to be compromised by premature autoxidation. Our results suggest that peptide sequences incorporating Lys and a balance of both Dopa and chemically stable Phe could provide an

attractive alternative for underwater adhesives, hydrogel binding groups, and other applications involving peptide cohesion in harsh oxidizing environments.

Our results also provide additional evidence supporting the importance of cation-π interactions in marine bio-adhesion. Many mussel adhesive proteins are comprised of sequences that are rich in both Lys and Dopa residues [17]. Recently, the adhesion of synthetic bio-mimetic small molecule adhesives to mica surfaces was shown to depend critically on synergy between Dopa and Lys functional groups [31], with these authors concluding that the role of Lys is primarily to eject hydrated ions from mica surfaces, which enables the formation of Dopa-surface bidentate hydrogen bonds.

Practical adhesives are typically composed of larger molecules, such as peptides and proteins, that can assemble to encapsulate particles and/or cover surface heterogeneities [11-13, 39]. For larger molecules that strongly bind to surfaces, the adhesive failure interface is typically shifted away from the surface and into the molecular film [13], so the overall adhesive performance is critically dependent on intermolecular cohesion. Combining this fact with our results, leads us to propose that the adhesive synergy that has been previously observed in Dopa- and Lys-rich mussel foot proteins may primarily be due to cation-π interactions, as opposed to surface hydrogen bonding interactions. Further, our results could provide a molecular basis for understanding how the aromatic- and cation-rich proteins produced by organisms that do not leverage the Dopa functional group, such as barnacles [25], can presumably achieve molecular cohesion rivaling that of Dopa-rich mussel proteins.

More broadly, our work demonstrates that the physical chemistry of cation-π complexation at interfaces substantially differs from the predictions of gas phase calculations. For example, quantum chemical calculations of cation-aromatic binding pairs show that the

interaction energies of K^+-benzene and K^+-phenol interactions agree to within fractions of 1 k_BT [1]. This agreement is due to the counterbalancing sigma electron withdrawing and π electron donating effects exerted by hydroxyl groups on the electron density of aromatic rings. By this reasoning, the subsequent hydroxylation of phenol should minimally impact the energetics cation-π binding energy, and the cation-π binding energies of the Phe, Tyr, and Dopa peptides should be very similar.

Instead, we find that the peptide adhesive strength exhibits a pronounced dependence on the presence of aromatic ring hydroxylation, with the Phe peptide exhibiting intermolecular cohesion that is more than double that of either the Tyr or Dopa peptides. This observation cannot be explained via calculations of binary cation-aromatic binding energies, but is consistent with a previous study of cation-π interactions in self-assembled monolayers [9], where the cation-π interaction energy between poly-L-Lys films and polystyrene films was measured to be twice as strong as that between poly-L-Lys films and poly-L-Tyr films. At the time, this study did not comment on the possible molecular origins of this observation.

To explain both our results and these previous [9] results, we propose that anion complexation with the positively-charged cation-π binding pairs is necessary to form stable cation-π bonds in confined interfaces (Fig. 6.4). In the absence of anion complexation, the cation-aromatic binding pairs within the peptide film will repel one another electrostatically. Hence, the peptide films must contain enough anions to neutralize most of the cation-aromatic binding pairs. Calculations on cation-π-anion complexation [21-23] show that anions interact strongly with the cation as well as the polarized hydrogens in the plane of aromatic rings in cation-π-anion complexes. Thus, we hypothesize that the strong adhesive interactions supported by the Phe peptide result from the highly favorable complexation of anions with

each (positive) cation-π binding pair, relative to a less favorable anion complexation with the mussel-mimetic Dopa peptide and the Tyr peptide.

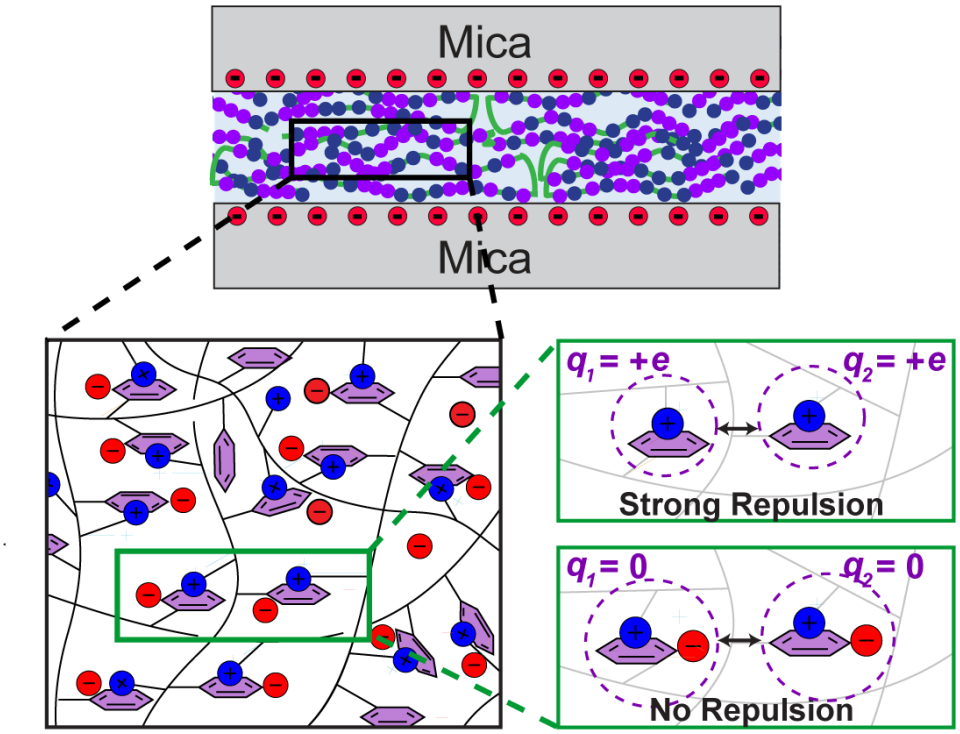

Figure 6.4. Proposed model for the impact of electrostatic correlations on cation-π energetics in aromatic- and Lys-rich peptide films, where many individual cation-aromatic binding pairs form in close proximity. In the absence of anion complexation, each of the cation-π pairs will be positively-charged, leading to strong electrostatic repulsions between closely neighboring binding pairs. Anion complexation neutralizes the positive cation-π binding pairs, eliminating the repulsive electrostatic interaction. Anions sit in the plane of the aromatic ring to interact favorably with both the cation and the aromatic ring quadrupole, and aromatic ring hydroxylation likely disrupts this in-plane anion complexation.

We conclude that replacing even a single aromatic ring hydrogen with a bulky, electronegative hydroxyl group abruptly decreases the strength of cation-π mediated cohesion within the peptide films, while the addition of a second hydroxyl group leads to only a marginal additional decrease in cohesion. Thus, we demonstrate that the rational inclusion or

exclusion of aromatic ring hydroxyl groups in peptide binding domains provides a facile molecular strategy for tuning the cohesive binding strength of cation-π interactions.

6.5 Summary and outlook

We establish that that the cohesive properties of short aromatic- and Lys-rich peptides rival that of the strong, reversible intermolecular cohesion exhibited by full mussel adhesive proteins. Thus, these engineered short peptides self-assemble to form nanoscale films that mediate reversible underwater adhesion between solid surfaces rivaling that of native mussel proteins, a task that has remained a substantial engineering challenge.

We also find that peptides incorporating the chemically stable amino acid Phe, a functional group that is conspicuously deficient in the sequences of mussel proteins, exhibit reversible adhesive interactions significantly exceeding that of an analogous mussel-mimetic Dopa-containing peptide. The strong reversible cohesion exhibited by the Phe peptide suggests that peptide sequences incorporating Lys and a balance of both Dopa and Phe could provide an attractive approach for developing underwater adhesives, hydrogel binding groups, and other applications involving peptide cohesion in harsh oxidizing environments

We ultimately conclude that cation-π interactions provide a compelling molecular motif that plays a key role in enabling the robust underwater adhesion exhibited by numerous marine organisms. This picture may provide a molecular basis for the impressive adhesive performance of marine organisms, like barnacles [25], that synthesize adhesive proteins lacking the Dopa functional group. More broadly, we demonstrate that interfacial confinement fundamentally alters the energetics of cation-π mediated assembly, an insight that should prove relevant for diverse areas, ranging from rationalizing biological assembly to engineering peptide-based biomaterials.

6.6 Materials and methods

6.6.1 Peptide synthesis and modification

The peptides CGYKGKYYGKGKKYYYK, CGFKGKFFGKGKKFFFK and CGLKGKLLGKGKKLLLK were synthesized by GenScript (NJ, USA) using routine solid-phase synthesis that included N-terminal acetylation and C-terminal amidation and were provided as a desalted solid. Mushroom tyrosinase (3000 U/mg) was from Aldrich-Sigma and all other reagents were of analytical grade.

All three peptide monomers were cross-linked to form dimers. 1 mg of peptide monomer was dissolved in 1 ml pH 7.0, 0.1 M phosphate buffer, and mixed with 10 µl of 5 mg/ml $NaIO_4$. After shaking for 10 min, the solution was injected to reverse phase HPLC using a 260 × 7-mm RP-300 Aquapore (Applied Biosciences Inc., Foster City, CA) column, eluted with a linear gradient of aqueous acetonitrile. Eluent was monitored continuously at 230 and 280 nm, and 0.33 ml fractions containing peptides were pooled. Mass spectra of those fractions were obtained on a Micromass QTOF2 tandem mass spectrometer (Waters Corp.) with an electrospray ionization source. The fractions containing pure peptide dimer, which were named PEP-Leu, PEP-Tyr, PEP-Phe, were collected and freeze dried for future use.

Enzymatic modification to obtain PEP-Dopa: 1 mg of PEP-Tyr were dissolved in 1 ml pH 7.0, 50 mM borate, 0.1 M phosphate-ascorbate buffer, in an Eppendorf microfuge tube. After adding mushroom tyrosinase (0.3 mg), the tube was shaken for 4 hrs at ambient room temperature and pressure. Each reaction was stopped by adding 40 µl glacial acetic acid, and the resulting product was purified with reverse phase HPLC column. After being analyzed by mass spectrometer, fractions containing 5 or 6 Dopa residues were collected and freeze dried. PEP-Tyr, Dopa, Phe, Leu were dissolved respectively in 100 mM acetic acid (Sigma Aldrich)

and 250 mM potassium nitrate (Sigma Aldrich) buffer (pH 2.5) with a peptide concentration of 100 μg/mL and kept in -80 °C freezer.

6.6.2 Peptide deposition

Nanoscale films of each peptide were deposited onto freshly-cleaved mica surfaces by immersing the mica surfaces for 20 min in 3 mL of 100 mM acetic acid, 250 mM KNO_3 solution (pH 2.5) containing 15 μL of a solution of 1 mg/mL peptide in 100 mM acetic acid. This protocol enabled reproducible assembly of films of comparable molecular density and thicknesses for each peptide. The thicknesses of the diffusive (~3-5 nm) and compressed (~1-3 nm) peptide films indicates the deposition of multi-layer peptide films onto the mica surfaces (Fig. 6.2).

The deposition protocol requires removing the surfaces from the SFA after measuring the distance reference, introducing an uncertainty of up to 2 nm for the thickness of the peptide films. Despite this small systematic error, the film thicknesses do trend with the peptide molecular structure as: Leu ~ Phe < Tyr < Dopa (Fig. 6.3 and Table 6.1). For each approach and separation measurement, the relative uncertainty between the points in the force-distance profile is below 3 Å, meaning that slope of the compression and the magnitude of the work of adhesion are accurate to Å distance and nN force resolutions.

Table 6.1. Thickness of peptide films under differing deposition conditions.

Peptide	Asymmetric thickness	Symmetric thickness
Leu	1.6 ± 0.4 nm	2.0 ± 0.4 nm
Phe	1.4 ± 0.6 nm	2.2 ± 0.4 nm
Tyr	2.3 ± 0.6 nm	2 ± 2 nm
Dopa	2.6 ± 0.8 nm	

6.6.3 Intermolecular force-distance measurements

Force-distance, $F(D)$, measurements were performed using a standard SFA 2000 [34], using the detailed protocol discussed in Ref. 34. Briefly, peptide-coated mica surfaces were brought into molecular contact in a background electrolyte solution of 250 mM KNO_3, 100 mM acetic acid (pH 2.5) by using a piezoelectric crystal to actuate the top surface at ångstroms-per-second rates (Figs. 6.2 and 6.3). After compression, the two surfaces were left to equilibrate for at least 5 minutes. The surfaces were then separated at nanometer-per-second rates using a motor, which progressively loads the SFA spring, until the surfaces abruptly "jump" apart to large separations. This instability "jump" distance is used to determine the load on the spring prior to the separation of the two surfaces. This adhesive force is then converted into the reported work of adhesion, E_{ad}, by using the JKR theory of adhesion [40].

6.6.4 Establishing cohesive failure

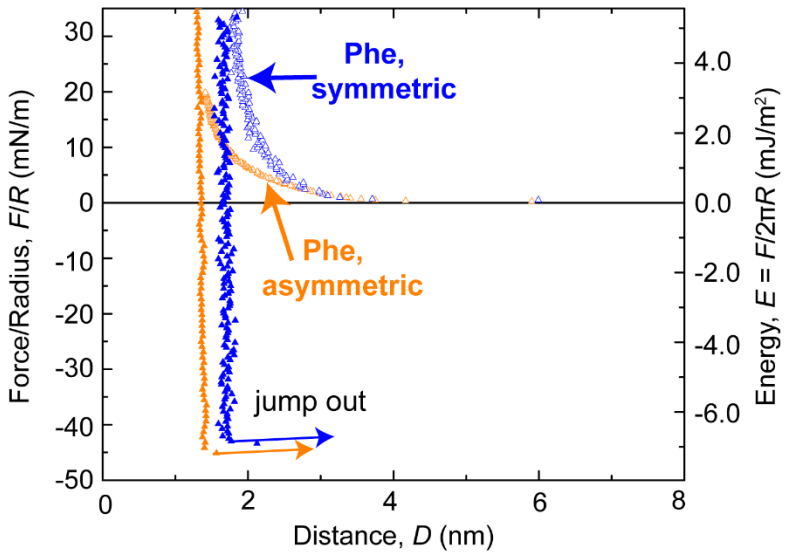

Figure 6.5. Representative force-distance profiles measured across the Phe peptide, comparing the adhesive properties of peptide films that were deposited onto only one of two mica surfaces (asymmetric, orange) to the adhesive properties of peptide films that were deposited onto both mica surfaces (symmetric, blue).

A key test of the film failure mechanism is to compare the adhesive performance of molecular films that are deposited onto only one of the two surfaces to the adhesive performance of molecular films that are deposited onto both surfaces. For the first set of experiments, peptides were deposited onto a single mica surface and a bare mica surface as the second surface for SFA measurements. A second set of experiments was then performed where peptides were deposited onto each of the two mica surfaces, creating a symmetric SFA setup. Previously, these two experimental protocols have resulted in qualitatively and quantitatively differing force-distance profiles when the adhesive failure occurs at the protein-surface or peptide-surface interface [17, 32]. On the other hand, force-distance experiments that implicated cohesive failure exhibit close agreement for the works of adhesion measured

via the two approaches [10, 17]. In this work, the measured adhesive forces are in quantitative agreement when the peptides are deposited using both methods (Fig. 5). The primary difference between the two experimental protocols is that the compressed peptide films are systematically thicker when peptide is deposited onto both surfaces, as compared to single surface deposition.

Ultimately, the primary mechanism of mica-peptide surface bonding is through the formation of Lys-mica Coulomb bonds, an interaction that should be independent of the molecular structures of the aromatic amino acids studied. As a result, the fact that alterations to the structure of the aromatic residues result in systematic changes to the measured E_{ad} is inherently indicative of cohesive failure.

6.7 References

1. Ma, J. C. & Dougherty, D. A. The Cation-π interaction. *Chem. Rev.* **97,** 1303–1324 (1997).
2. Gallivan, J. P. & Dougherty, D. A. Cation-π interactions in structural biology. *Proc. Natl Acad. Sci. U. S. A.* **96,** 9459–9464 (1999).
3. Crowley, P. B. & Golovin, A. Cation-π interactions in protein-protein interfaces. *Proteins* **59,** 231–239 (2005).
4. Madahevi, A. S. & Sastry G. N. Cation-π interaction: its role and relevance in chemistry, biology, and material science. *Chem. Rev.* **113,** 2100–2138 (2013).
5. Zhong, W. *et al.* From *ab initio* quantum mechanics to molecular neurobiology: a cation-π binding site in the nicotinic receptor. *Proc. Natl Acad. Sci. U. S. A.* **95,** 12088–12093 (1998).

6. Khademi, S. *et al.* Mechanism of ammonia transport by Amt/MEP/Rh: structure of AmtB at 1.35 Å. *Science* **305,** 1587–1594 (2004).
7. Meyer, E. A., Castellano R. K. & Diederich, F. Interactions with aromatic rings in chemical and biological recognition. *Angew. Chem. Int. Ed.* **42,** 1211–1250 (2003).
8. Hwang, D. S., Zeng, H., Lu, Q., Israelachvili J. N. & Waite, J. H. Adhesion mechanism in a DOPA-deficient foot protein from green mussels. *Soft Matter* **8,** 5640–5648 (2012).
9. Lu, Q. *et al.* Nanomechanics of cation-π interactions in aqueous solutions. *Angew. Chem.* **125,** 4036–4040 (2013).
10. Kim, S. *et al.* Cation-π interaction in DOPA-deficient mussel adhesive protein mfp-1. *J. Mater. Chem. B* **3,** 738–743 (2015).
11. Isrealachvili, J. N. *Intermolecular and Surface Forces: Revised Third Edition.* Academic Press (2011).
12. de Gennes, P. G. Soft adhesives. *Langmuir* **12,** 4497–4500 (1996).
13. Rose, S. *et al.* Nanoparticle solutions as adhesives for gels and biological tissues. *Nature* **505,** 382–385 (2014).
14. Sunner, J., Nishizawa, K. & Kebarle, P. Ion-solvent molecule interactions in the gas phase. The potassium ion and benzene. *J. Phys. Chem.* **85,** 1814–1820 (1981).
15. Burley, S. K. & Petsko, G. A. Amino-aromatic interactions in proteins. *Fed. Euro. Biochem. Soc.* **203,** 139–143 (1986).
16. Deakyne, C. A. & Meot-Ner, M. Unconventional hydrogen bonds. 2. NH^+-π complexes of onium ions with olefins and benzene derivatives. *J. Am. Chem. Soc.* **107,** 474–479 (1985).

17. Lee, B. P., Messersmith, P. B., Isreaelachvili, J. N. & Waite, J. H. Mussel-inspired adhesives and coatings. *Annu. Rev. Mater. Res.* **41,** 99–132 (2011).
18. Wong Po Foo, C. T. S., Lee, J. S., Mulyasasmita, W., Parisi-Amon, A. & Heilshorn S. C. Two-component protein-engineered physical hydrogels for cell encapsulation. *Proc. Natl Acad. Sci. U. S. A.* **106,** 22067–22072 (2009).
19. Norrby, P. & Liljefors, T. Strong decrease of the benzene-ammonium ion interaction upon complexation with a carboxylate anion. *J. A. Chem. Soc.* **121,** 2303–2306 (1999).
20. Bartoli, S. & Roelens, S. Binding of acetylcholine and tetramethylammonium to a cyclophane receptor: anion's contribution to the cation-π interaction. *J. Am. Chem. Soc.* **124,** 8307–8315 (2002).
21. Hunter, C. A., Low, C. M. R., Rotger, C., Vinter, J. G. & Cristiano, Z. The role of the counterion in the cation-π interaction. *Chem. Commun.* 834–835 (2003).
22. Carrazana-García, J. A., Rodríguez-Otero, J. & Cabaleiro-Lago, E. M. A computational study of anion-modulated cation-π interactions. *J. Phys. Chem. B* **116,** 5860 (2012).
23. Carrazana-García, J. A., Cabaleiro-Lago, E. M., Campo-Caharrón, A. & Rodríguez-Otero, J. A theoretical study of ternary indole-cation-anion complexes. *Org. Biomol. Chem.* **12,** 9145–9156 (2014).
24. Shao H. & Stewart, R. J. Biomimetic underwater adhesives with environmentally triggered setting mechanisms. *Adv. Mater.* **22,** 729–733 (2010).
25. Kamino, K., Nakano, M. & Kanai, S. Significance of the conformation of building blocks in curing of barnacle underwater adhesive. *FEBS J.* **279,** 1750–1760 (2012).
26. Yamamoto, H. Synthesis and adhesive studies of marine polypeptides. *J. Chem. Soc. Perkin Trans. 1* 613–618 (1987).

27. Yu, M. & Deming, T. J. Synthetic polypeptide mimics of marine adhesives. *Macromolecules* **31,** 4739–4745 (1998).

28. Mattson, K. M. et al. A facile synthesis of catechol-functionalized poly(ethylene oxide) block and random copolymers. *J. Polymer Sci. Part A* (2015).

29. Lee, H., Dellatore, S. M., Miller, W. M. & Messersmith, P. B. Mussel-inspired surface chemistry for multifunctional coatings. *Science* **318,** 426–430 (2007).

30. Wei Wei, *et al.* Bridging adhesion of mussel-inspired peptides: role of charge, chain length, and surface type. *Langmuir* **31,** 1105–1112 (2015).

31. Maier, G. P., Rapp, M. V., Waite, J. H., Israelachvili, J. N. & Butler, A. Adaptive synergy between catechol and lysine promotes wet adhesion by surface salt displacement. *Science* **349,** 628–632 (2015).

32. Danner, E. W., Kan, Y., Hammer, M. U., Israelachvili, J. N. & Waite, J. H. Adhesion of mussel foot protein mefp-5 to mica: an underwater superglue. *Biochemistry* **51,** 6511–6518 (2012).

33. Luckham, P. F. & Klein, J. Forces between mica surfaces bearing adsorbed polyelectrolyte, poly-L-lysine, in aqueous media. *J. Chem. Soc. Faraday Trans. 1* **80,** 865–878 (1984).

34. Israelachvili, J. N. *et al.* Recent advances in the surface forces apparatus (SFA) technique. *Rep. Prog. Phys.* **73,** 036601 (16 pp) (2010).

35. Sever, M. J., Weisser, J. T., Monahan, J., Srinivasan, S. & Wilker, J. J. Metal-mediated cross-linking in the generation of a marine mussel adhesive. *Angew. Chem. Int. Ed.* **43,** 448n450 (2004).

36. Yu, M., Hwang, J. & Deming, T. J. Role of L-3-4-dihydroxyphenylalanine in mussel adhesive proteins. *J. Am. Chem. Soc.* **121,** 5825–5826 (1999).

37. Lee, H., Scherer, N. F. & Messersmith, P. B. Single-molecule mechanics of mussel adhesion. *Proc. Natl Acad. Sci. U. S. A.* **103,** 12999–13003 (2006).

38. Martinez Rodriguez, N. R., Das, S., Kaufman, Y., Israelachvili, J. N. & Waite, J. H. Interfacial pH during mussel adhesive plaque formation. *Biofouling* **31,** 221–227 (2015).

39. Liaqat, F. *et al.* High-performance TiO_2 nanopartice/DOPA polymer composites. *Macromol. Rapid Commun.* **36,** 1129–1137 (2015).

40. Johnson, K. L, Kendall, K. & Roberts, A. D. Surface energy and the contact of elastic solids. *Proc. R. Soc. Lond. A* **324,** 301–313 (1971).